Quantum Control in Atoms and Molecules using Two-Color High Harmonic Generation

A thesis submitted in partial fulfilment of

the requirements for the degree of

Doctor of Philosophy

by

Pranav Bhardwaj

(Roll No. 18330018)

Under the supervision of

Dr. Rajesh Kumar Kushawaha

Associate Professor

Atomic, Molecular and Optical Physics Division

Physical Research Laboratory, Ahmedabad, India

DISCIPLINE OF PHYSICS

INDIAN INSTITUTE OF TECHNOLOGY GANDHINAGAR

2024

Declaration

I declare that this written submission represents my ideas in my own words, and where others' ideas or comments have been included, I have adequately cited and referenced the sources. I also declare that I have adhered to all academic honesty and integrity principles and have not misrepresented, fabricated, or falsified any idea/data/-fact/source in my submission. I understand that any violation of the above will cause disciplinary action by the Institute and can also evoke penal action from the sources which have thus not been appropriately cited or from whom proper permission has not been taken when needed.

Name: Pranav Bhardwaj

(Roll No: 18330018)

Date: 06-06-2025

CERTIFICATE

It is certified that the work contained in the thesis titled **"Quantum Control in Atoms and Molecules using Two-Color High Harmonic Generation"** by Mr. Pranav Bhardwaj (Roll No. 18330018), has been carried out under my supervision and that this work has not been submitted elsewhere for a degree.

10-06-2025

Dr. Rajesh Kumar Kushawaha
Associate Professor
Atomic, Molecular and Optical Physics Division,
Physical Research Laboratory,
Ahmedabad, India.

(Thesis Supervisor)

Date:

To

my Sahabji

Acknowledgments

It's funny how, despite having written this entire thesis, this is the only section that truly feels like it's mine. So I'll take this opportunity to thank everyone who has led me here.

This journey has taken longer than I expected, but it has been a real one. Now that I'm finally at the end of it, I can perhaps — somewhat sheepishly — take pride that I did it, and that I've (almost) enjoyed every bit of it. Things often look better in retrospect, but some people and moments have genuinely shaped my academic journey. This thesis exists because of them, and to them, I owe my deepest thanks.

First and foremost, I would like to thank my supervisor, Dr. Rajesh Kumar Kushawaha, for his constant support and guidance. I've lost count of the number of times I walked into his office thinking I'd hit a dead end, only for him to calmly listen and help me find a way forward. He has instilled confidence in me and trust in my work when I had none. His patience, his faith in me, and his ability to persevere are qualities I hope to carry forward when it's my turn to guide someone.

This Ph.D. is a significant part of the dream I had of becoming a scientist ever since my second-grade teacher praised me for asking a good question! My best guess is that it was a question about dinosaurs (yep, I was crazy about dinosaurs!) or perhaps plants. I don't know! I don't remember really. All I remember is how happy I was to hear the words "good question" echo in that small and colorful classroom. They made my teeny little chest fill up with confidence and pride! I've never stopped asking good questions since! So there it is — for those of you who feel I ask way too many questions, now you know who to blame. :P

At every stage of my life, I've been blessed with teachers who chose to encourage my curiosity and motivated me to ask deep and meaningful questions. Their attitude and encouragement — especially at moments when they didn't have all the answers — fueled my fascination for science. This journey began in school with Manoj Sir and Manish Sir. In my bachelor's, I owe it to Vimal Sir, for he is the one who fixed my physics. He taught me everything that I know. He made me better. He made me good enough to chase the dream of becoming a physicist. During my Master's, I discovered there's something even more fulfilling than asking good questions: answering them. I was captivated by the depth and clarity of Prof. Seshadri and Prof. Patrik in their lectures — I remember smiling ear to ear during their classes. They always believed in me, especially when I didn't. To all these teachers, thank you.

My Master's at D.U. was one of the hardest things I've done. I got through it only because of friends like Vishal, Vicky, and Nikita (and perhaps also because I kept a healthy distance from our beloved topper, Anshika — more on her soon). Our routine visits to the departmental canteen and collective despair over "certain" tutorials are cherished memories. Let me take this opportunity to explicitly state that the only reason I managed to get my Master's degree is due to Nikita. Her constant support, remarkable determination, and laughter in moments of deep despair have gotten me here. We've discussed my Ph.D. troubles on many occasions and she has always been among the most uplifting forces in my life — all the while acting as if she did nothing. Thank you for being my best friend.

D.U. also introduced me to Tanya, my bestest friend and entangled particle. We often joke that our lives are quantumly correlated. I thank my stars that I found her and that she has since, decided to dedicate her whole life copying what I do! I picked A.N.T., she picked A.N.T.; I came to PRL, she came to PRL; I wanted to do Quantum

Optics, she DID Quantum optics; I came to Europe for my Post.Doc and guess who's coming to Europe for hers? Jokes aside, I have been very fortunate to live 5 years of my life in close proximity of my best friend! I wonder how many people can say that. We have studied together, laughed together (a lot! until our stomachs hurt! Seriously! At really REALLY inappropriate times), had 1 A.M conversations over tea at our beloved Tea-Post, and perhaps most importantly been silent together. May our paths remain entangled for decades to come :)

PRL gave me memories I didn't expect. The hostel life was incredible — thanks to the best batch ever. I remember how quickly we all bonded, how many GPLs we were a part of, and how no matter whose birthday it was, EVERYBODY got kicked! We've shared our celebrations, our troubles, our festivals, our birthdays (special thanks to Soni), our home-brought sweets (which were often snatched — courtesy of the hunter gang), and everything in between. We were a family. Thank you, Daya, Anju, Soni, Naval, Binal, Meghna, Akanksha, Yash, Namita (my didi :)), Nabo, Monica, Yogesh, Deepak and Deepak, Anupam, Sandeep, Sanjit, and Siddharth — you all made it unforgettable. I'll always remember how we used to all come out to our hostel balconies and shout at each other. We had a blast! I've had many beautiful conversations with you all — at Tea Post, in PDF quarters (with Meghna madam as the host), at Anju's room (our adda), in our TV room, under the thinking tree, near Sarabhai. Thank you for all those times.

I was especially lucky to have my M.Sc. batchmate Anshika as my senior at PRL. Our ritualistic visits to her room after dinner made me miss my home a little less. Thank you for being such a wonderful host and making sure our Vitamin D levels stayed high (credit, Amul).

I was lucky to have Daya in my life to share the curiosity and excitement I've had

for physics. I thank him for the countless nights we have spent discussing physics (credit to Anju for providing tea during a few of these times), philosophy, spirituality, why one should get married, why marrying after completing a postdoc is a terrible idea, and the list goes on. Thank you for challenging me. Thank you for making me better.

I consider myself extremely lucky to have done my Ph.D. in Femtolab with my colleagues Madhu and Vinitha around me. Madhu taught me most of what I know. I am immensely thankful to him for all the times I woke him up at 2:00 p.m. to close my HHG chamber. There have been many plans which relied solely on the assumption: "Madhu sambhal lega." Cheers to you, my friend and my brother. Vinitha, thank you for supporting me the way you did — late at night, on Sundays even! Half of my experiments and the data I took wouldn't have existed if it weren't for you. I will cherish all the meals we had in our lab, the videos we watched when times were still good, and of course our temporal overlap celebrations at restaurants. The three of us have had so many conversations together that the memories just fill up my heart.

I thank Ritu for the fun conversations we've had and for her feedback on multiple occasions during my presentations. I thank Pooja Chandravanshi for automating my HHG setup with her LabView programs. I also want to thank Indrajit for supporting me through my final year. I wish all the best to him and Vinitha on their Ph.D. work. Watch out for their theses, people — they are going to rock you with their XUV-IR setups. I am also thankful to my lab colleagues Swetapuspa, Sowmyashree, Dr. Prashant Kumar, and Dr. Muhammed Shameem for helping me toward my research objectives.

I would also like to thank my family, who have been my foundation through it all. To my parents — for their unconditional love, quiet strength, and unwavering belief in me even when they didn't fully understand what I was doing. I think the one thing

we could all relate to was: "laser nahi chal rahi." Thank you both for making this happen — for giving me the best education you possibly could and for buying cable that had Discovery Channel access :P. I would also like to thank my sweet little sister (laal chooha) Heenu, for always having my back (..you and I have always been like!). I'm glad I have her. We share this weird conversational language that's completely ours, and it has helped me through many frustrating moments often turning them into laughter. Buy me PS6 (pretty pleaaase)! It's been a crazy six years, and I'm truly grateful I had you all and our lovely home to come back to. This achievement is as much yours as it is mine.

I am also thankful to someone who has both been a witness and an important part of this journey throughout. Someone who has literally seen me grow and study, and supported me with whatever she had — my best friend of 14 years! Sadly, she decided to give up this title for what she claims is a better one — that of my wife. I can only wish you good luck for the ambitious role you've taken, Tulika. Thank you for always being by my side: for taking care of me and my family; for turning my apartment into a home; for offering me tea, even now (it's 3:00 a.m.) as I'm writing this; for badly wanting me to succeed; for making me a better person; and for loving me.

I'd also like to thank the PRL workshop team — Vaghela Sir, Pramod Sir, Kaila Sir, Vipul bhai, Rohit, and others — for their constant support during the development of our lab, often stepping in on very short notice. My thanks also go to the academic committee, CMG, canteen staff, housekeeping, and administrative departments — with special mention to Mrs. Richa and Mr. Pradeep Chauhan.

I'm grateful to my DSC members — Prof. Goutam Samanta, Prof. Ketan Patel, and Dr. Naveen Chauhan — for their understanding and support, especially during my extension period. I also thank Prof. R.P. Singh for his guidance on multiple occasions,

both academic and personal. I also owe a great debt of gratitude to Dr. Thierry Ruchon, who guided me at a crucial juncture in my Ph.D. when I was struggling to obtain any signal from the HHG setup. His experience proved invaluable and helped steer me in the right direction.

I'd like to thank someone at the risk of sounding self-indulgent — me. This Ph.D. marks a significant milestone in becoming a scientist — a dream I've had since I was a little kid. And while I consider this thesis to be perfectly average (honestly!), I can really smile and say: "I gave it my best (well, almost)." Six years of work, setbacks, breakthroughs, and relentless tinkering — and I still wish I had more time. If I could do it again, I would. But only with the same incredible people around me. I wish I had more (data-taking) time with the setup I built (I really, really love HHG), but I'm happy that my setup will be in the capable hands of my junior Sonali, who will take things forward. I wish her the best.

To the future reader — perhaps a young researcher — I'll leave you with two small pieces of advice. First, I once told my supervisor that building an HHG setup would take me three months max. It took me five years. That's research. Be patient. Second, there may come a (terribly frustrating) time when everything falls apart and no one can help you — not friends, not mentors, not literature, not even your supervisor. When that happens, wait. Let time pass and do its thing. Most importantly, in such times, hold onto your friends. In the times you feel alone, you shouldn't be lonely.

And finally, to someone who has always been my rock in times of uncertainty — someone who once told me I'd do a good Ph.D., and to whom I replied with full-blown skepticism: "How?" To the greatest teacher I've ever had — I bow down with gratitude. Thank you, sir.

Abstract

Keywords: High Harmonic Generation, Attosecond Physics, Two-color fields

Light-matter interactions form some of he most fundamental processes available to us that unravel the secrets of the quantum realm. At an atomic level, the interaction of light with atoms and molecules holds the key to unraveling the intricacies of quantum mechanics and understanding the fundamental building blocks of matter and energy. This thesis explores a remarkable process called Higher Harmonic Generation (HHG) as a powerful tool for generating ultrashort Extreme Ultraviolet (EUV/XUV) pulses. These pulses hold immense potential for investigating and manipulating the ultrafast dynamics in atoms and molecules, a realm where processes occur on timescales of the order of attoseconds, or billionths of a billionth of a second, enabling us to unravel the intricacies of electronic motion and molecular dynamics with unprecedented precision.

The thesis begins by establishing the context of attosecond physics and the fundamental principles behind HHG. It emphasizes the crucial role of HHG in high harmonic spectroscopy (HHS) – a technique capable of capturing sub-femtosecond nuclear and electronic motions within a molecule.

Following this foundation, a significant effort was devoted to the in-house development of the HHG setup, detailing the key experimental methodologies employed. This includes a comprehensive description of the laser system, the setup design, and optimization schemes employed to achieve optimal HHG performance.

A significant portion of the research focuses on extending the capabilities of traditional single-color HHG setups by utilizing Two-Color laser fields. The thesis explores the theoretical framework and the necessary experimental adjustments required

for implementing this advanced HHG scheme. Experimental results from Argon (Ar) and Carbon Dioxide (CO_2) highlight the complexities encountered, particularly in capturing the behavior of molecules like CO_2 within the two-color regime.

Further chapters explore HHG from various atoms (Ar, Kr, Xe) and molecules (N_2, CH_3Cl) using two-color laser fields. The research investigates different experimental schemes to control the behavior of tunnel electrons and achieve desired HHG outcomes. The findings highlight the influence of key parameters like two-color intensity, polarization, and relative phase in the attosecond domain (10^{-18}s) on the overall HHG yield. Notably, the observed dependence on relative phase suggests that it modulates the trajectories of tunnel electrons, thereby affecting the HHG yield. These experimental observations are further supported by theoretical simulations, providing a deeper understanding of the underlying HHG process.

The thesis concludes by summarizing the key findings and establishing quantum control in both atoms and molecules and outlining exciting directions for future research.

Abbreviations

MPI	Multiphoton Ionization
TI	Tunnel ionization
HHG	High Harmonic Generation
QWP	Quarter Wave Plate
OTC	Orthogonal polarized Two-Color laser field
PTC	Parallel polarized Two-Color laser field

Contents

List of Figures

Chapter 1

Introduction

The study of light-matter interactions is at the forefront of unlocking the mysteries of the atomic world [3, 4]. Within the realm of ultrafast laser science, the primary objective is to observe, understand, and manipulate the nuclear and electron dynamics in atoms and molecules on their intrinsic time scales. While significant effort has been made in this pursuit, investigating the dynamics of inner valance and core electrons necessitates the use of tunable ultrashort Extreme Ultraviolet (XUV) pulses. The interaction of intense femtosecond light pulses with atoms yields XUV/Soft X-Rays through a highly nonlinear process called High Harmonic Generation (HHG), marking the advent of Attosecond science [5–10].

This year's Nobel Prize in physics was awarded to Pierre Agostini, Ferenc Krausz and Anne L'Huillier "for experimental methods that generate attosecond pulses of light for the study of electron dynamics in the matter." HHG is the first step in the grand scheme of Attosecond science [11–15].

HHG arises when an atom is exposed to an intense ($> 10^{13} W/cm^2$) ultrashort

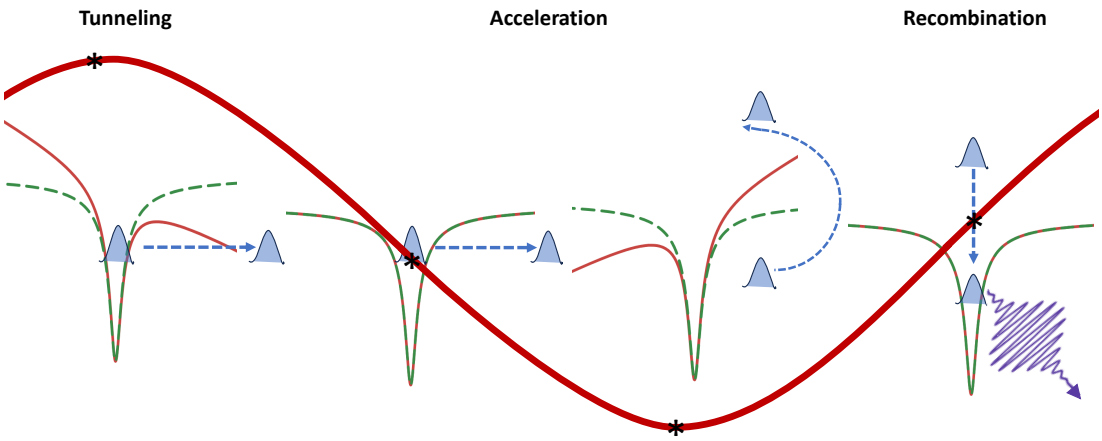

Figure 1.1: Corkum's three step model [1] showing Tunneling, Acceleration, and recombination of the electron with the parent ion. The red sinusoidal curve denotes the field. The green curve shows the coulomb potential, red curve shows the total potential denoting the sum of the atomic potential and the static electric field potential at the temporal position of the laser field. The blue cloud shows the evolution of the electronic cloud as the field progresses. The generated XUV pulse is denoted in violet.

pulse, resulting in the emission of XUV/Soft X-rays. Unlike other nonlinear phenomena, HHG is non-perturbative in nature, as shown by Paul Corkum's renowned three-step semi-classical model [1], often referred to as the "simple man's model." This model successfully predicts crucial aspects of the process, including the energy of the outgoing photons, the cutoff energy for a given medium, and the absence of even harmonics in the HHG spectrum.

1.1 The Three Step Model

Paul Corkum's seminal three-step model [1] provides a simplified yet powerful explanation for high harmonic generation. The entire process can be broken down into 3 steps as shown in Fig.1.1, namely,

1. **Tunneling Ionization**:

   The intense electric field of the laser pulse interacts with the atomic potential, creating a combined effective potential. If the field is strong enough, this combined potential can be lower than the ionization energy of the system at specific locations and times. This allows the electron a finite probability of ”tunneling” through this classically forbidden region and escaping the atomic potential.

2. **Acceleration in the field**:

   Once freed from the atom, the electron experiences only the influence of the laser field. This strong electric field accelerates the electron away from the parent ion. The energy gained by the electron in this process can be classically estimated using Newton's equation of motion.

3. **Recollision and XUV Emission**:

   As the laser field oscillates, its direction reverses, and the electron can be driven back toward the parent ion. This recollision with the parent ion may lead to recombination. If this recombination occurs, the electron releases its excess energy in the form of a coherent XUV photon.

The XUV photon energy is equal to the difference between the initial energy at the time of recombination and the final bound state energy. This explains how an initial infrared laser pulse (800 nm) can lead to the generation of high-frequency XUV radiation (˜10 nm). It's important to note that this model is considered semi-classical because of the initial and final steps, both of which are governed by quantum mechanics. Only the acceleration of the free electron in the laser field is approximated using classical mechanics. Fully quantum mechanical descriptions for the process are also present [16]. However, the present model explains all qualitative characteristics of the

process, such as the cut-off energy, wavelength scaling, and the absence of even-order harmonics.

A representation of the typical high harmonic spectrum is shown in Figure 1.1.

As discussed previously, we can use Newton's equation of motion to understand the propagation of the tunneled electron, i.e.,

$$m_e \frac{d^2y}{dt^2} = -eE_0 \cos \omega_0 t \tag{1.1}$$

Note that more complex fields representative of a femtosecond pulse have been used when we perform full classical simulations for estimating the return kinetic energy and yield of the return electron trajectories in Chapter 4. The initial conditions for the process are taken such that both the position and velocity of the free electron at the time of birth are zero, i.e., $\frac{dy}{dt}(T)$=0 and y(T)=0. By imposing these initial conditions, we obtain the full solution of the eq.1.3 given by,

$$v(t) = \frac{dy}{dt} = -\frac{eE_0}{m_e}(\sin \omega_0 t - \sin \omega_0 T) \tag{1.2}$$

and,

$$y(t) = \frac{eE_0}{m_e \omega_0^2}(\cos \omega_0 t - cos\omega_0 T) + \frac{eE_0}{m_e \omega_0}(t - T) \sin \omega_0 T \tag{1.3}$$

The characteristic behavior described by the equations becomes evident when plotting them for various birth times (T). It becomes apparent that electrons return to the parent ion only during the first and third halves of the pulse. Electrons born at other times drift away from the parent ion as the pulse progresses. We can determine the recombination time by finding the roots of eq. 1.3 and calculate the kinetic energy

at that instant using eq. 1.2. The XUV photon will, therefore, have an energy of $\frac{1}{2}m_e v(t_R)^2 + I_p$ where t_R is the return/recombination time.

While the semiclassical three-step model provides an intuitive picture of the Higher Harmonic Generation (HHG) process, obtaining quantitative predictions such as the yield requires a quantum mechanical treatment. This is typically done by solving the Schrödinger equation under the strong field approximation (SFA). Additionally, two key approximations are made: the single active electron approximation (SAE) and the dipole approximation. The SAE assumption posits that only the outermost valence electron contributes to the HHG process, while the influence of all other electrons can be approximated using an effective potential. Meanwhile, the dipole approximation neglects the spatial variation of the external driving laser field, considering it to be uniform across the entire atom. This approximation is justified by the fact that the maximum distance traveled by the electron, typically on the order of the atomic size, is negligible compared to the wavelength of the driving laser. With these approximations, the Schrödinger equation reduces to the following form :

$$-i\hbar\frac{\partial}{\partial t}|\Psi(t)\rangle = (-\frac{\hbar^2}{2m}\nabla^2 + V(\mathbf{r}) - \mathbf{E}(t)\cdot\mathbf{r})|\Psi(t)\rangle \tag{1.4}$$

In this form, the Schrödinger equation can be solved using the split-operator method, which is a widely used numerical technique for solving time-dependent quantum mechanical problems. However, for the purposes of this thesis, we predominantly utilize the semiclassical model. Instead of directly solving the Schrödinger equation, we employ trajectory calculations [17] to estimate the variation in Higher Harmonic Generation (HHG) yield. This approach allows us to gain insights into the dynamics of the process while leveraging the simplicity of semi-classical methods.

1.2 Use of Two-Color fields

Two-color-induced photoionization has emerged as a powerful tool for manipulating and controlling the ultrashort dynamics of atoms and molecules, spanning from femtosecond to attosecond time domain [18–20]. Unlike the single-color scenario, the two-color approach provides additional degrees of freedom, including control over the relative two-color intensity, relative polarization, and relative phase. This motivates us to employ the two-color fields for controlling the tunneling electron trajectories to influence the energy distribution of the ejected electrons and thereby control the harmonic generation process [21–23].

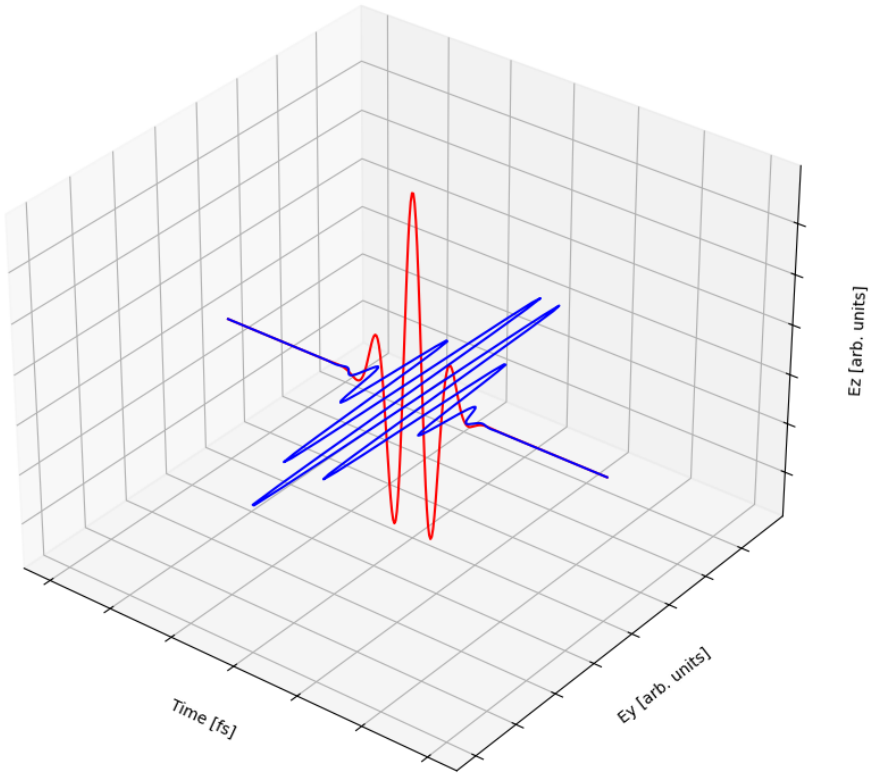

Figure 1.2: Representation of a Two-Color fields in Orthogonal configuration.

1.3 Objectives of this thesis

This thesis can be broadly divided into two parts. The initial part comprehensively discusses the design and development of an HHG spectrometer and its extension to perform two-color delay-dependent studies. The second part investigates the influence of the two-color phase and polarization on the HHG process in atoms and molecules. The detailed objectives are listed below.

- Develop a High harmonic generation spectrometer for producing (ultrashort) XUV pulses. This involves the design, construction, and optimization of the spectrometer to maximize the harmonic yield.
- Extend the capabilities of the HHG setup to enable Two-Color High Harmonic Generation. This involves modifying the existing setup to accommodate two-color laser fields and optimizing the macroscopic phase matching parameters for efficient generation of harmonics.
- Simulate the tunnel electron trajectories in high harmonic generation using both single-color and two-color laser fields and estimate the revisiting kinetic energy and yield.
- Investigate the processes involved in Two-Color HHG in Argon and Krypton, including the influence of various experimental parameters such as the intensity, polarization, and relative phase between the two laser pulses. Compare the obtained experimental results with theoretical results obtained using the simulation.
- Explore how molecular structure and dynamics influence the harmonic generation process using two-color laser fields.

1.4 Thesis Outline

This thesis has six chapters and is structured as follows :

1.4.1 Introduction

This chapter elaborates on the motivation and principles underlying Higher Harmonic Generation (HHG), emphasizing its significance in generating attosecond Extreme Ultraviolet (EUV/XUV) pulses. It offers an overview of attosecond physics, illustrating how ultrashort bursts of light are instrumental in studying ultrafast dynamics in atoms and molecules on the shortest achievable time scales. The discussion highlights the significance of high harmonic spectroscopy (HHS) as a probing technique capable of capturing sub-femtosecond nuclear and electronic dynamics. The chapter also discusses methods for achieving quantum control in atoms and molecules, highlighting the use of an additional pulse to manipulate the tunneling electron. By discussing these foundational principles and techniques, the chapter aims to equip readers with a basic understanding; necessary for subsequent developmental and scientific studies in this field.

1.4.2 Development of High Harmonic Generation setup

This chapter outlines the experimental methodologies used in this thesis, spanning from a detailed description of the femtosecond laser system and the methods used for its pulse characterization. The design and development process of the High Harmonic Generation (HHG) setup is discussed in detail, including initial simulations conducted using Zemax, the loose-focusing two-chamber geometrical design, the assembly of vacuum chambers, and the installation of a gas cell. Additionally, it encompasses the

construction of an XUV spectrometer, the development of data acquisition programs, along with the calibration of resulting spectra. Subsequently, a detailed optimization scheme with respect to the macroscopic phase matching variables is discussed.

1.4.3 Two-Color High Harmonic Generation

This chapter explores High Harmonic Generation (HHG) from Two-Color fields, a powerful extension of the traditional HHG setups. We begin by thoroughly examining the renowned 1D model [2], which serves as a fundamental theoretical framework for calculating HHG yield induced by a single-color field. Subsequently, we transition to discussing the essential experimental adjustments required for implementing the two-color HHG scheme. We obtain two-color HHG spectra from Ar and CO_2 and investigate how the two-color HHG yield varies concerning pressure and distance from the focal point (Z). Interestingly, while the model demonstrates good agreement with two-color HHG in Argon (Ar), it encounters limitations in explaining the observed behavior in Carbon Dioxide (CO_2). This highlights the potential constraints of the 1D model in capturing the complexities of molecules like CO_2 within the two-color regime.

1.4.4 Two-Color HHG in Atoms

This chapter delves into the exploration of Higher Harmonic Generation (HHG) from atoms (Ar, Kr, Xe) induced by Two-Color laser fields. The focus lies on understanding the role of tunnel electrons in the generation process and controlling them to achieve desired results. Various schemes were employed, including altering the two-color intensity, the relative polarization of the pulses, and the relative phase between them. Increasing the two-color intensity was found to correlate with a higher harmonic yield

across all studied atoms. A comparison between orthogonal and parallel polarization schemes in Argon revealed their differing impacts on higher harmonics (> 17). An experimental technique to generate a time delay between the two-color pulses is discussed. A significant aspect of this study involved investigating the dependence of the two-color phase on the HHG yield. It was observed that a relative phase delay between the two-color pulses influenced the trajectories of tunneling electrons, consequently modulating the HHG yield. The experimental findings were supported by theoretical simulations, which calculated the return kinetic energy and yield of tunneled electrons and compared them with experimental data.

1.4.5 Two-Color HHG in Molecules

This chapter expands the exploration of Two-Color Higher Harmonic Generation (HHG) to include molecules (N_2, CH_3Cl). A two-color phase-dependent study was performed in both N_2 and CH_3Cl in the PTC configuration and the results were compared with the simulation.

1.4.6 Summary and Future Outlook

In this chapter, the key findings from the two-color high harmonic generation (HHG) studies in atoms (Ar, Kr) and molecules (N_2, CH_3Cl) have been summarized. Future plans to expand the scope of research to include two-color HHG from CO, CO_2, and SO_2 have been outlined to better understand the role of molecular geometry and dipole moment in the harmonic generation process. Another area of interest is investigating the role of the tunneled electrons in facilitating the transfer of orbital angular momentum (OAM) to the resulting harmonics. Finally, leveraging the capabilities of the HHG beamline in combination with our VMI/COLTRIMS setup will open up the possibility

of performing XUV-IR experiments in the near future.

Chapter 2

Development of High Harmonic Generation setup

This chapter presents the experimental methodologies used in this thesis. For my Ph.D work, I developed the Higher Harmonic Generation (HHG) setup and used it to record the HHG spectrum of atoms and molecules induced by single-color (fundamental wave (FW), 800 nm) and two-color (400 nm + 800 nm) femtosecond laser pulses. The femtosecond laser system at PRL delivers 25 fs pulses at a repetition rate of 1KHz, with the 800 nm central wavelength being employed in this thesis. The developmental works cover the design and assembly of vacuum chambers, gas-line, tight-focusing and loose-focusing configurations of the HHG setup, XUV spectrometer implementation, data acquisition scheme, calibration procedures, etc. Prior to constructing the HHG setup, simulations were conducted using the Zemax software. Further, many simulations were performed to optimize the gas cell design, assess pressure/power effects on HHG, and evaluate optimal phase-matching conditions. The details about the design and development of the HHG setup, femtosecond laser system and its pulse charac-

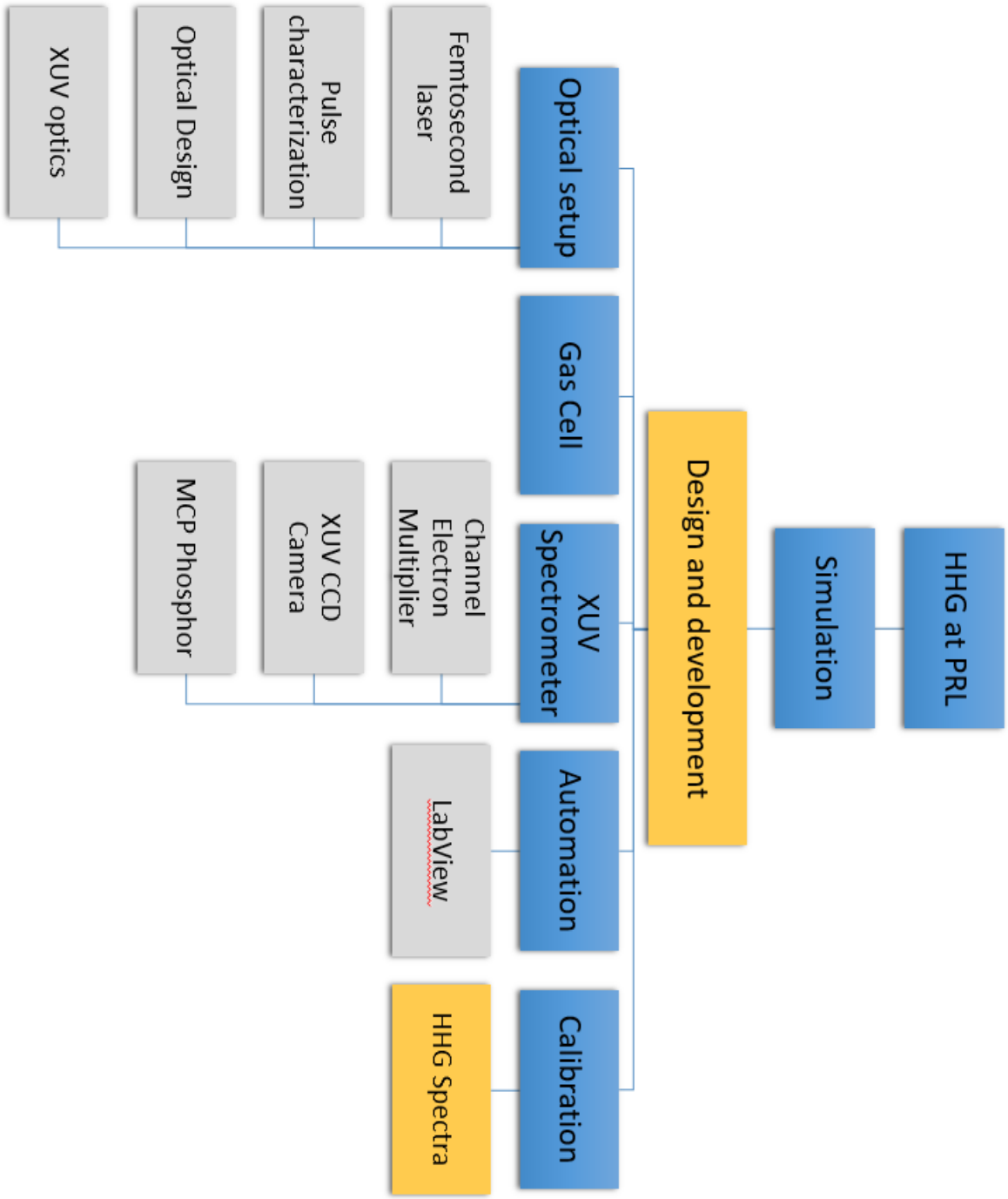

Figure 2.1: Schematic of HHG setup development at PRL.

terization, data acquisition scheme, etc., are discussed below. The flowchart shown in Figure 2.1 summarizes the key elements utilized in developing the HHG setup at PRL.

2.1 Experimental design of the HHG Setup

High Harmonic Generation (HHG) has been demonstrated using gases [24–28], liquids [29–31], and solids [32–35]. Among these, gases have been shown to produce the highest XUV flux. HHG in gases is influenced by a combination of microscopic factors, such as the intensity and wavelength of the input beam, and macroscopic factors, such as pressure and length of the gas cell and the positioning of the gas cell relative to the laser focus [2, 36–38]. HHG in gases has been typically carried out using two broad geometries resorting either to the loose-focusing [39, 40] regime or the tight-focusing regime[41–43]. Both regimes offer distinct spectral characteristics and flux and may be desirable based on the required application.

The choice of geometry determines the experimental design of the HHG setup. Both geometrical designs will be briefly discussed, although the HHG facility at PRL is based on the loose-focussing design.

It has been observed that the flux from loose-focussing geometry is typically better than tight-focussing. However, recent developments have shown improvements in the fluence of systems deploying tight-focusing [42].

2.1.1 Simulation

The geometrical setup under the loose-focussing design was simulated using the ray-tracing software Zemax to find the optimum position of the grating from the detector (Andor CCD 12 mm) for the wavelengths of interest (20-80 nm). This was useful to

determine the exact position of the HHG wavelength on the detector and their relative spacing. Various positions and angles of the grating and the position and thickness of the slit were checked to find the optimum parameters. This information was used to build special plates for isolating the detector from stray radiations that can flood the XUV detector.

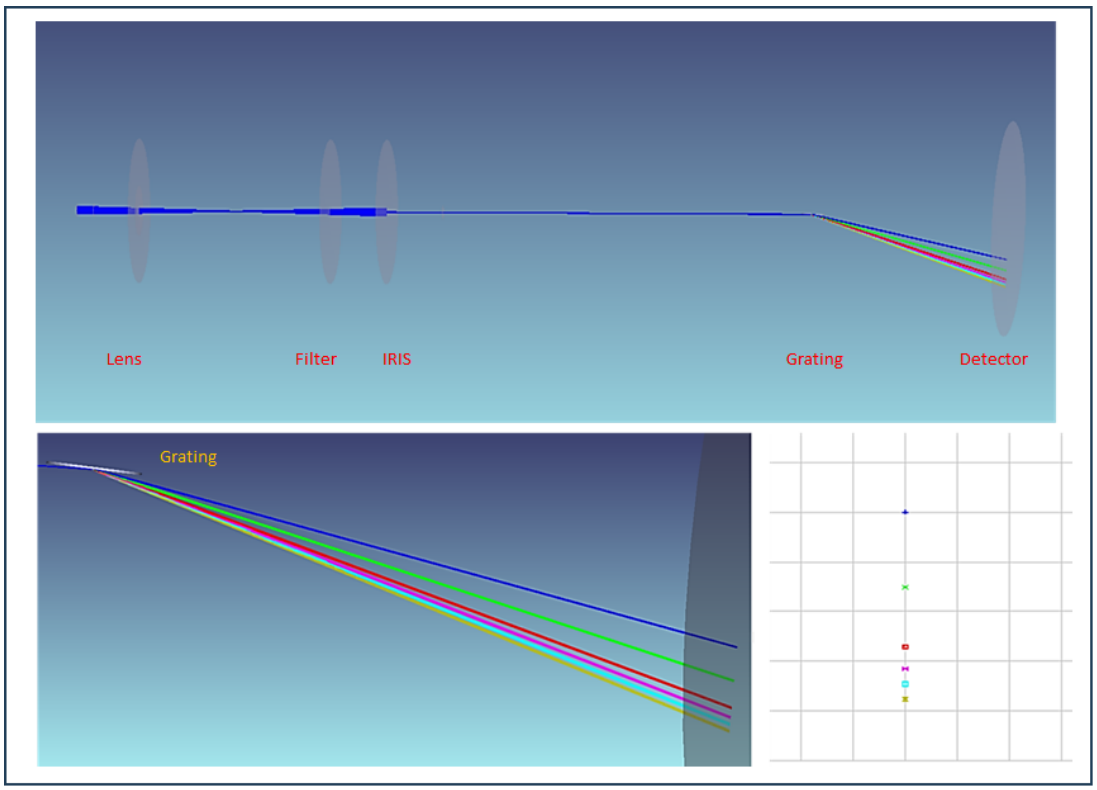

Figure 2.2: Ray tracing simulation based on the grating angle and position was carried out in Zemax. The grating separates the XUV beam based on wavelength (bottom left). The detector plane (bottom right) shows the position of different wavelengths on the detector.

A Python code was written based on the phase matching equation provided by E.Constant [2] to estimate the dimensions of the interaction length for efficient generation of HHG for our experimental setup. A scan over all the experimental parameters, such as the length of the gas medium, distance of the medium from focus and intensity were varied to check if the pressure required inside the gas cell lay within a reasonable

range. A suitable set of these four parameters provided important experimental data and paved the way for the commissioning of the actual HHG setup.

2.1.2 PRL Femtosecond Laser

Ultrafast lasers [44–48] operate within the picosecond to femtosecond time domain, representing a pinnacle of precision in optical systems. Leading this technological frontier are titanium–sapphire (Ti:Al_2O_3) based laser systems employing Kerr lens mode-locking [49, 50], capable of emitting pulses as short as 5 fs. These advanced lasers boast an exceptional average output power, frequently exceeding several hundred milliwatts, and feature a very high pulse repetition rate, such as 80 MHz. The resulting pulses, with durations of the order of femtoseconds or picoseconds, achieve staggering peak power levels ($> 10^{11}W$). These high power femtosecond lasers employ the technique of chirp pulse amplification which was one of the groundbreaking techniques to create the shortest and most intense laser pulses, for which a Nobel prize was awarded to Gérard Mourou and Donna Strickland in the year 2018. This technique aids in creating pulses of duration of a few tens of femtoseconds. This basically involves stretching a seed pulse, amplifying and then, compressing the amplified pulse. A typical femtosecond laser has four stages involved in generating the ultrashort pulses: i) Mode-locked Oscillator, ii) Pulse-Stretcher, iii) Amplification Unit, iv) Pulse compressor as shown in the block diagram below.

PRL houses the Coherent Legend Elite Duo system, which consists of a femtosecond oscillator (VITARA-T-HP) and an amplifier (LEGEND ELITE DUO HE+). The VITARA femtosecond oscillator produces 15 fs, 80 MHz pulses with 670 mW of average power. These pulses are then sent into an optically pumped multipass amplifier to produce 10 mJ, 1 KHz, and 25fs pulses at 800 nm.

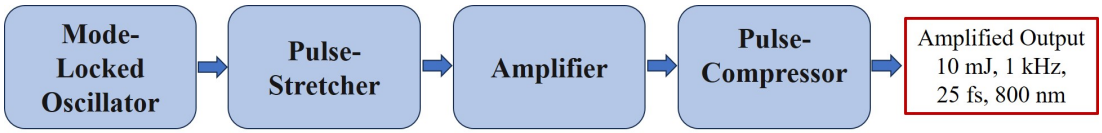

Figure 2.3: Representative scheme denoting the working principle of femtosecond amplifiers

The oscillator is based on the mode-locking principle in a cavity or a resonator. Generating short (nanosecond) to ultrashort (pico- to femtosecond) pulses requires maintaining a constant phase relation between adjacent modes, which is crucial. This process, known as mode-locking, involves stabilizing the phases of the modes or establishing a fixed phase relationship between adjacent modes. In a mode-locked oscillator, the modes periodically interfere constructively with each other, resulting in the generation of an intense burst or pulse of light. The four main parts of the oscillator are the pump laser(Nd:YLF laser), dispersion correction optical components, a collection of mirrors constituting the optical cavity/resonator, and a gain medium (Ti:Sapphire crystal) which is widely used in a solid-state laser due to its better thermal conductivity and broad gain bandwidth properties. There are active and passive ways of mode-locking techniques to ensure the fixed phase difference between the modes. Active mode-locking techniques utilize external signals, such as an electro-optic modulator, to modulate the light within the laser cavity. In contrast, passive mode-locking techniques employ an element inside the cavity to modulate the light. Passive mode-locking is based on the optical Kerr effect, which is a nonlinear response of certain optical media to the intensity of the laser beam passing through them.

Direct amplification of the oscillator pulses can potentially damage the Ti:Sapphire crystal. To address this issue, the concept of pulse stretching was introduced, proving to be an innovative and successful solution. The pulse is stretched to few nano-pico seconds. A filtered oscillator beam is passed through the stretcher part, which includes

gratings; the various frequency components experience different time delays. This effect, known as group velocity dispersion (GVD), leads to pulse broadening. Positively chirped pulses occur when the red frequency components experience less delay than the blue frequency components. This results in a pulse with its leading edge composed of red frequencies and its trailing edge composed of blue frequencies.

The regenerative amplifier operates similarly to the femtosecond oscillator, where the seed beam passes through the Ti: Sapphire gain medium multiple times without spatial separation for amplification. Pockel cells are employed to regulate the seed beam's passage. In the second stage, the amplified regenerative output passes through the single-pass amplification stage. At the PRL femtosecond laser lab, there is a regenerative femtosecond amplifier that generates laser pulses of 25fs duration at a repetition rate of 1KHz, with a wavelength of 800nm and an energy of 10mJ.

After the amplification stage, intense pulses produced have a long pulse duration (up to nanoseconds) and exhibit positive chirp (spectral components dephasing). To shorten the pulse duration to a few tens of femtoseconds and achieve intense ultrashort pulses, the pulses from the amplifier must undergo compression, which is enabled by a pair of gratings to down chirp and give a compressed output of 25fs.

2.1.3 Pulse Characterization

Accurate and reliable pulse characterization is essential for applications of femtosecond laser systems, especially for studying ultrafast processes. Pulse characterization refers to the complete determination and faithful reconstruction of the laser pulses emitted from femtosecond laser systems. While some information in this regard can be obtained from auto-correlation techniques, a complete characterization that gives information on the electric field versus time, the precise pulse shape and chirp of the

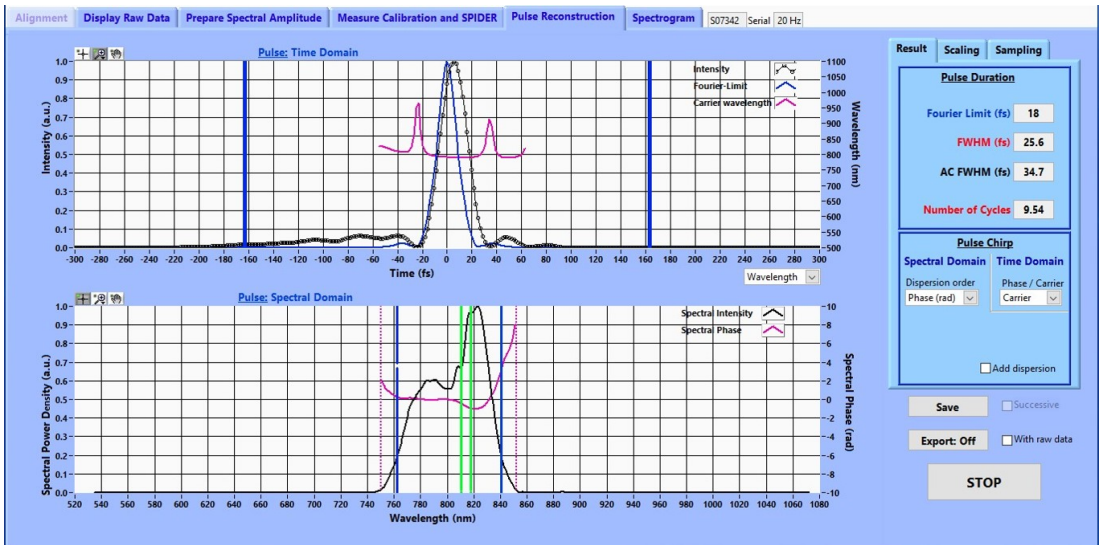

Figure 2.4: APE-SPIDER software window showing pulse measurement: 25.6fs FWHM.

pulses requires special techniques such as FROG, SPIDER etc. This is especially true when measuring asymmetrical pulses where ordinary auto-correlation techniques would always yield a symmetrical signal shape in the time domain. For a complete determination of the pulse amplitude and phase, we can take two approaches based either on the temporal or the frequency domain. In the temporal approach, measurements are conducted to precisely determine when a specific frequency occurs within a defined time interval or ”gate.” This is accomplished through the application of optical gating techniques, wherein the interference of a laser pulse with a delayed version is examined. The goal is to establish a high-frequency resolution of the pulse envelope, enabling the differentiation of various frequency components within the pulse. The emphasis lies in accurately controlling the timing of a particular frequency occurrence within the specified time window. The technique FROG does precisely this. In the frequency approach, measurements focus on determining the timing of a specific frequency component. One technique that adopts this approach is SPIDER (Spectral Phase Interferometry for Direct Electric-field Reconstruction). In the SPIDER tech-

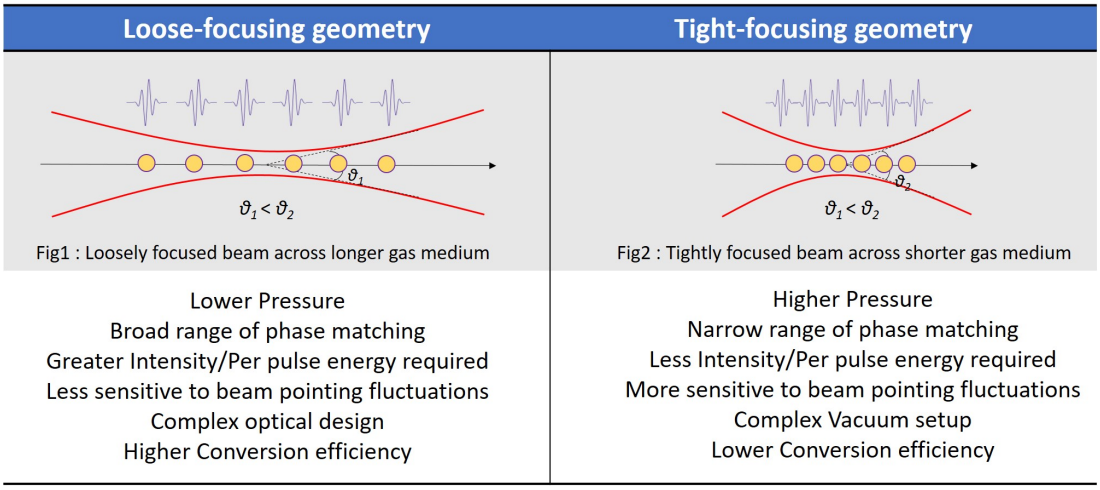

Figure 2.5: Comparison of the Loose-focusing and the short-focusing geometries in HHG generation.

nique, the input pulse is divided into two parts. One part traverses a delay line with group velocity dispersion, resulting in a pulse with a predetermined chirp. This chirped pulse is then used in a subsequent cross-correlation technique employing a nonlinear process such as SHG. In our lab, we use FC-SPIDER, which monitors the pulse duration of our femtosecond laser throughout the experiment duration, as shown in Fig.2.4. Now, I will discuss the HHG setup developed for this thesis work, beginning with the optical design.

2.1.4 Optical Design

As mentioned earlier, both optical designs [51] based on either the loose/long-focusing geometry or the tight/short-focusing geometry can be utilized for HHG generation. Figure 2.5 in table form outlines the key characteristics of both designs. A notable difference lies in the energy and pressure requirements. The loose-focusing geometry requires lower pressure but higher per-pulse energy, whereas the tight-focusing geometry requires higher pressures but can operate with lower per-pulse energies.

At the time of development of the HHG setup at PRL, we were limited by 1mJ laser power. We tried to strike a balance between the two optical designs when developing the setup at PRL. We used a 750mm lens to loosely focus the laser onto the gas cell, maintaining the pressure at a few tens of millibars. This configuration allowed us to generate up to the 25^{th} harmonic in Argon using 0.7mJ, 25fs, 800nm pulses at a 1KHz repetition rate.

The loose focussing geometry

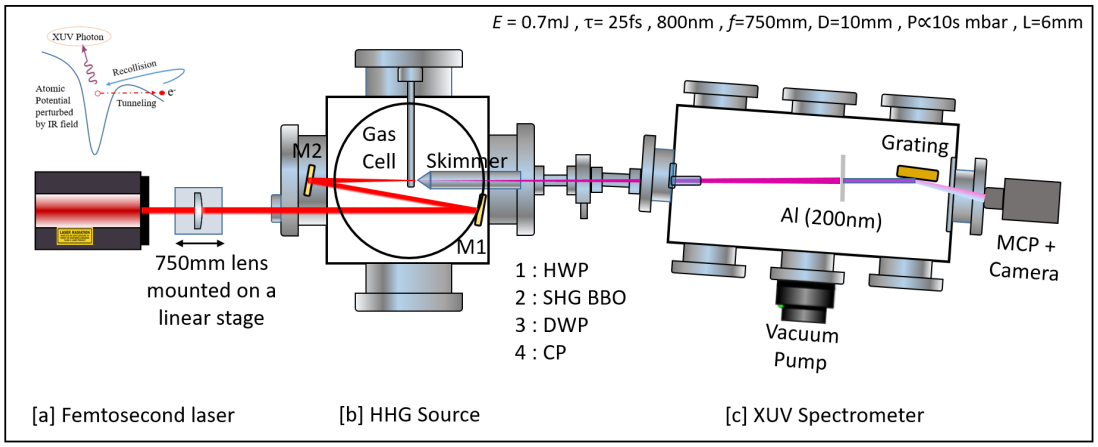

Figure 2.6: A schematic of the High Harmonic Generation Spectroscopy setup. [a] Femtosecond Laser (10 mJ 25fs 1 KHz), [b] Gas chamber housing mirrors and a gas cell, [c] XUV detection chamber housing aluminium filters, concave flat field grating (300 lines/mm) and an MCP camera for detection.

A schematic of the experimental setup for High Harmonic Generation (HHG) under the loose-focusing geometry is shown in Figure [2.6]. The setup consists of two vacuum chambers: a generation vacuum chamber and a vacuum detection chamber. The generation vacuum chamber Figure [2.8] houses beam routing optics and a gas cell, whereas the detection vacuum chamber houses an XUV spectrometer consisting of aluminum filters, an XUV grating, and an MCP-Phosphor camera detector for detection of the higher harmonics. The two vacuum chambers are connected using a

CF-35 bellow at a 3-degree angle with respect to each other. The vacuum chambers are separated using an in-house-designed conical tube that acts like a skimmer. The skimmer ensures that the XUV beam generated is transported into a separate region with a better vacuum. The conical end of the skimmer was kept 10 mm away from the gas cell to avoid re-absorption of the XUV beam generated from the gas cell by flooding the skimmer pipe. The incoming beam is folded onto the gas cell using the beam routing mirrors in the Z-shaped geometry.

2.1.5 XUV Optics

XUV (Extreme Ultraviolet) optics play a crucial role in handling the high harmonic radiations. Unlike conventional optics for visible light, XUV optics operate in a regime where traditional materials like glass become opaque. To circumvent this limitation, XUV optics typically function in reflection mode. Specialized techniques are needed to handle and focus these high-energy photons. Grazing incidence mirrors made of iridium or silicon carbide are commonly employed, reflecting the XUV radiation at very small angles. Additionally, multilayer coatings with alternating high and low-density materials can be used to create diffraction gratings to isolate specific harmonic frequencies. At PRL, we used a gold-coated aberration-corrected concave grating from Shimadzu (30-002) operating in the 20 nm - 80 nm wavelength range to separate and focus the harmonic radiations onto the detector in a flat-field configuration. The same setup can be adapted to focus the harmonics onto samples of interest for probing their electronic properties. Additionally, ultrathin (200 nm) metallic filters are utilized to selectively transmit desired XUV wavelengths while blocking the incident IR radiation.

2.1.6 Gas cell

The gas medium for efficient HHG generation is based on the phase-matching parameters suited to the type of geometry employed. The medium plays a key role in determining the efficiency and characteristics of the harmonics emitted. The experimental schemes for HHG have employed several types of mediums such as the gas jet [37], semi-infinite [52] and finite [53] gas cell, hollow-core gas cell [54, 55], wave guides [56–58] and capillaries [59].

Gas Jet: A gas jet is one of the most common configurations employed for generating HHG. It releases a continuous or pulsed jet of gas from an orifice into an interaction region of the laser beam. While this configuration is easy to implement, the interaction length is limited by the jet thickness. This poses a limit on the XUV flux generated. In addition, gas jets are often backed by very high gas pressures posing difficulty in maintaining ultra-high vacuum in the gas chambers without some special arrangements. While this problem can be bypassed using a pulsed gas jet, the time synchronization of the laser with the opening of the orifice becomes experimentally challenging.

Semi-Infinite Gas Cell: In this setup, a semi-infinite gas cell is employed, where the laser beam interacts with the gas medium over an extended length. This configuration aims to maximize the interaction length and enhance harmonic yield. Due to a larger medium length, the gas cell pressures can be lower, making it possible to bypass the vacuum-based challenges of employing a gas jet design. This configuration was employed in our HHG setup. However, achieving a uniform gas density over the extended interaction length is a challenge and may need to be accounted for in the theoretical phase matching estimations using a special gas profile. In addition, the length

of the medium must be carefully estimated based on the phase-matching calculations to limit the effects of dispersion and reabsorption of XUV.

Wave-guide: In this configuration, the gas medium is confined within a tube, guiding the laser pulse through the center. This replaces the Guoy phase component in the phase matching equation which varies as a function of the distance from laser focus with a fixed term dependent on the width of the waveguide. This may create conditions for efficient phase matching inside the medium, producing enhanced HHG flux.

Theoretical Estimations for the medium dimensions

The choice of the type of gas cell is determined by estimations of its dimensions from the input laser parameters and vacuum conditions. The following table in Fig.2.7 lists the required threshold intensity I_t, maximum length, and diameter of the gas cell. This provides us with an upper limit for constructing our gas cell.

Parameters	Formula	Description
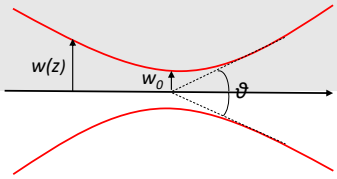	$w(z) = w_0\sqrt{1+\left(\frac{z\lambda}{\pi w_0^2}\right)^2}$	Beam waist
	$I_t = \frac{2c\varepsilon_0 m\omega^2}{3.17\cdot e^2}(qh\nu - I_p)$	Threshold Intensity for q^{th} harmonic
Length of medium	$L_{max} = \frac{8f_\#^2}{\pi}\cdot\sqrt{\frac{I_0}{I_t}-1}$	Max length beyond which phase mismatch happens
Diameter of medium	$D_{max} = \frac{\lambda f_\#}{\pi}\cdot\sqrt{8\ln\left(\frac{I_0}{I_t}\right)}$	Radial disc within which generation happens

Figure 2.7: Gas cell parameters for producing q^{th} harmonic [2].

In our HHG setup, the gas cell is made using a 1/4” Swagelok stainless steel pipe

with its wall thickness reduced to 0.5 mm. The open end of the pipe is sealed, and the other end is connected to the gas line through a vacuum feedthrough. The gas cell is placed perpendicular to the direction of the input laser beam. The mounting was secured using a special in-house-designed holder to keep the gas cell still at all times during the experiment. The femtosecond laser (800 nm, 25 fs, 1 mJ) pulses were focused to drill holes in the stainless steel pipe. The laser was passed through for about a half hour until cleaner holes on both sides of the cell appeared. The thickness of the holes was measured using a microscope and found to be about 100 microns on the input side and 50 microns on the output end. The gas cell made using this technique can act as a self-aligning tool for the alignment of the rest of the setup. This proved to be very useful because the alignment of any HHG setup is challenging, as the XUV beam cannot be visibly traced, and the detector is typically 1.5 - 2 m away from the gas cell.

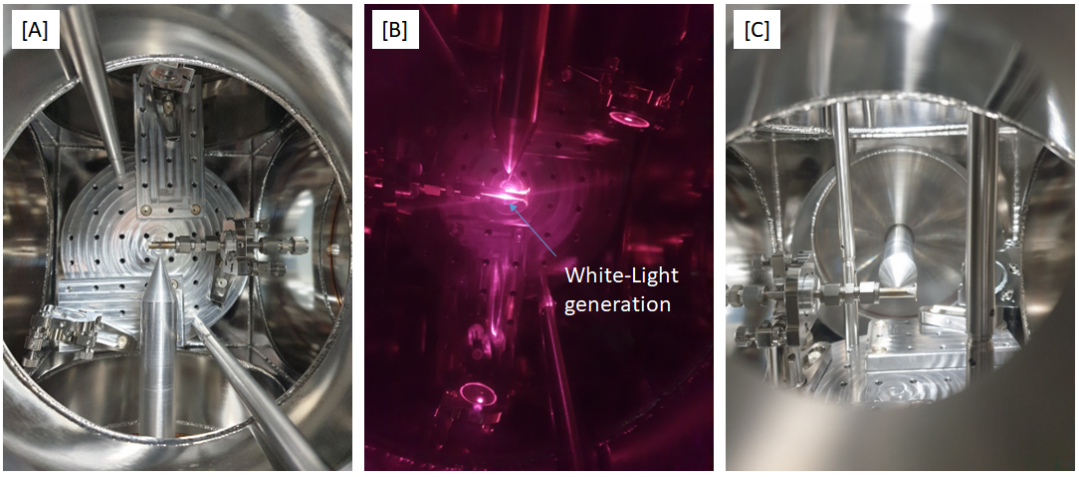

Figure 2.8: [a] Top view of the gas chamber containing mirrors M1 and M2, the gas cell and skimmer pipe. [b] Laser focused on the gas cell producing HHG [c] Gas cell as seen from the alignment viewport.

The gas is allowed into the gas cell in two stages to maintain a constant pressure of a few tens of millibars. To begin with, gas pressure from the cylinder is main-

tained at around 1200 mbars. The gas is then inlet through a needle valve to control the flow rate and reduce the pressure to a few tens of millibars. An additional needle valve (Swagelok) is connected in series, which provides finer control of the gas pressure inside the gas cell, resulting in a stable pressure throughout the measurement. The pressure was typically within 1 mbar of the set value at the end of 1 hour, and it was measured using a vacuum gauge (Pfeiffer RPT-200) right before the vacuum feedthrough of the gas cell.

2.1.7 The XUV Spectrometer

The XUV beam generated from the gas cell is skimmed into the XUV Spectrometer chamber through a 1mm skimmer placed 10 mm after the gas cell [Figure 2.8]. This provides a better (vacuum) environment for the XUV beam produced. The entire journey through the spectrometer can be broken down into the following steps.

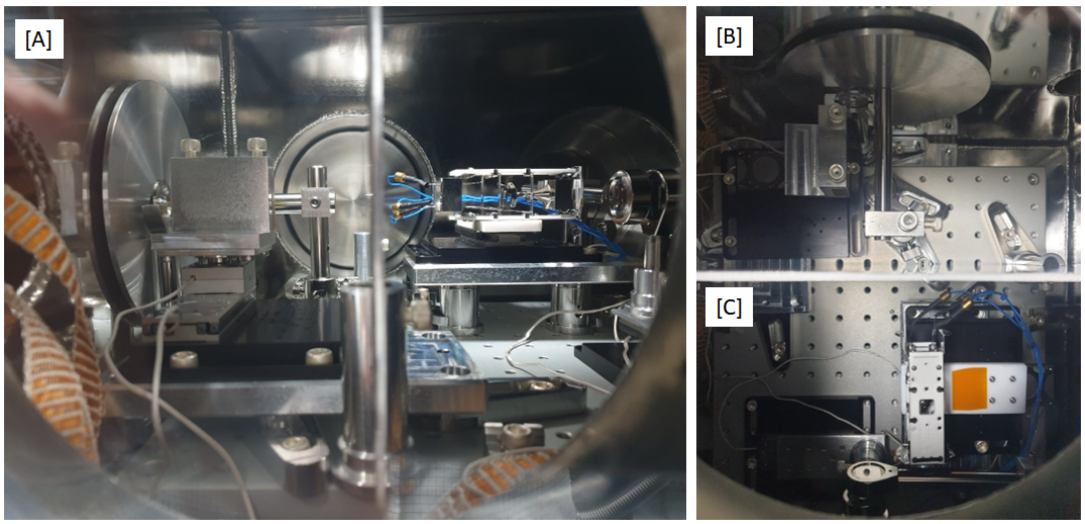

Figure 2.9: [A] Side view of the detection chamber housing [Right to Left] a slit, aluminium filter, Channel Electron Multiplier (CEM), an aluminium partition, grating mounted on a rotation and linear (Z) stage, exit side filter and the detector opening; [B] Top view of XUV grating; [C] Top view of CEM.

Beam Alignment and Selection: The beam enters the spectrometer chamber through a custom made 3-degree alignment tool and travels through an aluminium pipe with a 5 mm pinhole at its end. This alignment tool is crucial for maintaining the angle of the input beam with respect to the grating at 3 degrees for best performance. The pinhole selects the centremost portion of the diverging beam. Since the divergence of the XUV beam is less than that of the IR beam, the pinhole ensures that only the region containing the XUV beam is selected while the rest is discarded. The residual beam hits the aluminium cap and bounces off within the pipe multiple times before dampening out. This is important for reducing the background noise, which can show up on the very sensitive XUV camera as stray radiation.

IR Blocking: The remaining (centremost) XUV+IR beam hits the 200 nm Al filter which blocks the IR and allows only the XUV to pass through. The IR beam gets reflected and goes back and forth between the filter and the aluminium pipe resulting in damping.

XUV Detection: The filtered XUV beam is directed onto a Channel Electron Multiplier (CEM) mounted on a linear vacuum stage as shown in [Figure 2.9 [C]]. The CEM serves as a sensitive detector for XUV radiation, as the incoming XUV ionizes electrons within its collecting cone, generating a detectable signal at the anode. This signal is monitored using an oscilloscope to confirm XUV production, with an increase in gas pressure resulting in a corresponding increase in the CEM signal. To confirm that the XUV signal is indeed a result of HHG, the polarization of the input beam is changed from linear to circular, directly influencing the tunnelled electron in the HHG process and resulting in a decrease in XUV production. This change is reflected in the oscilloscope signal, providing additional confirmation of the XUV radiation detection.

Spectral dispersion: Once the production of XUV is ensured, the beam is passed

onto a slit. The slit width along with parameters such as the groove density and focal length of the grating, as well as detector pixel size, collectively determine the resolution of the spectrometer. Subsequently, the beam from the slit is directed onto the grating [Figure 2.9[B]] through a 10 mm aperture in the partition. This partition prevents the stray radiations from reaching the detector.

The grating disperses different harmonics onto different paths based on their wavelength. The position and angle of the grating are crucial for observing a strong HHG signal. The XUV grating is particularly sensitive to the input angle stated by the manufacturer. The grating was therefore mounted on a linear and rotation stage for optimization with the input beam. We used a 300 lines/mm gold-coated concave grating from Shimadzu to produce a flat field image on the detector.

Harmonic detection: The dispersed harmonics are passed through another 200 nm Al filter to further isolate the XUV signal before being detected either by an MCP/phosphor detector or an XUV camera. During the initial commissioning phase of an HHG setup, it is recommended to prioritize the utilization of an MCP-Phosphor detector over an XUV camera. The MCP-Phosphor detector presents several advantages, notably its larger cross-sectional area and immunity to stray Infrared (IR) radiation, which could potentially blind an XUV camera. Additionally, this detector simplifies the alignment process, providing much-needed ease during the initial setup and calibration. The detector can be later replaced with an XUV camera if finer spectral structures within the harmonics or absolute photon numbers/efficiency are of interest.

2.1.8 Data Acquisition Scheme

Data acquisition from the experimental setup was conducted using LabVIEW software, facilitating seamless interfacing of various components. Three separate pro-

grams were written for this purpose. The first program controlled the rotational and linear stages of the grating, enabling optimization of its angle and position with respect to the input beam. A comprehensive scan was performed, ranging from -5 mm to 5 mm and -2°to 2°, to identify the optimal grating position yielding the highest HHG flux.

The second program was designed for data accumulation using the MCP-Phosphor camera. All studies concerning the optimization of phase matching conditions using both single and two-color pulses utilized this program.

The third program facilitated the investigation of the two-color pump-probe delay effect on atoms and molecules. By interfacing with the calcite plate mounted on the delay stage and the XUV spectrometer's camera, this program allowed for varying time delays between the two-color pulses. Data accumulation was done at each delay setting, enabling a detailed analysis of the temporal dynamics. A block diagram illustrating the functionality of this program has been provided in the Appendix.

2.1.9 Calibration

Fig [2.10 [A]] shows the first HHG signal observed using the ANDOR (Ikon-M) XUV camera. The calibration of the HHG spectra refers to the conversion of raw experimental data (i.e., the X-axis denoting pixels) into quantitative information about the wavelength of the harmonic orders produced. This is typically achieved by referencing the harmonic signals to known spectral lines of gases such as helium, neon, etc., or using the absorption edge of the filters employed. For the calibration of the PRL's HHG setup, the absorption edge of Sn was used. As evident from the transmission curve, Sn exhibits a sharp absorption at 50 nm. This corresponds to the 17th harmonic (the 16th harmonic being even is not expected in the HHG signals from atoms), which

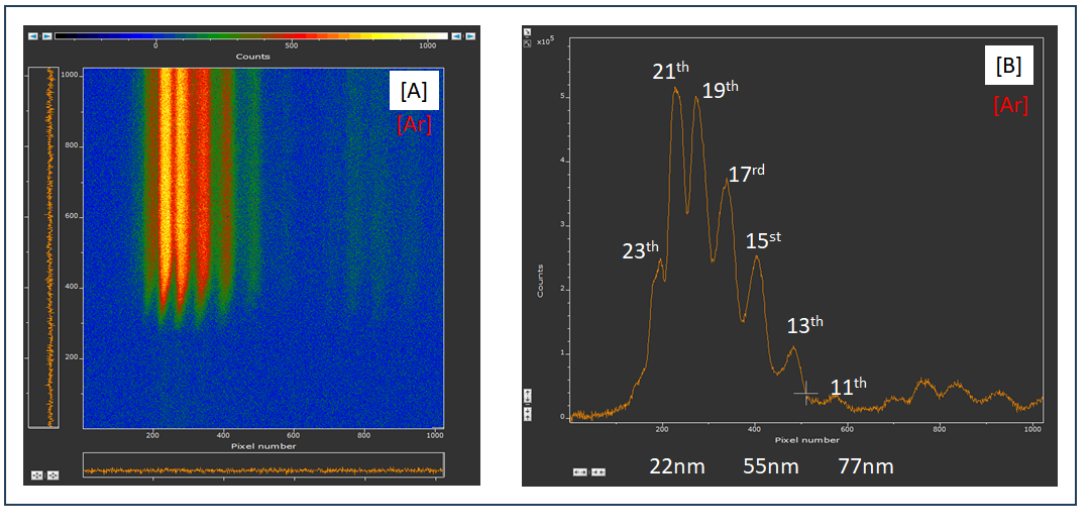

Figure 2.10: [a] First HHG signal observed from Argon using an Andor ccd camera [b] Flux vs Wavelength obtained by projecting the raw data onto the wavelength axis

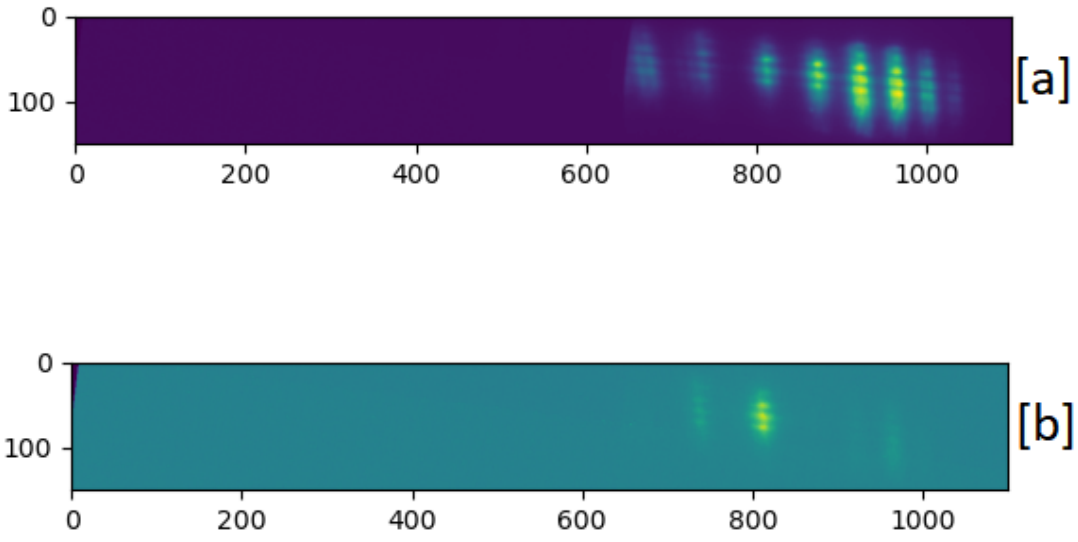

Figure 2.11: [a] HHG from Argon. [b] HHG obtained using a Sn filter in the path. The input parameters were 0.7 3mJ, 800 nm 35 fs, and 10 mm beam.

is expected to vanish in the presence of an Sn filter. This phenomenon is depicted in Figure [2.11], observed using an MCP-Phosphor detector. Fig [2.11[b]] shows the effect of a 200 nm Sn filter on the HHG data of Argon and compares it with the raw experimental data shown in Fig [2.11[a]].

The complete calibration process is illustrated in Fig[2.12] and Fig[2.13]. Raw HHG projection data for Argon is depicted in the Figure [2.12][a], while data using a Sn filter is presented in the Figure [2.12][c]. In Figure [2.12][d], a comparison is made between the theoretical estimation of the HHG yield, obtained by multiplying the Transmission Curve for Sn (NIST dataset) ([2.12][b]) with the HHG spectra of Argon; and the experimental results shown in Figure [2.12][c].

Notably, the nature of yield and positions of the respective peaks closely align with the estimated graph, validating the calibration process. A closer examination indicates that the harmonic vanishing at the 890th pixel may be the 17th harmonic. This can be clearly seen in Fig [2.13], where all the previous HHG curves have been overlapped. This figure provides a comprehensive view of the calibration process for the setup. The bottom axis represents pixels, while the top axis represents wavelength. With this, the calibration process is complete, and the cutoff peak is identified as the 25^{th} harmonic.

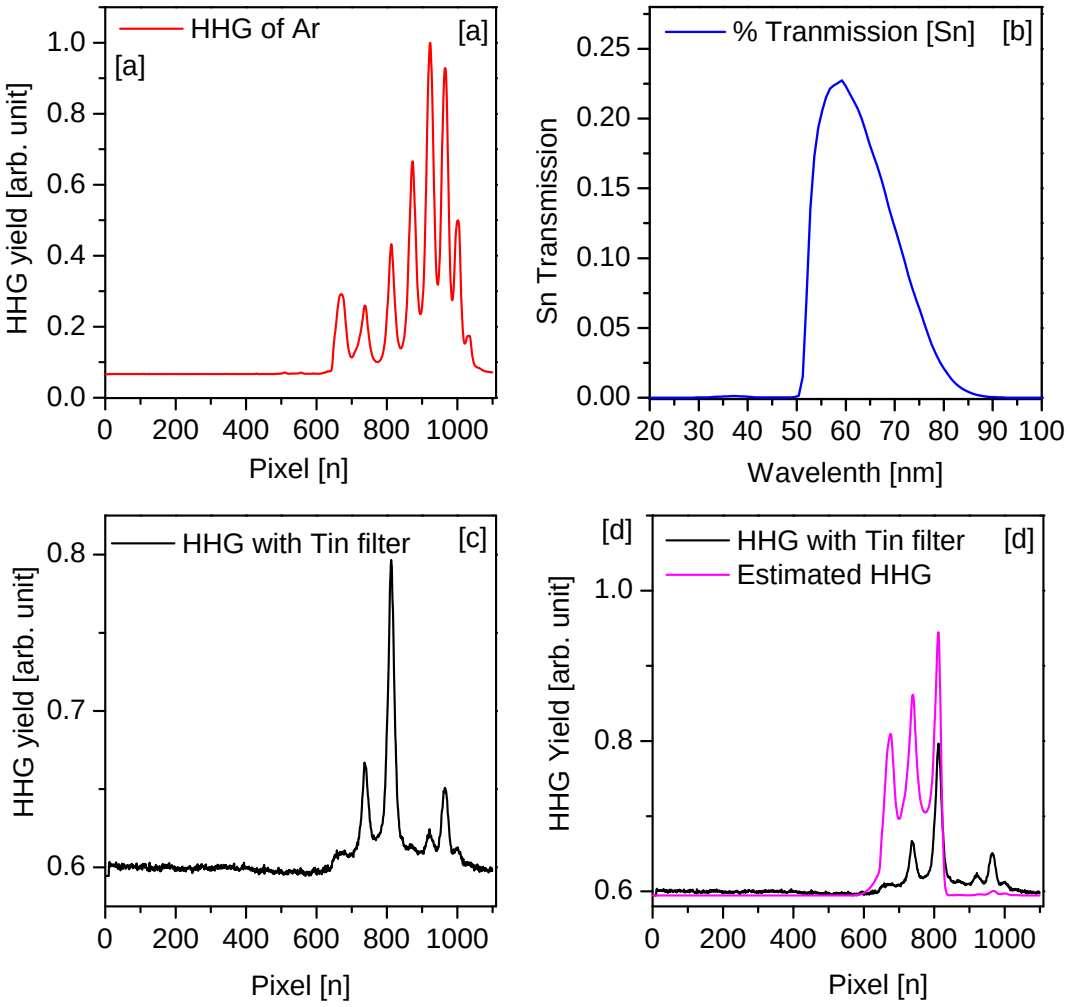

Figure 2.12: [a] HHG data from Argon [b] Transmission curve for Sn [c] HHG data from Argon using a 200nm Sn filter [d] Comparison of the theoretically estimated curve (magenta) with the experimental curve in [c].

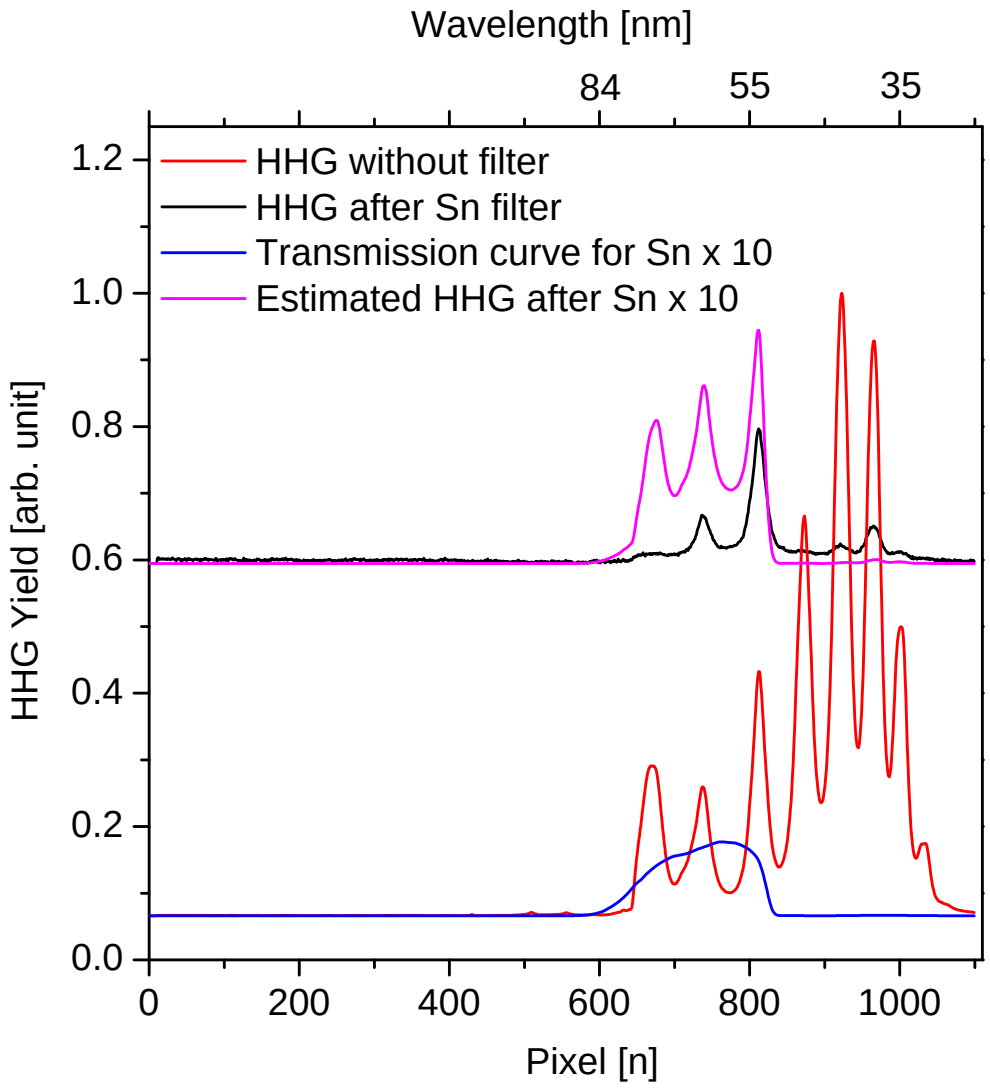

Figure 2.13: Calibration of the HHG signal. Overlap of the estimated (black) and observed (magenta) HHG signal using a Sn filter validates the calibration process. Note that the first peak is the 2^{nd} order signal from the 21^{st} harmonic and not the 11^{th} harmonic.

2.1.10 Experimental Optimization of the HHG signal

Once an HHG signal is obtained, immediate efforts can be put in to maximize the efficiency of the generation process. This is typically done by scanning through a range of phase-matching parameters such as the Intensity of the input laser, Iris diameter, distance of the laser focus from the medium, length of the gas cell, and pressure inside the gas cell. By optimizing these parameters, we aim to minimize the phase mismatch between the wave vectors of fundamental and harmonic radiation across the length of the medium, leading to a coherent buildup of the harmonic beam. In simpler terms, the phase mismatch signifies how much their "wavefronts" are out of sync as they propagate through the medium. This total phase mismatch can be broken down into its 4 constituents and quantitatively captured using the following equation[ref]:

$$\Delta k = \Delta k_{\mathrm{n}} + \Delta k_{\mathrm{fe}} + \Delta k_{\mathrm{foc}} + \Delta k_{\mathrm{i}}.$$

where Δk_{n} denotes the phase mismatch due to neutral plasma dispersion, Δk_{fe} is the mismatch as a result of dispersion due to free electrons, Δk_{foc} denotes the mismatch due to Guoy phase and Δk_{i} is the dipole component of the phase mismatch.

The HHG photon flux along the axis of propagation per unit time can be calculated using the following formula given by E.Constant [2]:

$$N = \rho^2 \cdot A_q^2 \frac{4L_{abs}^2}{1+4\pi^2(L_{abs}^2/L_{coh}^2)} \left[1 + exp(-\frac{L_{med}}{L_{abs}}) - 2cos(\frac{\pi L_{med}}{L_{coh}})exp(-\frac{L_{med}}{2L_{abs}})\right] \tag{2.1}$$

A detailed discussion of this model and all its parameters in the context of Two-Color fields has been done in Chapter 3. Here, we shall briefly discuss the effect of

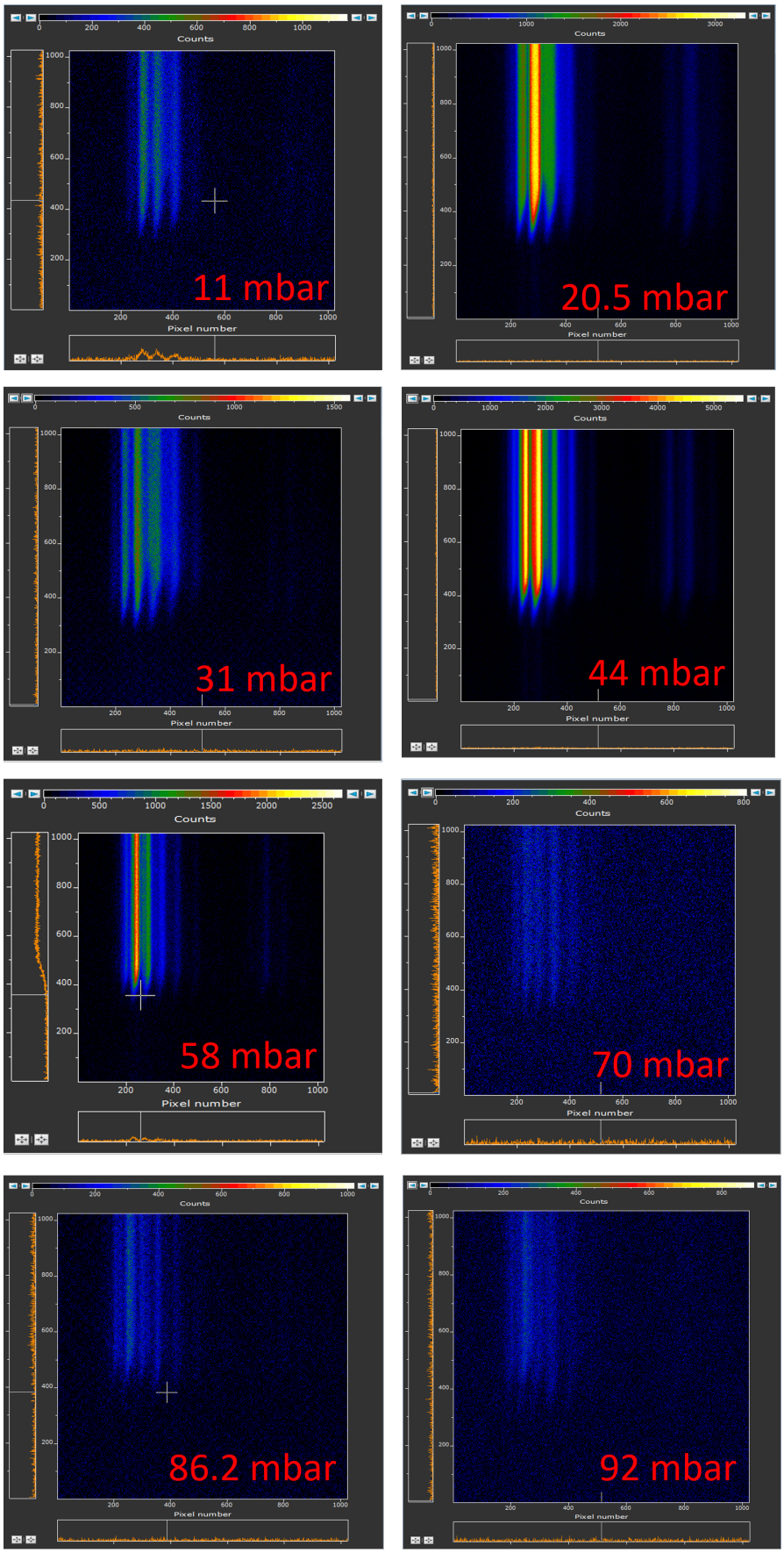

Figure 2.14: HHG signal from Argon at different pressures for 0.73 W of input laser.

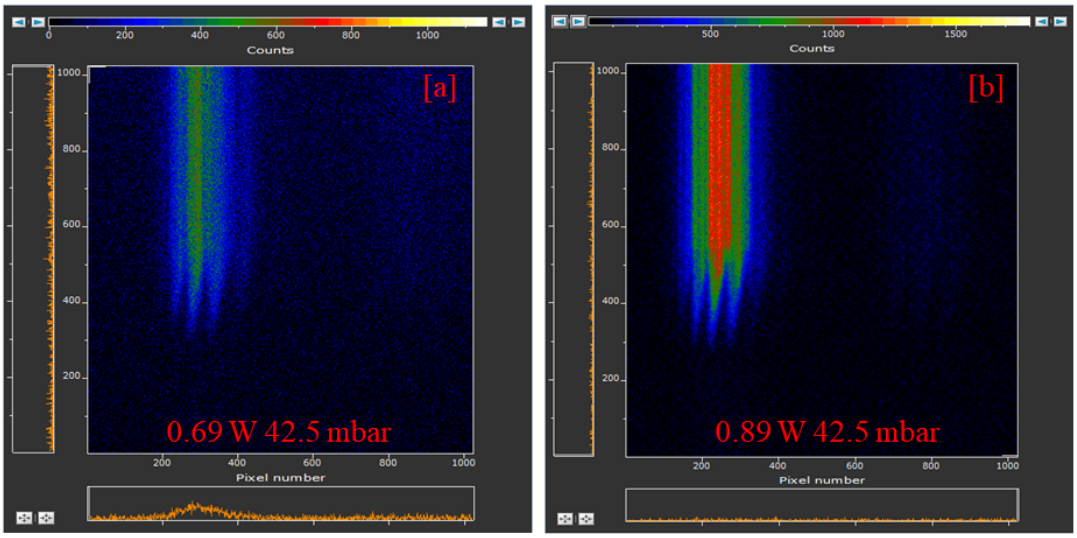

Figure 2.15: Effect of laser intensity on the HHG yield.

Pressure, Intensity, and Z on the HHG yield. Our results are in good agreement with other setups across the world [36, 38, 39, 43, 60, 61].

Pressure

The HHG spectrum at four different pressures is shown in Figure 2.14. It is clear from this figure that the HHG yield is dependent on the pressure, and the yield is highest at 44 mbar. To understand the details about the phase matching and the pressure dependence HHG yield, we have performed the 1D-model simulation, and the results are discussed in Chapter 3.

Intensity

The effect of Intensity on the HHG yield is complex and topic of research even today [62, 63]. As laser intensity increases, the HHG yield initially increases as well. This is because a stronger electric field in the laser pulse facilitates the ionization of the gas atoms and subsequent acceleration of the freed electrons. These accelerated electrons then recombine with the parent ion, emitting high harmonic radiation in the

process. However, this increase in yield doesn't continue indefinitely. Beyond a certain intensity, a further increase in laser power can actually lead to a decrease in the HHG yield. This is because, at very high intensities, the laser field becomes strong enough to ionize a significant portion of the species (gas atoms). This excessive ionization disrupts the optimal conditions for phase matching by creating an imbalance between the neutral and free electron dispersion. Therefore, for a particular harmonic of interest, the optimal intensity lies within a lower limit characterized by the ionization energy of the generating medium and the upper limit determined by the phase-matching conditions. For higher harmonics, the difference between the two intensities keeps on reducing. The harmonic for which the two intensities are equal is called the cut-off harmonic.

The effect of intensity on the HHG yield from Argon has been shown in Fig [2.15] for two different laser powers (0.69 mJ and 0.89 mJ) at 42.5 mbar pressure. Higher power shows the splitting of individual harmonic peaks due to contributions to the HHG radiation from both short and long trajectories of the tunneled electrons.

Z-dependence

Z-dependence determines the distance of the laser focus from the gas cell and impacts the Guoy phase, thereby affecting the phase-matching conditions. The graph in Fig[2.16] shows how the yield remains maximum up until a certain point and then starts to fall.

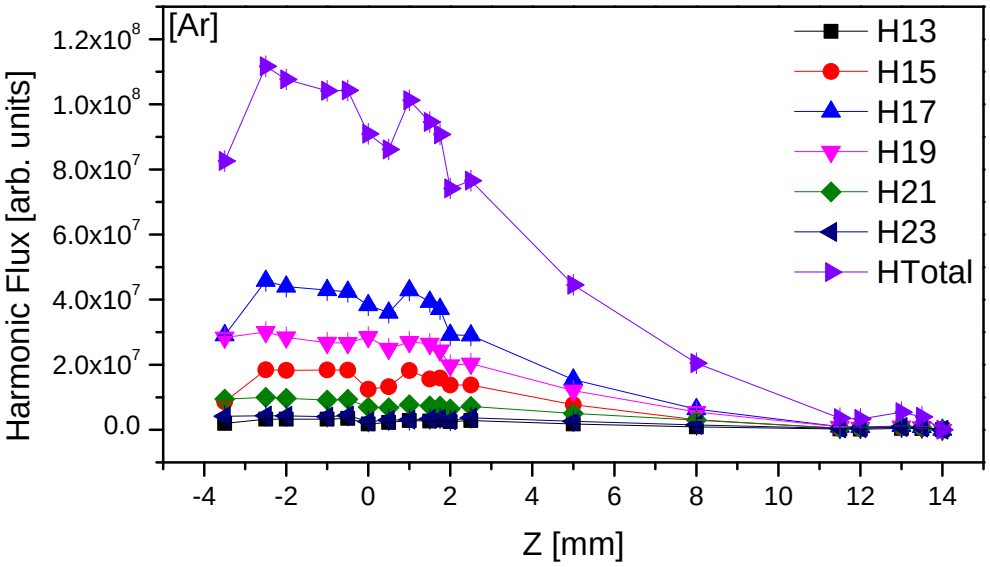

Figure 2.16: Distance of gas cell with respect to the laser focus [positive direction denotes gas cell is ahead of laser focus].

2.1.11 Summary and Conclusions

This chapter comprehensively covers the design and development of a High Harmonic Generation (HHG) setup, including key components and experimental procedures. It begins with an introduction to the PRL femtosecond laser system, followed by a brief overview of two prominent HHG geometries. The PRL HHG beamline, developed based on the loose-focusing design after the simulations conducted using Zemax for setup optimization is discussed in detail.

The gas chamber and XUV spectrometer are extensively discussed, covering various aspects such as experimental design, gas cell configuration, filters, Channel Electron Multiplier (CEM), grating, and detectors. Calibration of the spectrometer was done using the absorption edge of a Sn filter.

Furthermore, data acquisition and automation were facilitated using a home-built

LabView software, streamlining the data acquisition process. Optimization for maximum HHG yield was carried out by adjusting macroscopic variables, including pressure, intensity, iris diameter, and distance from the focus. This comprehensive overview provides a deep insight into the development of an efficient HHG setup, laying the foundation for further experimentation and research in the field of Attosecond physics.

Chapter 3

Two-Color HHG setup

This chapter explores Two-Color High Harmonic Generation (HHG), a powerful extension of the traditional HHG setup. We begin by establishing a theoretical foundation through a detailed discussion of the well-known 1D model [2] for calculating the HHG yield. This model serves as a benchmark for understanding the HHG process induced by a single color field. Following the theoretical background, we describe the necessary experimental modifications to implement the two-color HHG scheme. We then present the results obtained using this technique, including the two-color HHG spectrum of various atoms and molecules. We specifically investigate how the two-color HHG yield varies with pressure and distance from the focal point (Z). These experimental results are compared with predictions from the 1D model for single-color HHG. Surprisingly, the model shows good agreement for two-color HHG in Argon (Ar). However, it fails to fully explain the behavior observed in Carbon Dioxide (CO_2). This suggests potential limitations of the 1D model for complex molecules like CO_2 in the two-color regime.

3.0.1 1D-model for calculating the HHG Yield

The HHG photon flux along the axis of propagation per unit time can be calculated using the following formula given by Constant et al. [2]:

$$N = \rho^2 \cdot A_q^2 \frac{4L_{abs}^2}{1+4\pi^2(L_{abs}^2/L_{coh}^2)} \left[1 + exp(-\frac{L_{med}}{L_{abs}}) - 2cos(\frac{\pi L_{med}}{L_{coh}})exp(-\frac{L_{med}}{2L_{abs}})\right] \tag{3.1}$$

where L_{med} is the length of the gas medium, L_{coh} is the coherence length of the harmonic field generated, and L_{abs} is the absorption length. A_q represents the dipole amplitude of the q^{th} order harmonic. The phase mismatch Δk between the fundamental field and the q^{th} harmonic field in the High harmonic Generation is influenced by several contributing factors. These factors encompass dispersion within the neutral medium (Δk_{at}), the presence of free electrons (Δk_{fe}), the effects of laser focusing (Δk_{foc}), and the dipole phase contribution (Δk_i).

The overall phase mismatch (ΔK) is the sum of the individual contributions:

$$\Delta k = \Delta k_n + \Delta k_{fe} + \Delta k_{foc} + \Delta k_i. \tag{3.2}$$

Dispersion in the neutral medium (Δk_n): This aspect stems from variations in refractive indices (n) between the fundamental frequency (n_1) and the harmonic frequencies (n_q) situated above the ionization threshold. When $n_1 > 1$ and $n_1 > 1$, this contribution yields a positive effect. The formulation for Δk_n hinges on the polarizability α at frequency $q\omega$:

$$\Delta k_n = q\omega\rho \cdot (2\varepsilon_0 c) \cdot (1-\eta_{fe}) \cdot (\alpha_1 - \alpha_q). \tag{3.3}$$

In this equation, ρ signifies the atomic density of the medium, ε_0 represents the vacuum permittivity, c denotes the speed of light, and η_{fe} accounts for the ionization degree within the medium.

Inclusion of Free Electrons (Δk_{fe}): This factor accounts for the influence that free electrons within the medium exert on the refractive index, leading to a contribution in the phase mismatch between the fundamental and harmonic fields.

$$\Delta k_{\mathrm{fe}} = -\frac{\eta \cdot N_{atm} \cdot r_e \cdot \lambda_0 \cdot P \cdot (q^2 - 1)}{q \cdot P_0} \tag{3.4}$$

Impact of Laser Focusing (Δk_{foc}): The process of laser focusing also introduces a phase mismatch, a consequence of the spatial distribution of laser intensity across the medium.

$$\Delta k_{\mathrm{foc}} = -\frac{q}{Zr(1 + \left(\frac{Z}{Zr}\right)^2)} \tag{3.5}$$

Contribution from Dipole Phase (Δk_i): This component arises from the response of single atoms and depends on the trajectory of electrons within the continuum. The magnitude of this contribution varies depending on whether the electron trajectory is categorized as short or long.

$$\Delta k_{\mathrm{i}} = \frac{8Z \cdot \alpha \cdot I}{b^2 \cdot \left(1 + (\frac{2Z}{b})^2\right)^2} \tag{3.6}$$

It's important to note that the beam focusing gradient (Gouy phase) and dipole phase term are independent of the medium pressure and depend on the distance of the gas medium from the laser focus (denoted by Z). In contrast, the dispersion terms due to the neutral species (Δk_n) and the creation of free electrons (Δk_{fe}) depend on the

pressure of the system. This is because pressure determines the number of species (charged or neutral) per unit volume of the medium.

3.0.2 Code for estimating optimal phase matching parameters

A Python code was developed based on the theoretical framework outlined above to compute the Higher Harmonic Generation (HHG) yield using the formula provided in equation 3.1. Additionally, a separate code was created to estimate the Ammosov-Delone-Krainov (ADK) ionization rates [64] for the ionizing medium. These rates (η), combined with other macroscopic variables, were used to estimate the flux for the q^{th} harmonic. Next, the collected data was normalized, aiding in a qualitative understanding of the trends and relationships among various harmonics.

To identify the optimal phase-matching regime for a given laser intensity, a comprehensive scan was conducted across variations in pressure and the distance of the gas cell from focus (Z). Considering that the electrons responsible for generating XUV photons can tunnel throughout the entire duration of the fundamental pulse, an integration over all values of Intensity (from 0 to I_{peak}) was also done to calculate the total harmonic flux.

This process involved calculating all phase mismatch terms (Δk_n, Δk_{fe}, Δk_{foc}, and Δk_i) using the formulas provided in equations 3.3, 3.4, 3.5, and 3.6 for a given set of (P, Z, I). Subsequently, we determined the values of L_{med}, L_{abs}, and L_{coh} and substituted them into equation 3.1 to compute the q^{th} harmonic flux for this particular set of parameters. Integrating over the intensity range yielded the HHG flux for a specific (P, Z) pair.

Similarly, the integration over all pressure and Z values allowed us to generate

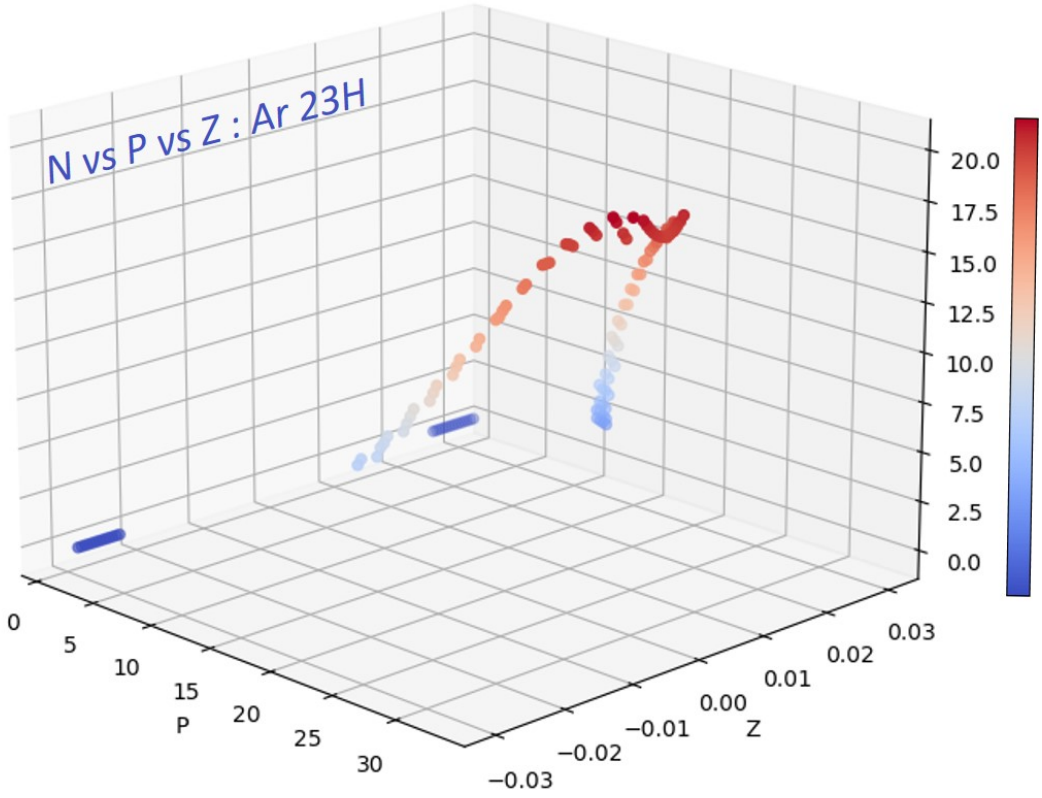

Figure 3.1: 23^{rd} harmonic flux vs. P vs. I in Argon at 0.73 mJ.

the graph shown in Fig3.1. This graph provides a comprehensive visualization of the relationship between HHG flux and different combinations of pressure and Z values, offering valuable insights into the optimal phase-matching conditions for our experimental setup.

Note that in the actual code implementation, the integration was limited to half of the pulse duration as the medium is fully ionized by the time, peak intensity is reached. Such highly ionized mediums do not produce efficient higher harmonic flux because of total phase mismatch.

3.0.3 Optimization of HHG using Two-color fields

Bichromatic driving fields were employed early in the development of high-order harmonic generation (HHG) as a means to overcome the inherent limitations of using a single-color field, i.e, low conversion efficiency and limited control over the return electron trajectories. By combining a fundamental frequency with one of its harmonics (typically 2ω or 3ω), these two-color fields break the inversion symmetry of the driving waveform, enabling sub-cycle control over the ionization and recombination process. This control allows for the selective enhancement of specific electron trajectories and the tuning of the harmonic yield. Despite their demonstrated potential, finding the perfect recipe for a fully optimized system by tweaking experimental parameters such as the pressure, intensity ratio, relative phase, dispersion, remains experimentally and theoretically challenging, and more importantly, scientifically intriguing to this day.

Since the present study aims to explore and understand the influence of two-color driving fields on HHG yield, it is important to acknowledge several seminal works in this area. On the theoretical front, Jin et al. [65] proposed that multicolor laser fields

could enhance HHG yield by up to two orders of magnitude. Their analysis showed that because macroscopic phase matching favors short trajectories, bichromatic fields can be tailored to preferentially increase ionization at times that lead to short return trajectories. This effectively boosts the yield by enhancing a subset of electron paths that are both efficient and phase-matchable.

This was experimentally tested in the work of Severt et al. [66] who systematically investigated the impact of the intensity ratio in bichromatic fields on HHG enhancement. Their experimental results demonstrated that by precisely controlling the relative phase and intensity ratio of a bichromatic ω-3ω field, it is possible to significantly alter the excursion time of short-trajectory electrons, thereby optimizing the harmonic yield. Furthermore, they demonstrated that by varying the relative intensity ratio between the two colors, one could shift the dominant enhancement mechanism between ionization rate and electron wave packet diffusion. Notably they reported a roughly one-order-of-magnitude enhancement using a 10:1 intensity ratio, which interestingly is the same ratio employed in our setup—albeit for ω-2ω fields rather than ω-3ω.

This work is particularly relevant to our study, as it complements our findings despite differences in field strength, configuration and propagation geometry. While Severt et al. employed a capillary-based setup with ω–3ω fields and a total pulse energy of 2mJ, our experiments are conducted in a comparatively thick gas cell using ω–2ω fields with a total pulse energy of 0.7mJ, yet we observe similar indications that the ionization timing within the bi-chromatic field plays a critical role in shaping the return kinetic energy and overall harmonic yield. This is especially evident in our pressure-optimized Argon HHG results (Fig. 3.8, 3.9), where the degree of ionization that best fits the measured harmonic spectra appears to be strongly correlated with the birth time of the electron in the laser cycle. This is evident from the observation that no

single ionization level provides a universally optimal fit across all harmonic orders. Instead, due to the strong modulation introduced by the second harmonic field, different harmonics are generated at distinct times within the cycle—each corresponding to a different effective electric field strength at the time of ionization. Put more intuitively, the extent to which the presence of the second harmonic field perturbs the electrons is dependent on their excursion times. Naturally, the phase-delay between the two color fields acts as a parameter to control each of these harmonics differently. We shall now discuss the experimental realization of such a setup.

3.0.4 Two-color extension of the HHG setup

The High harmonic generation setup can be modified and extended to incorporate the delay between the two-color input pulse. As discussed previously, this introduces an additional degree of freedom to control the HHG process by manipulating the input electric field, potentially leading to favorable harmonic characteristics.

Figure 3.2 (a) illustrates the experimental schematic for Two-Color HHG. The setup largely resembles the single-color setup, with the addition of four key optical components to the generation chamber [Figure 3.3], namely :

1. Half-Wave Plate (HWP): Ensures the fundamental beam's polarization aligns with the BBO crystal's axis for efficient second harmonic generation.

2. Second Harmonic Generation (SHG) BBO Crystal: Generates the second harmonic (400 nm) from the fundamental beam (800 nm) focused by the 750 mm focal lens within the chamber.

3. Dual Waveplate (DWP): Used to control the polarization of both beams independently (optional for specific experiments).

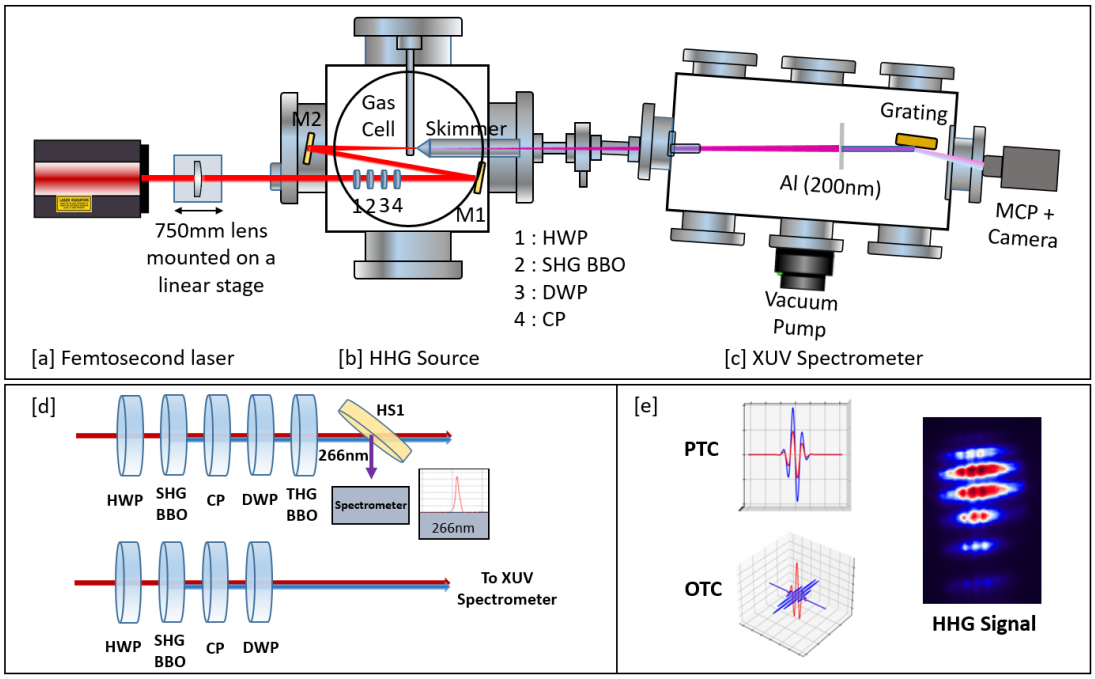

Figure 3.2: Schematic of the Two-Color HHG setup consisting of the laser[a], HHG source chamber[b] and XUV Spectrometer Chamber[c]. Scheme for generating delay between the two color pulses [d] with zero delay calibration done using Third Harmonic Generation (THG) [e] Graphical Representation of Orthogonal and Parallel polarization.

4. Compensation Plate (CP): Overlaps the two pulses temporally. It is typically made of a birefringent material like calcite.

Achieving perfect temporal overlap between the two pulses is crucial for efficient Two-Color HHG. Calcite, a birefringent material, is used to accomplish this. Birefringence refers to the variation in refractive index depending on the light's polarization and propagation direction within the crystal. This variation in refractive index allows for precise manipulation of the pulse propagation times. The calcite crystal possesses two distinct axes: the fast axis and the slow axis. By aligning the calcite crystal and directing the (otherwise faster) fundamental beam (800 nm) along the slow axis and the second harmonic beam (400 nm) along the fast axis, we can compensate for the inherent group velocity delay between the two pulses. Additionally, rotating the calcite plate allows for fine-tuning the delay by effectively increasing/decreasing the path length for each beam.

To confirm this overlap, a third harmonic generation (THG) BBO crystal is used. The calcite plate is rotated, and the position where the THG signal is maximized is considered the zero-delay point. Once achieved, the THG BBO crystal is removed, and the two pulses are focused onto the gas cell for HHG. The generated extreme ultraviolet (XUV) signal follows the same path inside the XUV spectrometer as in the single-color setup and is detected using an MCP-Phosphor detector. Figure 3.2(e) shows the HHG spectrum obtained for Argon using two-color pulses in parallel polarization configuration. Rotating the DWP axis with respect to the input beam enables us to switch the polarization configuration from parallel to orthogonal. The representations for both OTC and PTC have been shown in Fig.3.4 and Fig.3.5.

Following the production of HHG from Two-Color pulses, an optimization process was undertaken to determine the optimal conditions for HHG. It was anticipated based

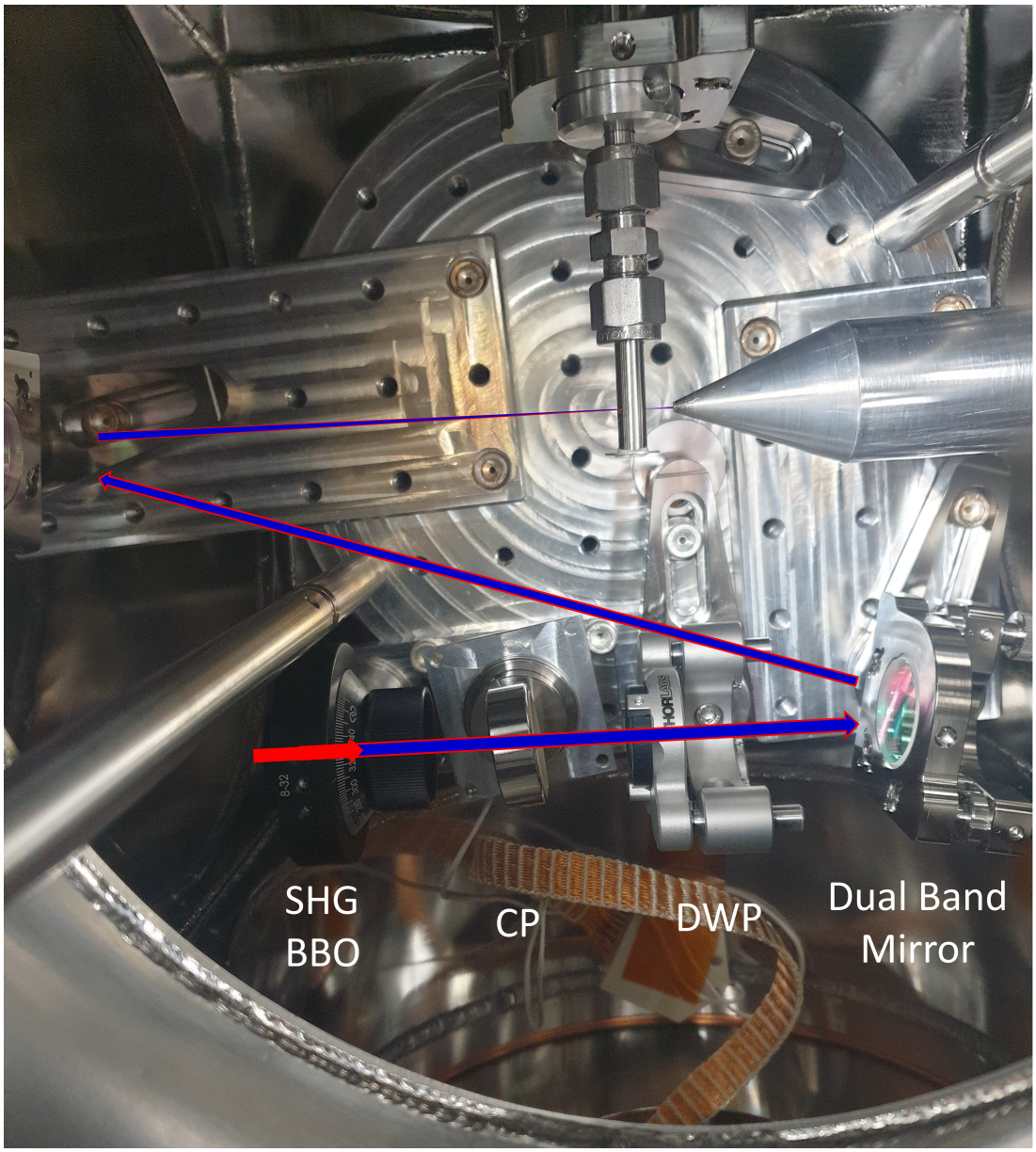

Figure 3.3: Generating chamber housing the Second harmonic generation BBO crystal (SHG BBO), Compensation plate (CP), Dual Waveplate (DWP) and Dual-band mirrors.

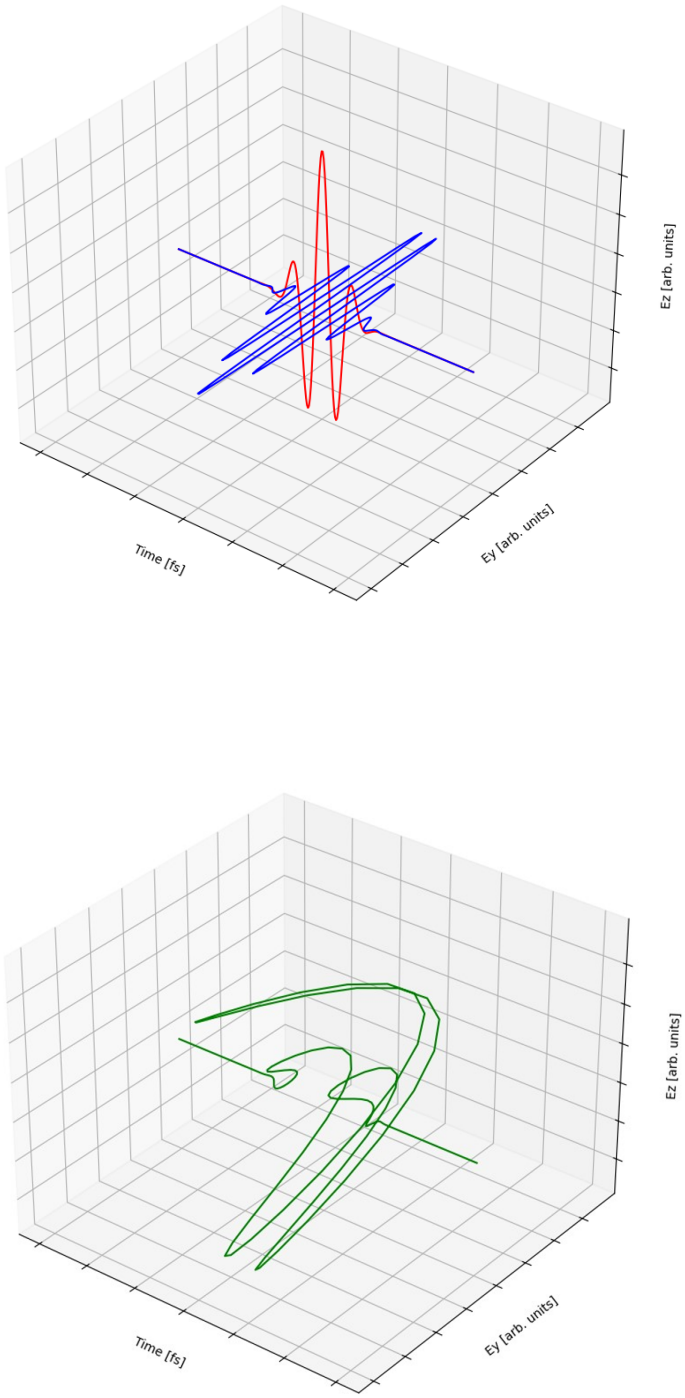

Figure 3.4: [Top] Fundamental(Red) and Second Harmonic(Blue) fields and the resultant OTC electric field [Bottom] at zero-delay position.

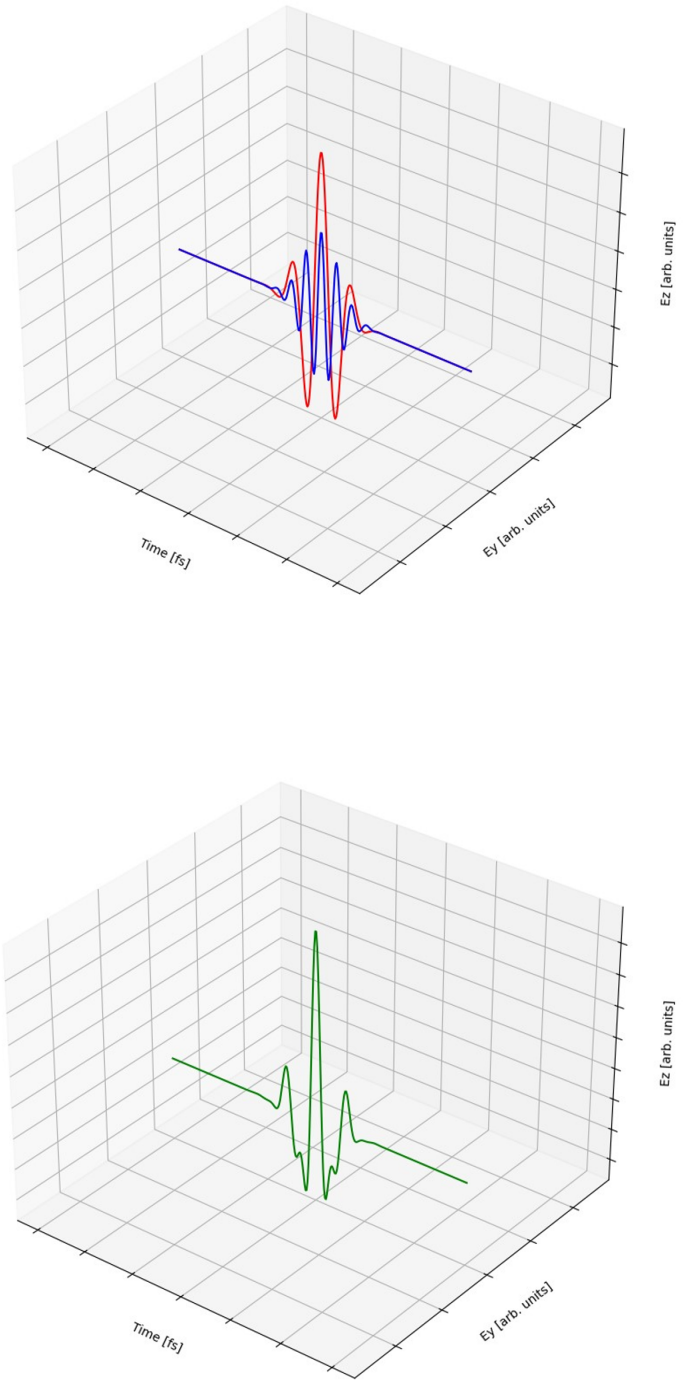

Figure 3.5: [Top] Fundamental(Red) and Second Harmonic(Blue) fields and the resultant PTC electric field [Bottom] at zero-delay position.

on previous discussions that the presence of an additional field would influence the optimal phase-matching parameters. We opted to use the single-color HHG yield derived from the earlier theoretical model as a benchmark for evaluating our two-color results. Interestingly, we observed a completely different behavior in the Z dependence in Argon. We repeated the experiment using Krypton and obtained similar results. Subsequently, we turned our attention to pressure variation, hoping for a significant change in the optimal range. To our surprise, the pressure dependence of HHG in Argon was in line with the predictions made by the 1D model, provided one accounted for the effect of two-color fields on the degree of ionization. Conversely, for CO_2, the pressure dependence of higher harmonics exhibited a different trend, deviating from the 1-D theoretical model. This deviation is possibly due to molecular properties and different phase-matching conditions for the two-color HHG in CO_2.

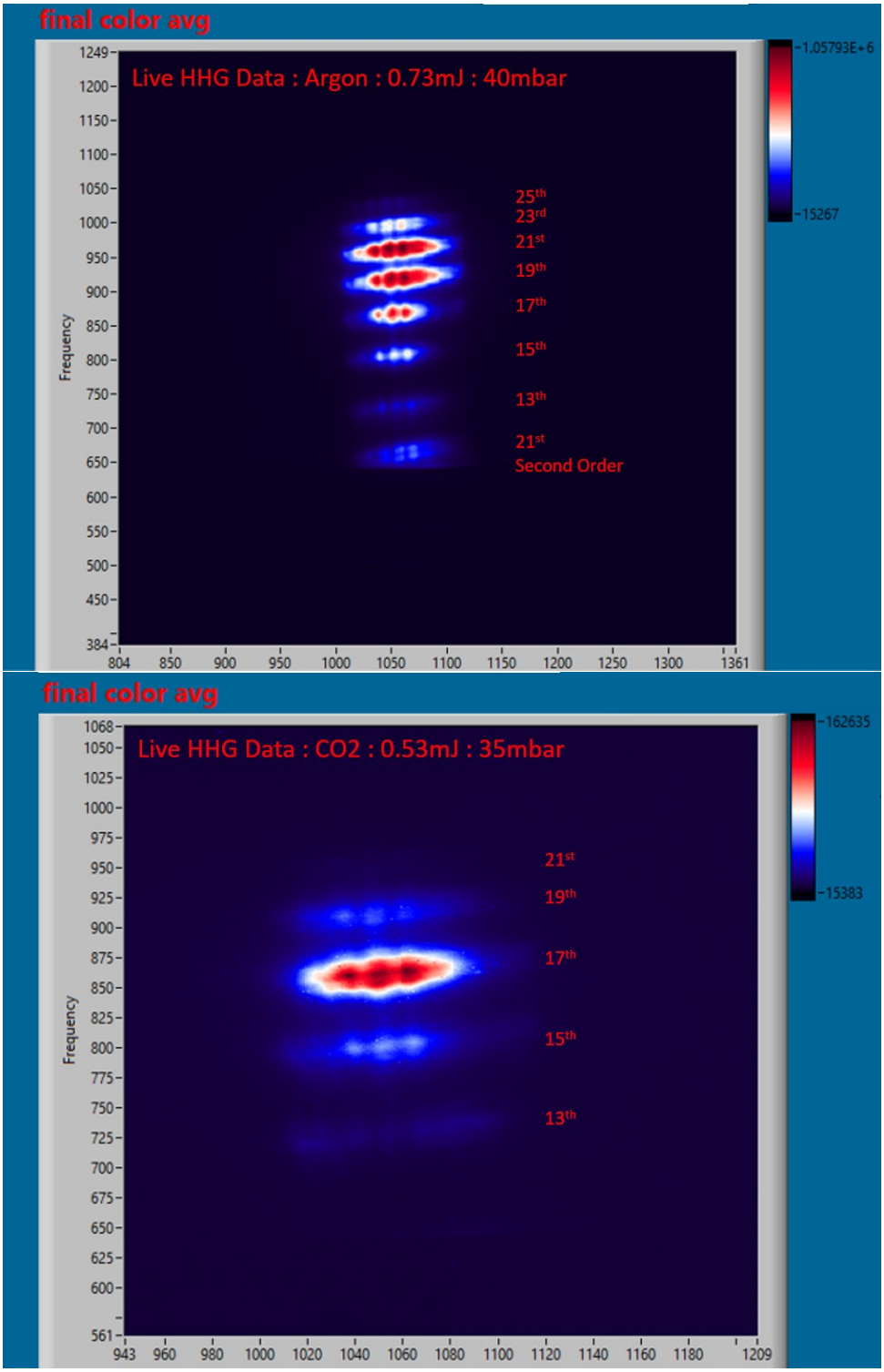

Figure 3.6: [top]HHG spectrum (raw image) of Argon observed at 0.73 mJ pulse energy and at 40 mbar pressure. [Bottom] HHG spectrum (raw image) of CO_2 recorded at 0.53 mJ pulse energy and at 35 mbar pressure.

3.0.5 Z- Dependence

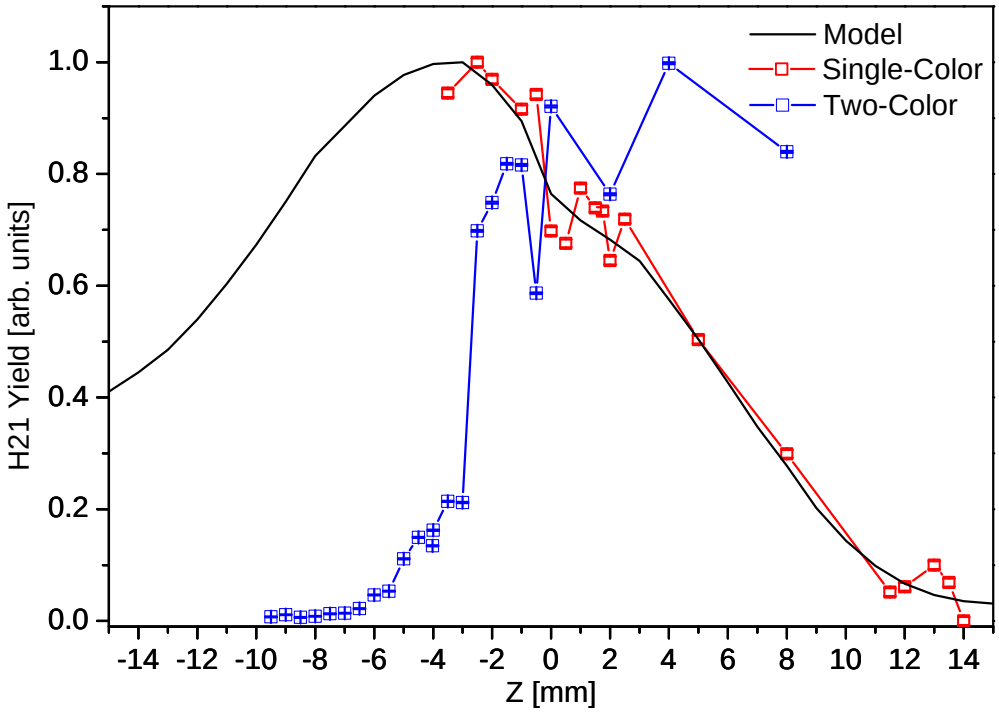

Figure 3.7: Z dependence using Single-Color vs Two-Color fields. Both studies are performed at 0.73W power and 38mbar gas (Ar) pressure.

As discussed in the previous section, in Two-Color High Harmonic Generation (HHG), the dependence of harmonic yield on the propagation distance from the focal point, known as Z-dependence, exhibits a different behavior compared to single-color HHG. This is shown in Fig 3.7 where the single-color HHG results are shown in red while the two-color results are shown in blue. We can see that the single-color results are in excellent agreement with the theoretical predictions (black). However, the two-color results are completely different. We claim this is because we can no longer neglect the dipole phase contribution in equation 3.2 as done previously, arguing that short-trajectory electrons do not acquire significant phase shifts during their journey. With

the contribution of long-trajectory tunneled electrons considered, we observe that for Z $<$ 0, achieving phase matching becomes challenging as there are three negative terms (Guoy phase, the dipole phase, and the free electron dispersion) that need to be balanced by only one positive term (neutral dispersion). This explains why, for Z$<$0, the HHG yield falls rapidly. Conversely, for Z $>$ 0, phase matching becomes more feasible as the dipole phase term now becomes positive, assisting the neutral dispersion term in balancing the remaining two terms in the phase matching equation, resulting in $\Delta K \rightarrow 0$. This phenomenon is evident in the observed behavior of the two-color results as we see efficient HHG generation for the positive Z axis.

3.0.6 Pressure Dependence

Following the investigation of Z-dependence, we turned our attention to another crucial parameter influencing phase matching: pressure. We optimized the two-color field by varying the pressure within the gas cell while maintaining a laser power of 0.73 mJ. This experiment successfully generated harmonics up to the 23^{rd} order in Argon. We expected a change in the optimal pressure in line with the significant deviations observed in the Z-scan compared to single-color HHG. However, for Argon, the experimental data (shown in Fig 3.8 and in Fig 3.9) for harmonics above the 17^{th} order exhibited a good fit with the predictions of the theoretical model. This can be explained using our existing understanding and arguments made in the previous section. The pressure-dependent terms in equation (3.2) are the natural and plasma dispersion terms respectively. We argued in the previous section that the change in Z-dependence was due to the role of the second harmonic field in unlocking the contribution due to the long trajectory electrons. This change is captured by the dipole phase term, which is independent of pressure. Therefore, the pressure dependence observed in single-color HHG remains largely unchanged.

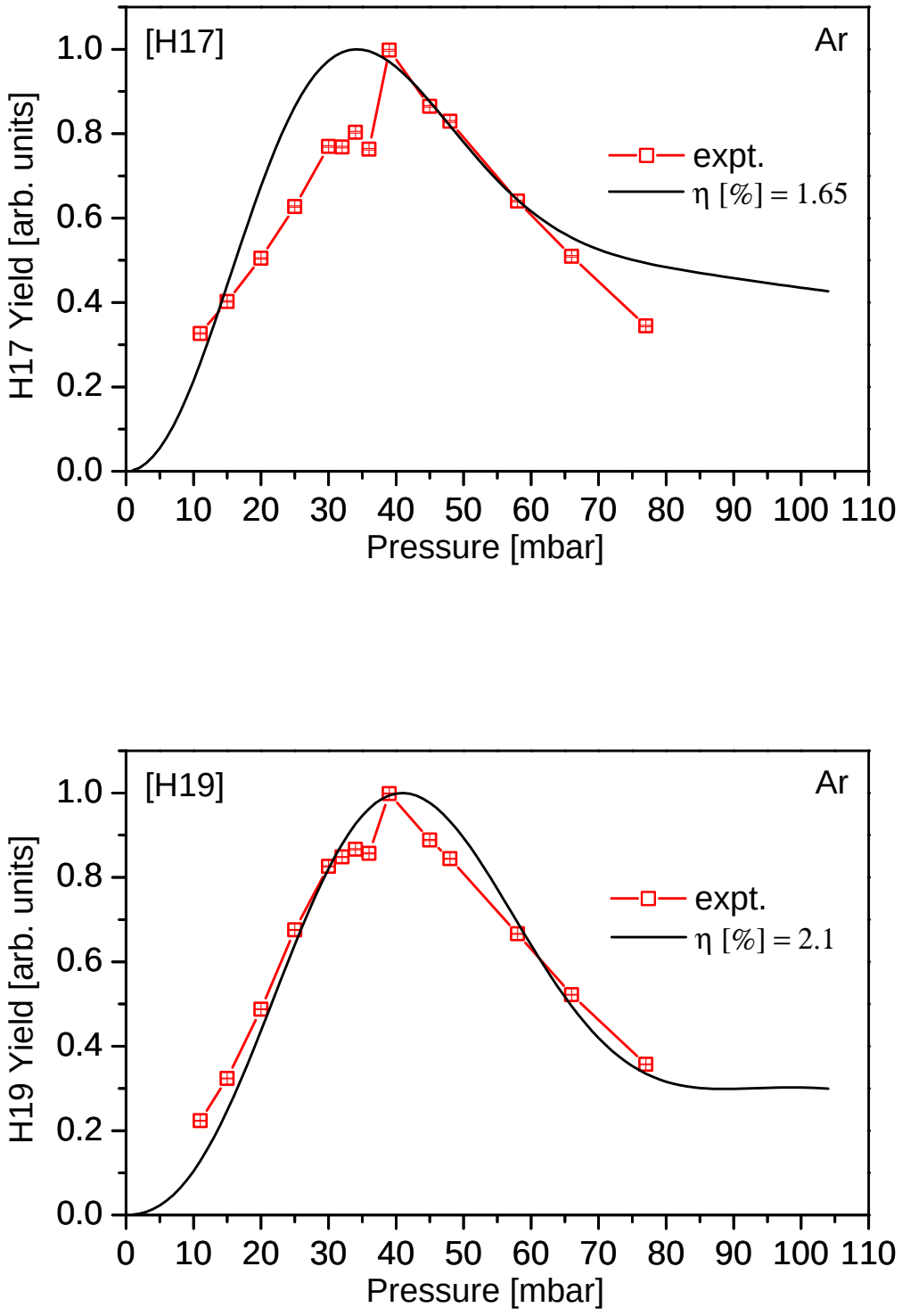

Figure 3.8: Two-Color Pressure dependence in 17^{th} and 19^{th} harmonic generated from HHG in Argon using 800 nm, 0.73 mJ, and 25 fs pulses.

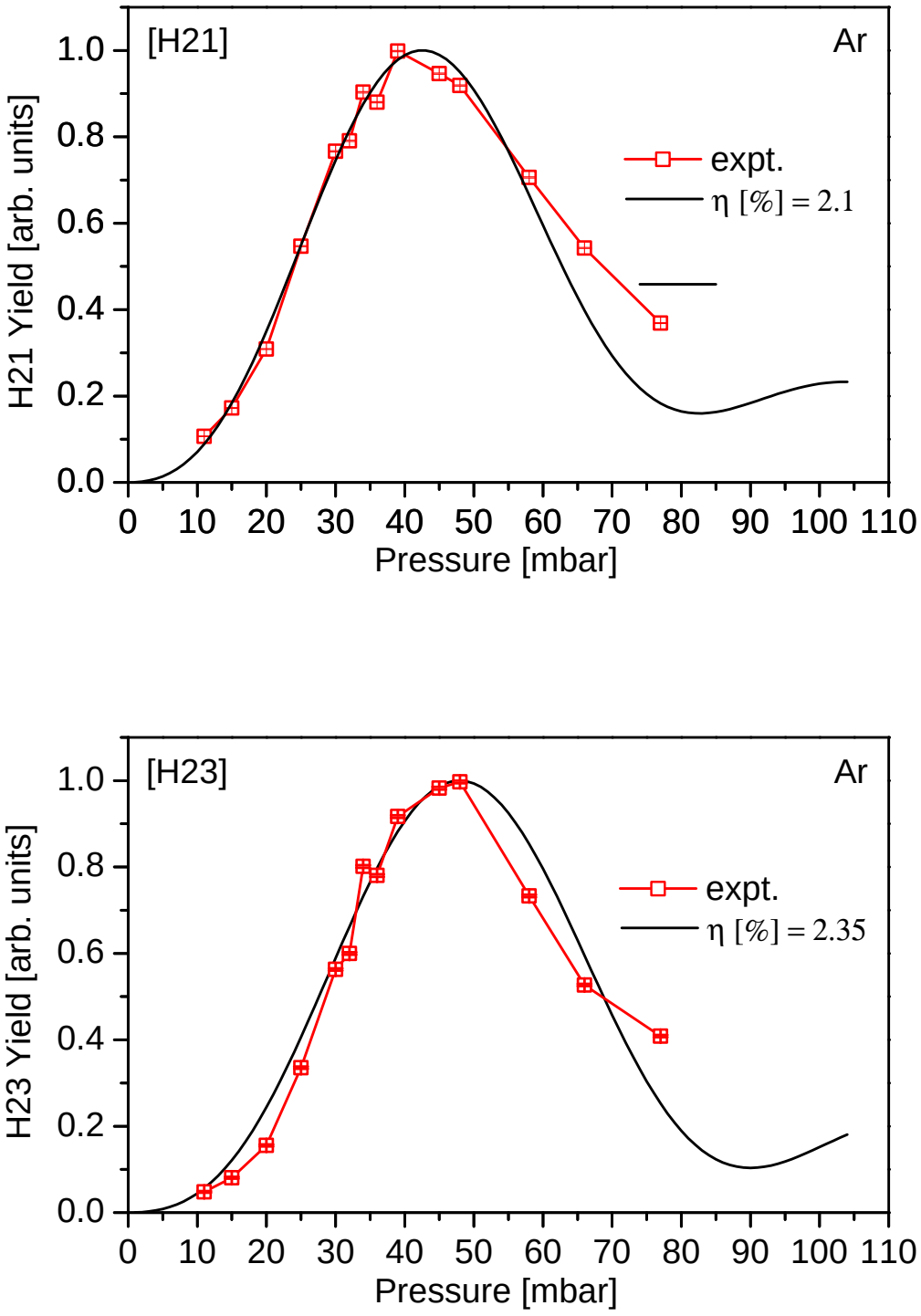

Figure 3.9: Two-Color Pressure dependence of 21^{st} and 23^{rd} harmonics generated from HHG in Argon using 800 nm, 0.73 mJ, and 25 fs pulses.

Pressure dependence in CO_2

The dependence of Two-color HHG in CO_2 yields an intriguing result, diverging significantly from our initial expectations. As discussed in the previous section, we anticipated the results to mirror those observed in Argon, given that the two phase-dependent terms (ΔK_n and ΔK_{fe}) remained unaffected by the presence of the second harmonic field. However, the experiment yielded a trend that is similar to Argon (increasing and then decreasing as a function of pressure) but deviates from the 1-D model.

Conducted with a laser power of 0.63 mJ, the experiment revealed pressure dependencies in CO_2 that deviated from the theoretical predictions of our 1-D model. Figure 3.10 and Figure 3.11 illustrate these deviations, highlighting a departure from the theoretical (1-D model) behavior(solid lines). Despite exhaustive efforts, we were unable to find the ionization probability (η) values for CO_2. Conventional calculations (such as using the MO-ADK theory) for finding such probabilities provide inaccurate results due to the complex geometrical structure of the molecule. To address this limitation, we plotted CO_2 curves for various η values. The black curve represents our best fit, while the blue and green curves denote the minimum and maximum degrees of ionization, respectively, expected with the laser intensity.

However, upon examining these 1-D model curves, none could adequately explain the observed pressure-dependent behavior of CO_2. This discrepancy underscores the complexity of the HHG process in CO_2 and suggests the presence of additional factors influencing the observed results. Since the two-color effects on the tunneled electron are (assumed) independent of the system's potential, our best estimate is that the presence of two-color fields significantly alters the ionization rate for CO. Further theoretical investigation is warranted to elucidate these phenomena comprehensively par-

ticularly those which take the molecular structure into account[67]. A more detailed discussion has been carried out in section 5.0.2.

3.0.7 Absence of even-order harmonics

A characteristic feature of higher harmonic generation using two-color pulses is the emergence of even harmonics [68–70]. This phenomenon arises due to the asymmetric nature of the net electric field in the two-color case, which breaks the symmetry of the system responsible for generating only odd-order harmonics. However, in our experiment with a 0.73 mJ laser power and a 10% efficient BBO crystal, we did not observe even harmonics. We argue that the laser power of the second harmonic pulse is not sufficient to generate even harmonics. [1] This raises a reasonable question: how can we be certain the observed spectrum originates from Two-Color HHG and not solely from single-color HHG?

One key observation in favor of two-color HHG (other than the huge deviations observed in Z-dependence of Argon) is the significantly higher HHG flux (order of magnitude) compared to the single-color case. This behavior is characteristic of Two-Color HHG [66, 71–73]. However, we will conclusively address this point in subsequent chapters, where we demonstrate that despite the absence of even harmonics, the second laser pulse can significantly affect the tunneled electron trajectories, as evidenced by the HHG yield dependence on the relative phase between the two (FW and SH) pulses.

[1] A graph showing the production of both even and odd harmonics could later be produced when sufficient power was available, and has been added to the final section (Addendum) of this thesis.

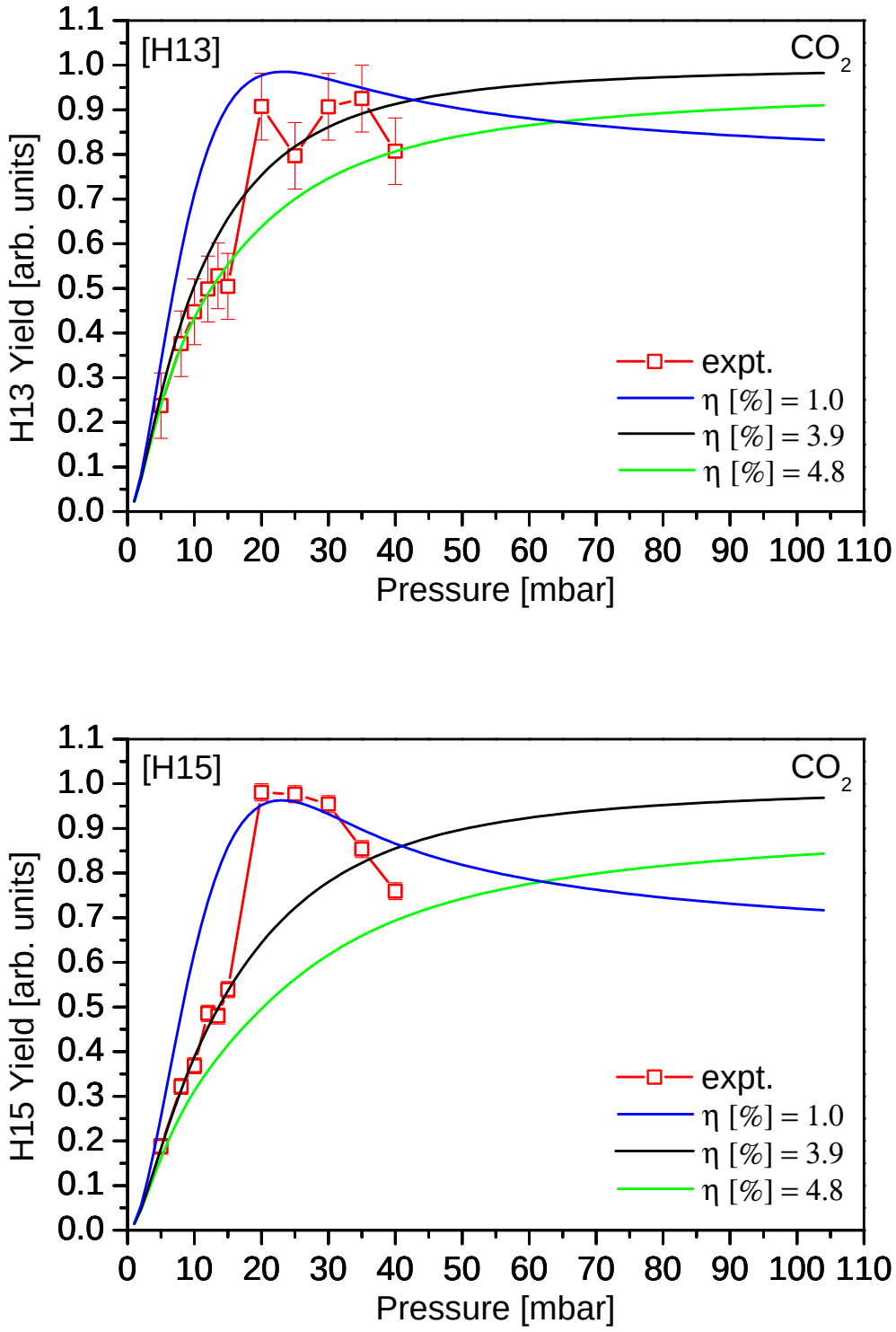

Figure 3.10: Two-Color Pressure dependence of 13^{th} and 15^{th} harmonics generated from HHG in Argon using 800 nm, 0.73 mJ, and 25 fs pulses.

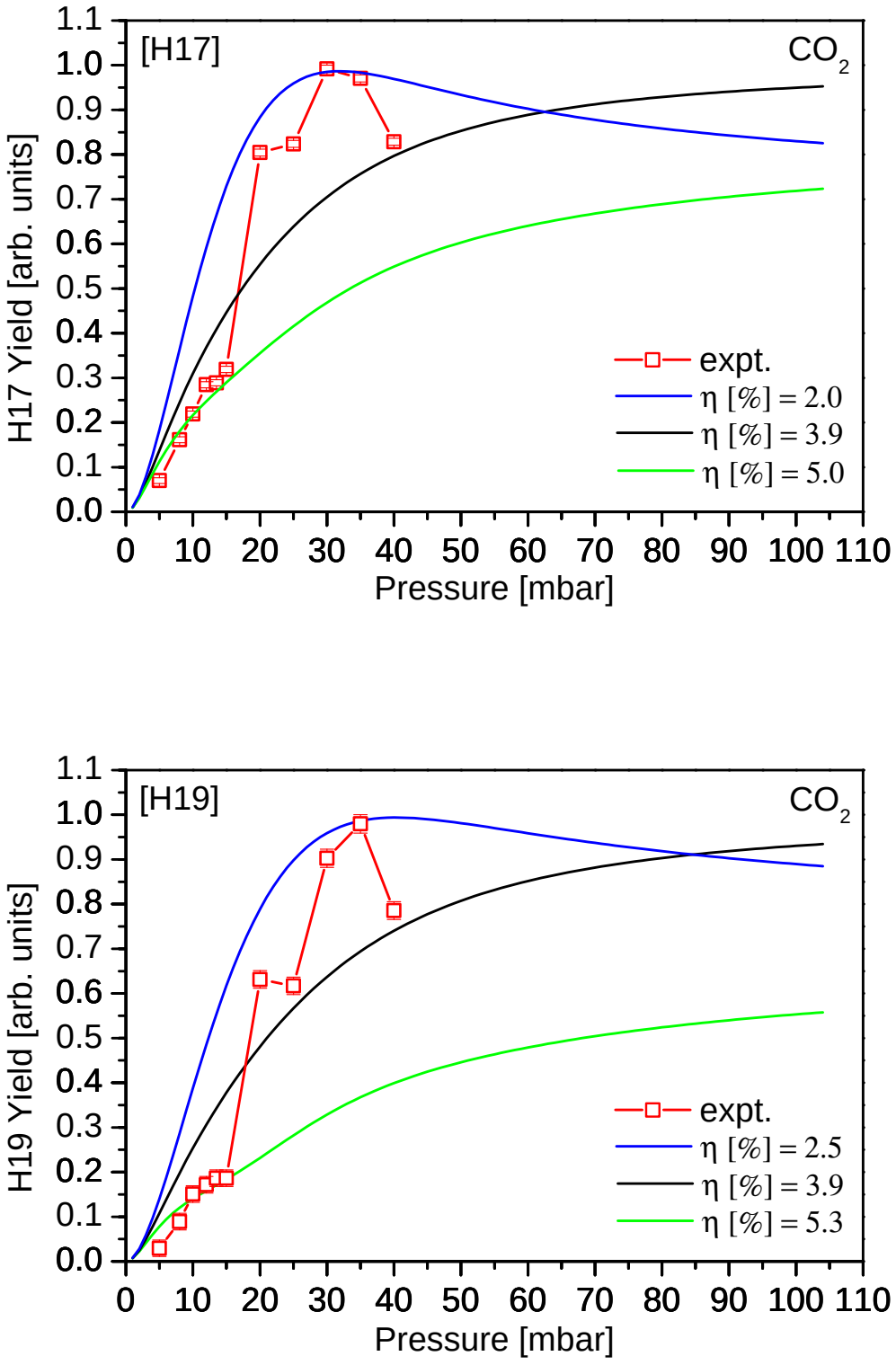

Figure 3.11: Two-Color Pressure dependence of 17^{th} and 19^{th} harmonics generated from HHG in Argon using 800 nm, 0.73 mJ, and 25 fs pulses.

3.0.8 Summary and Conclusions

This chapter provides a comprehensive overview of the design and development of a Two-Color High Harmonic Generation (HHG) setup, detailing key optical components and experimental procedures for generating HHG using two-color fields. We begin by laying a theoretical foundation for comparing our results by utilizing the 1D model by E.Constant [2] that captures the key components of the phase matching equation and estimates the HHG yield.

We discuss the necessary modifications to adapt the existing HHG setup for use with Two-Color fields, including the determination of the zero-delay position for the two-color pulses. We demonstrate the operation of the HHG setup using two-color pulses in both the OTC and PTC polarization orientation and present the obtained HHG spectra of Argon as the generating medium.

Following this, we optimize the setup by varying the pressure and the distance of the gas cell from the focus (Z). While the pressure dependence of HHG in Argon aligns well with the predictions of the theoretical model by E. Constant, significant deviations are observed in the Z-dependence. We attribute these deviations in results to the contribution from individual phase mismatch terms, particularly the dipole phase mismatch arising from long-trajectory tunneled electrons. Notably, the neutral and free electron dispersion terms remain unaffected, exhibiting behavior similar to that of the single-color HHG case. This explains why the pressure-dependent results remain the same while the Z-dependence for HHG experiences notable changes.

Expanding our experimental study, we explore HHG from the CO_2 molecule, where marked deviations are observed, even in the pressure dependence of HHG. This discrepancy is attributed to the complex geometrical nature of the molecule, warrant-

ing further investigation using better theoretical models.

Chapter 4

Two-Color HHG in Atoms

Higher Harmonic Generation from atoms (Ar, Kr, Xe) induced by two-color laser fields are discussed in this chapter. The two different polarization schemes, viz, orthogonal and parallel, are employed for measuring the HHG spectra from the atoms. The HHG yield as a function of two-color intensity is investigated, and it was found that the Harmonic yield increases with two-color intensity. The two-color polarization also affects the HHG yield, and comparative results have been presented. Finally, we studied the two-color phase dependence on the HHG yield and observed that the two-color phase influences the tunnel electron trajectories and thus affects the HHG yield. We interpreted our experimental findings based on results obtained using an in-house developed theoretical simulation code in which the yield and kinetic energy of return electron trajectories were estimated at experimental parameters. Detailed discussions of these studies are provided in the subsequent sections.

4.1 The role of Two-Color fields

In the preceding chapter, we examined how the phase-matching conditions differed between the two-color and single-color cases. This section delves deeper into the role of the two-color laser field on the return tunnel electron trajectories, which affects the harmonic yield. We previously demonstrated that these trajectories significantly influence the accumulated dipole phase in atoms and that the subsequent changes in results (Z-dependence) could be explained using the same theoretical model for single color field [2, 51] by incorporating the contribution of long-trajectory electrons.

Now, we introduce a relative delay between the two color pulses as an additional degree of freedom to further explore (and potentially control) the behavior of these returning electrons. This section will investigate how varying the intensity and relative phase of the two colors affects the net electric field experienced by the atom and the tunneled electron. As the net electric field dictates the acceleration and, hence, the trajectories of the recoiling electrons, understanding this influence is crucial for understanding the subsequent impact on the HHG process.

We begin by looking at the impact of increasing the two-color field strength while maintaining a constant intensity ratio (1:10). Subsequently, we will introduce a controlled phase delay between the two colors and study how the second harmonic field interacts with the returning electrons. This analysis will offer valuable insights into potentially enhancing the generation of specific harmonic orders at specific delays.

Simulation for return electron trajectories

As discussed in Corkum's three-step model [1], a strong laser field can suppress the coulomb barrier facilitating the tunneling of an electron. This tunneled electron is

assumed to be free of the influence of the parent ion and is solely governed by the laser field. Therefore, the entire treatment is semi-classical in nature. As a result, we may compute the electron trajectories using Newton's equation of motion:

$$m_e \frac{d^2y}{dt^2} = -eE_{field} \tag{4.1}$$

where m_e and e are the mass and charge of electron, E_{field} is the electric field of the laser. By establishing a suitable set of initial conditions for the electron, we can determine its position and energy as a function of time. In our calculations, we will assume that at the birth time, immediately after the electron tunnels out and becomes free from the influence of the parent atom, the electron possesses no kinetic energy and is at rest. We will now choose a suitable mathematical representation for the femtosecond pulse, plug it back into equation [4.1], and solve for y. There are many viable mathematical functions that capture the envelope and carrier oscillations of an ultrashort pulse however we shall use the following representation:

$$A \cdot \cos\left(\omega(t+\phi)+\phi_1\right) \cdot \sin^2 \frac{\omega(t+\phi)}{\eta} \tag{4.2}$$

where A is the electric field amplitude, ω is the angular frequency of laser, ϕ is the relative phase which determines the field strength at t = 0, ϕ_1 represents the carrier envelop phase (CEP) and η represent a constant governed by the pulse duration.

For two-color fields, two different orientations can be discussed.

Solving for y in equation [4.1] yields :

$$y = \frac{e}{m}(I_1 + I_2) + c_1 t + c2 \tag{4.3}$$

where,

$$\begin{aligned} I_1 = \frac{A_1}{2}\Bigg(&\frac{1}{w^2}\frac{n^2}{(4+2n)(n+2)}\cos\left(\left(1+\frac{2}{n}\right)wt+\phi_1\right) \\ &-\frac{1}{w_1^2}\cos(w_1 t+\phi_1)+\frac{1}{w^2}\frac{n^2}{(2n-4)(n-2)}\cos\left(\left(1-\frac{2}{n}\right)wt+\phi_1\right)\Bigg) \end{aligned} \tag{4.4}$$

$$\begin{aligned} I_2 = \frac{A_2}{2}\Bigg(&\frac{1}{w^2}\frac{n^2}{(4+2n)(n+2)}\cos\left(\left(1+\frac{2}{n}\right)w(t+\phi)+\phi_1\right) \\ &-\frac{1}{w_2^2}\cos(w_2(t+\phi)+\phi_1)+\frac{1}{w^2}\frac{n^2}{(2n-4)(n-2)}\cos\left(\left(1-\frac{2}{n}\right)w(t+\phi)+\phi_1\right)\Bigg) \end{aligned} \tag{4.5}$$

$$\begin{aligned} c_1 = &-\left(\frac{eA_1}{2m_e}\right)\left(\frac{1}{w_1}\sin(w_1 T+\phi_1)-\frac{n}{4+2n}\cdot\frac{1}{w}\sin\left(\left(1+\frac{2}{n}\right)wT+\phi_1\right)\right. \\ &\left.-\frac{n}{2n-4}\cdot\frac{1}{w}\sin\left(\left(1-\frac{2}{n}\right)wT+\phi_1\right)\right) \\ &-\left(\frac{eA_2}{2m_e}\right)\left(\frac{1}{w_2}\sin(w_2(T+\phi)+\phi_1)-\frac{n}{4+2n}\cdot\frac{1}{w}\sin\left(\left(1+\frac{2}{n}\right)w(T+\phi)+\phi_1\right)\right. \\ &\left.-\frac{n}{2n-4}\cdot\frac{1}{w}\sin\left(\left(1-\frac{2}{n}\right)w(T+\phi)+\phi_1\right)\right) \end{aligned} \tag{4.6}$$

$$
\begin{aligned}
c_2 = &- \frac{eA_2}{2m_e}\left(\frac{n^2}{(4+2n)(n+2)}\cdot\frac{1}{w^2}\cos\left(\left(1+\frac{2}{n}\right)w(T+\phi)+\phi_1\right)\right.\\
&\left.-\frac{1}{w_2^2}\cos(w_2(T+\phi)+\phi_1)+\frac{n^2}{(2n-4)(n-2)}\cdot\frac{1}{w^2}\cos\left(\left(1-\frac{2}{n}\right)w(T+\phi)+\phi_1\right)\right)\\
&- \frac{eA_1}{2m_e}\left(\frac{n^2}{(4+2n)(n+2)}\cdot\frac{1}{w^2}\cos\left(\left(1+\frac{2}{n}\right)wT+\phi_1\right)\right.\\
&\left.-\frac{1}{w_1^2}\cos(w_1(T)+\phi_1)+\frac{n^2}{(2n-4)(n-2)}\cdot\frac{1}{w^2}\cos\left(\left(1-\frac{2}{n}\right)wT+\phi_1\right)\right)-c_1T
\end{aligned}
\tag{4.7}
$$

The equation 4.3 gives us a way to estimate the path and more importantly, the return kinetic energy of the electron. Before moving onto the experimental realization of the two-color scheme it is important to highlight the viability of the semi-classical treatment and the extent to which it can be applied, especially at the single-atom level. The quantum mechanical treatment of this problem via the Strong Field Approximation (SFA) referred to as the Lewenstein's model [16] shows that the ionization rate and electron wave packet dispersion while traversing the continuum, strongly influence the harmonic yield. Notably, it can be shown that the classical electron trajectories are approximately equivalent to the trajectories predicted using SFA within the saddle-point approximation. This is because the Lewenstein model (SFA) expresses the HHG dipole response as a time integral over all possible ionization and recombination times and momenta but most of the contribution to the integral comes from (the saddle) points where the phase of the integrand changes slowly. To find these points, we look for points where the derivatives of the classical action are zero — meaning the action is stationary.

$$
S(t,t',p)=\int_t^{t'}\left[\frac{1}{2}(p+A(\tau))^2+I_p\right]d\tau \tag{4.8}
$$

where, t$'$: ionization time, t: recombination time, p: canonical momentum of the electron in the continuum, $A(\tau)$: vector potential of the laser field and I_p : ionization potential of the atom/molecule. To find the stationary phase points (saddle points), we take derivatives of $S(t,t',p)$ with respect to p, t and t$'$ and set them to 0 i.e

$$\begin{aligned} \frac{\partial S}{\partial p} = \int_t^{t'} [p + A(\tau)] d\tau = 0 \\ \frac{\partial S}{\partial t'} = 0 \\ \frac{\partial S}{\partial t} = 0 \end{aligned} \tag{4.9}$$

These conditions tell us: when the electron leaves the atom (ionization time), with what momentum it travels and when it returns (recombination time). These equations are therefore like Newton's equations, but with complex variables, and derived quantum mechanically. Thus we already see a classical equivalence emerge out of this treatment. In the classical limit, these equations yield exactly the three-step model trajectories: real-valued ionization, propagation, and recombination times under a laser field. Thus our earlier treatment of using classical trajectories to estimate the path of the electron holds up well and can indeed be used to study [66] the emerging harmonics using the two-color fields.

4.2 Experimental Scheme for Two-Color delay-dependent experiments

This section describes the experimental setup for studying the effect of relative phase delay between the two colors in a High Harmonic Generation (HHG) experiment. The core setup remains identical to the standard two-color HHG setup; however, the data acquisition scheme is modified to introduce and record the two-color phase

delay dependence of the HHG spectra.

A motorized rotation stage (Attocube-3030) equipped with a calcite compensation plate allows for precise control of the relative phase delay between the two color pulses. A custom LabVIEW program interfaces the rotation stage with the PCO-edge camera, which captures the HHG signal observed on the MCP-Phosphor detector. The program operates by first recording the HHG spectra at a specific phase delay position. It then instructs the stage to move to a new position based on a user-defined step size. This step size is carefully chosen to ensure that 10 points can be obtained within 1 cycle of the second harmonic pulse, which translates to 133 as.

Due to the rotation stage's ability to be precisely adjusted in micro degrees, a correlation needs to be established between the degree of rotation and the delay between the pulses. To achieve this, existing data from the Two-Color Velocity Map Imaging (VMI) experiments were utilized [17]. This involved comparing photoionization results obtained using the compensation plate with those acquired using the nanometer stage. Since the results from the nanometer stage can be directly converted to attoseconds (1 nm = 3.33 as), this comparative analysis ensured the accurate characterization of the compensation plate.

It's worth noting that the nanometer stage couldn't be used due to its requirement for a non-collinear arrangement of generating the two-color pulses. In this configuration, half the power in one of the interferometer arms (responsible for SHG) is lost after recombination. Given the limited laser power available during the experiment, such loss couldn't be afforded.

Once the stage reaches the new position, the camera triggers another data acquisition sequence. This process is repeated for multiple phase delay positions. The data

acquisition time at each position is set to 100 seconds to ensure a satisfactory signal-to-noise ratio.

4.3 Results and Discussions

In this section, two-color laser intensity, polarization, and relative phase-induced effect on the HHG yield from atoms are discussed in detail. These parameters are directly linked with the two-color field, which will affect the tunnel electron return trajectories and kinetic energy. Due to the asymmetric nature of the two-color field, the effect on tunnel electron return trajectories directly alters the yield of HHG. Thus, it would be interesting to see how the manipulation of the two-color field affects the HHG yield.

4.3.1 Two-Color Intensity dependence in Argon

Two-color HHG in Argon exhibits an interesting relationship with the intensity of the driving laser pulses. The two-color HHG yield of Argon as a function of input power is shown in Figure 4.1. This HHG yield is obtained at fixed experimental parameters. It is interesting to see the effect of two-color laser intensity (input power) on the HHG yield trend. The results show distinct two-color intensity-induced trends for lower and higher-order harmonics of Argon.

Lower-order harmonics (below the 19th harmonic) show a flat response to increasing intensity. This implies that the yield for these harmonics remains relatively constant despite increasing the laser power. Higher-order harmonics (above the 19th harmonic) exhibit a linear increase in yield with intensity. The 25th harmonic, for instance, demonstrates a clear linear relationship between its yield and the two-color intensity. This behavior can be explained by considering two intensity limits that in-

fluence harmonic generation:

Lower intensity limit (I_{mic}): Also known as the cutoff intensity (2.7), this limit depends on the ionization energy required to generate a specific harmonic order. Consequently, lower-order harmonics require lower intensity.

Upper-intensity limit (I_{mac}): This limit is related to the optimal phase-matching conditions for HHG. Excessive ionization beyond this limit due to increasing intensity disrupts these optimal conditions, hindering the generation efficiency.

The observed flat response for lower harmonics suggests that the intensity at 0.73 mJ (laser pulse energy) is already sufficient to saturate these levels. Further increases in intensity have minimal impact on their yield. In contrast, higher harmonics have a higher saturation intensity, requiring a stronger driving field strength to exhibit this flat behavior.

4.3.2 Two-Color Intensity dependence in Xe and Kr

Similar to the study in Ar, we performed Two-Color intensity-dependent investigations in Xe (results shown in Figure 4.2) and Kr (Figure 4.3). The experiments in Xe spanned power levels from 0.15 W to 0.5 6W at 6.2 mbar pressure, while in Kr, power levels ranged from 0.50 W to 0.69 W at 25 mbar pressure. An interesting observation was made when analyzing the total power for Xenon, as depicted in Fig. 4.2. Initially, a linear increase in power was noted at lower intensities, followed by a sharp escalation beyond 0.4 W. We probed further into this trend by examining the behavior of individual harmonics as shown in Figure 4.4. The 13^{th} harmonic exhibited a linear trend initially, saturating around 0.5 W power, similar to our findings in Argon. However, for higher harmonics such as the 17th and 19th, an exponential increase in HHG yield

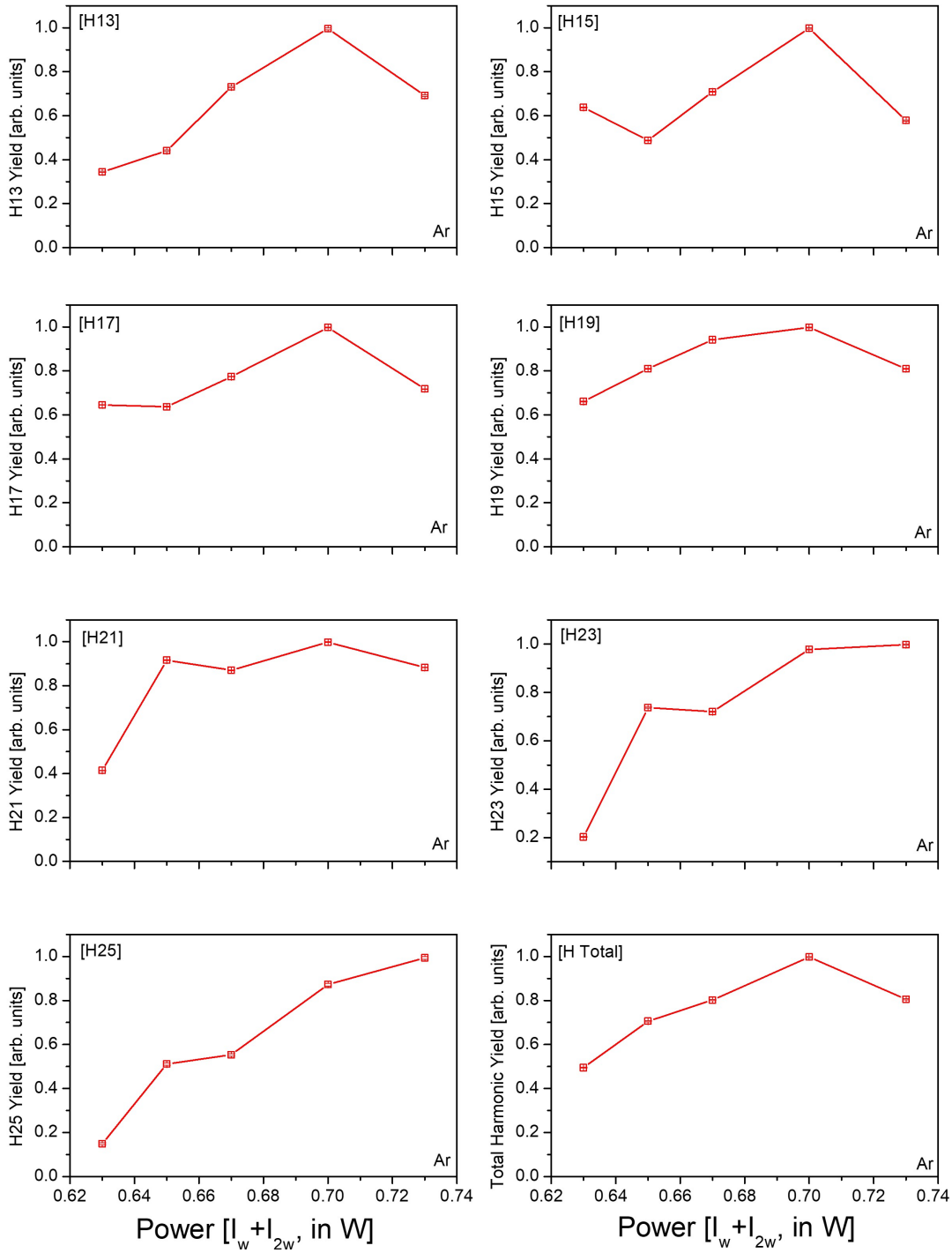

Figure 4.1: Two-color HHG of Ar as a function of input power.

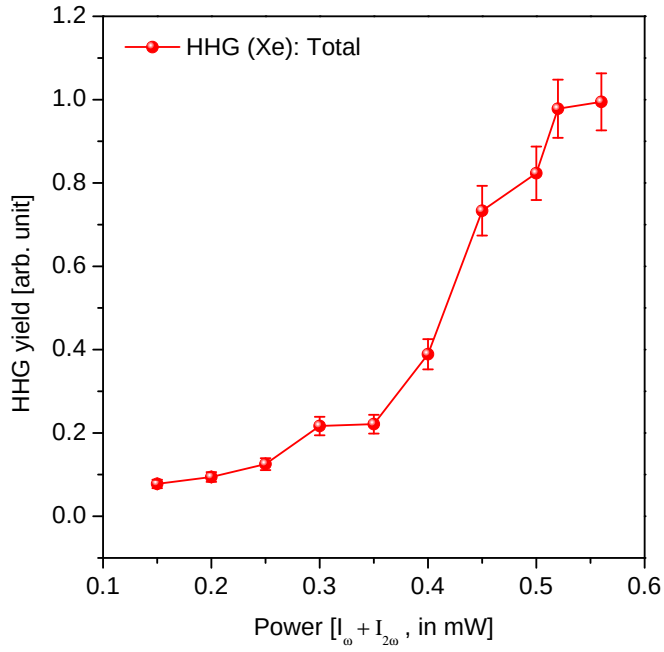

Figure 4.2: Two-color HHG of Xe as a function of input power.

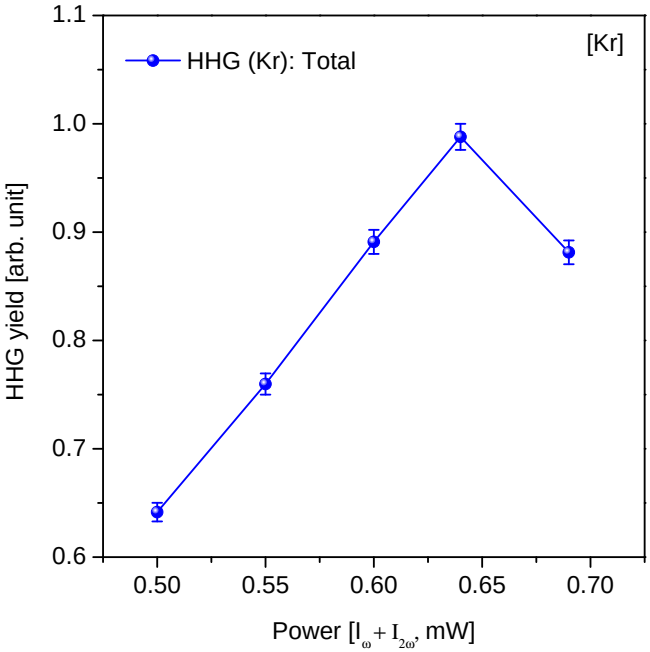

Figure 4.3: Two-color HHG of Kr as a function of input power.

was observed beyond their respective cutoffs at 0.35 W and 0.40 W. We used the laser parameters to convert the laser power to peak intensity and found that for H17 it stood at $6.7 \times 10^{13} W/cm^2$ and for H19 it was $7.66 \times 10^{13} W/cm^2$. Upon comparison with the theoretical values estimated using the cut-off intensity formula outlined in Figure 2.7, interesting observations were made. The theoretical estimates were calculated and found to be $7.49 \times 10^{13} W/cm^2$ and $9.12 \times 10^{13} W/cm^2$ for H17 and H19, respectively, indicating a deviation from the experimental results.

This discrepancy can be attributed to the two-color HHG process. The interference of the two-color pulses effectively leads to a higher "perceived" intensity due to a higher net electric field at certain phase positions of the two pulses. This allows for the generation of higher harmonics even at lower total power levels. In essence, the combined effect of the two colors unlocks higher intensities, enabling the production of H17 and H19 at lower total power compared to what would be required in a single-color setup.

4.3.3 Two-color HHG of atoms: OTC vs PTC

Having examined the two-color intensity dependence of HHG, we now explore how different polarization configurations in two-color fields influence the process. Fig.4.5 shows the projection of HHG spectra acquired using both Parallel Two Coloured (PTC) and Orthogonal Two Coloured (OTC) fields at zero delay position, obtained in Argon at a laser power of 0.73 W and 30 mbar pressure. The figure clearly shows a significant impact of polarization. The yield of higher harmonics is markedly higher in the PTC case compared to the OTC case. This observation aligns with our expectations, as the combined electric field strength is greater in the PTC configuration where both colors are polarized along the same axis. In contrast, the OTC configuration results in a net

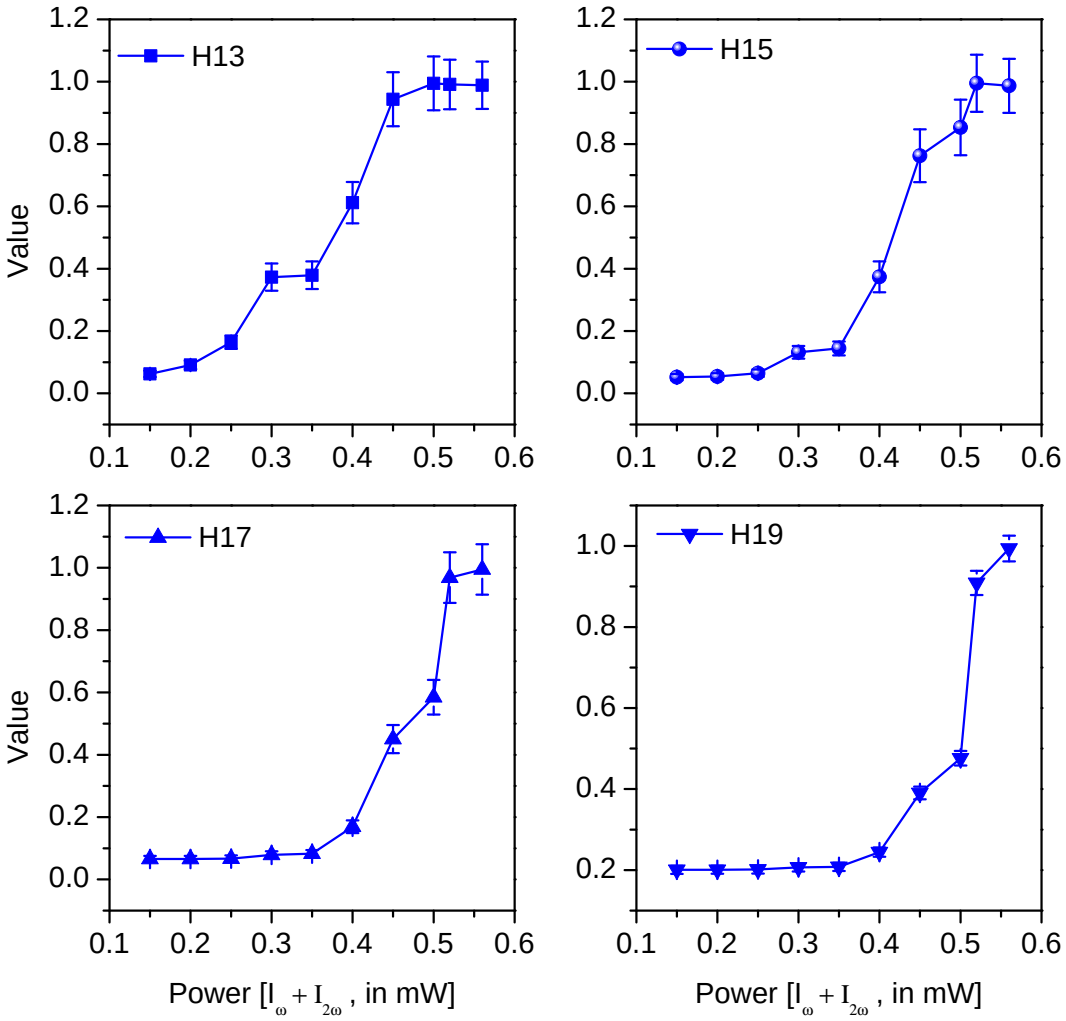

Figure 4.4: Two-color HHG of Xe as a function of input power.

electric field that is not confined to a single plane, making recombination between the electron and the ion less probable. Interestingly, the 15th and 17th harmonics appear to be not sensitive to this polarization effect, exhibiting similar yields in both PTC and OTC configurations.

We propose that the electrons responsible for generating these lower harmonics are tunneled out when the field strength is weak, particularly at the onset of the fundamental pulse. Consequently, the Second Harmonic (SH) pulse, being only 10% of the fundamental, is even weaker. This scenario, therefore, resembles the single-color case, explaining why we observe no sensitivity to the relative polarization. However, this does not explain why the 13th harmonic exhibits a higher yield [Note that the harmonic at pixel 670 is formed due to the second order diffraction of the 21^{st} harmonic and therefore mimics the yield variation]. Further investigations are needed to fully understand the reason behind this unique behavior of the 15th and 17th harmonics.

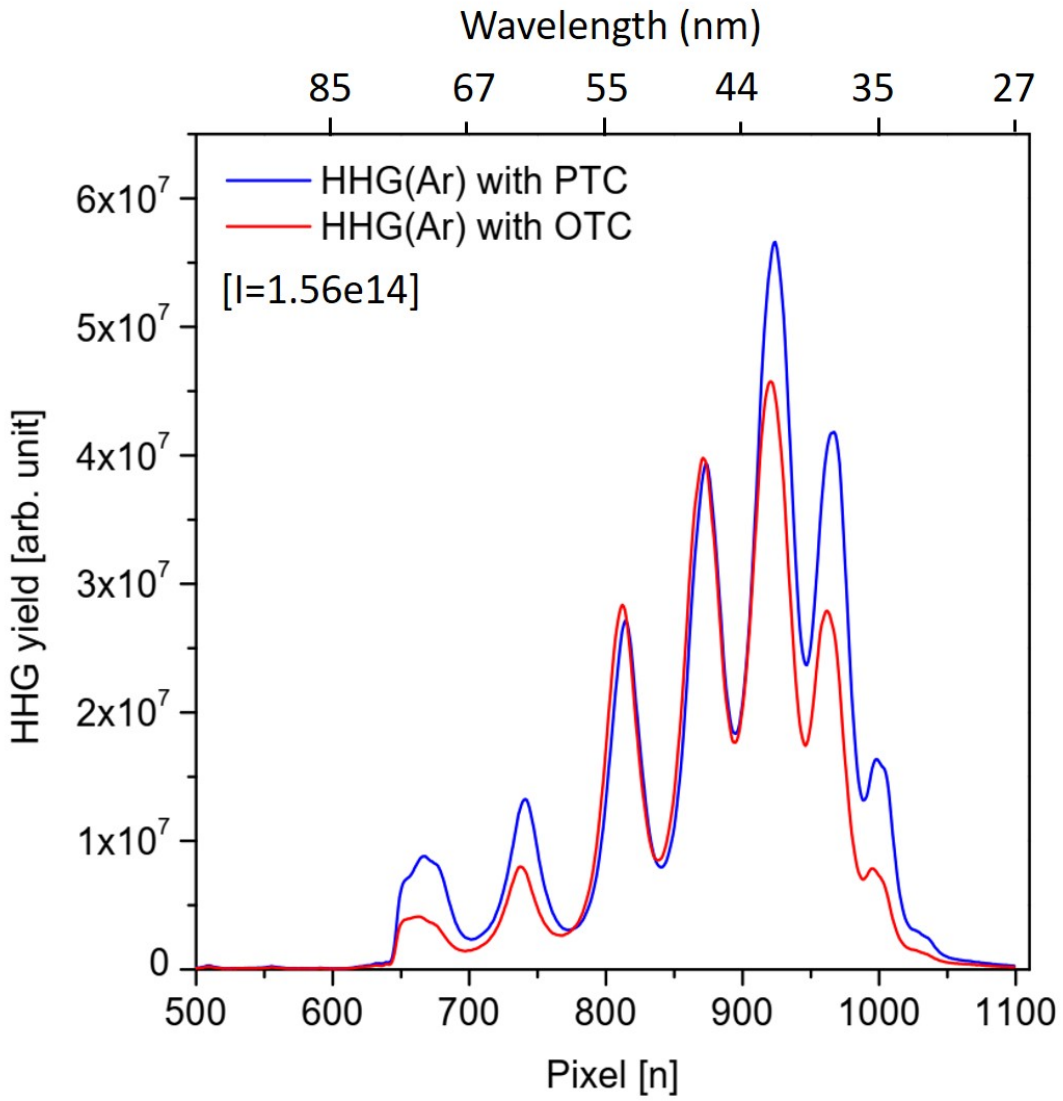

Figure 4.5: Two-color HHG spectra of Ar using OTC field vs PTC field.

4.3.4 Two-color HHG of atoms: Phase dependence

We investigated the influence of relative phase in two-color HHG by examining Argon spectra at two distinct relative phases (π and $\pi/2$) for both Orthogonal Two-Color (OTC) and Parallel Two-Color (PTC) configurations. This was done by rotating the calcite-mounted rotation stage. The laser intensity was set to 1.56 x 10^{14} W/cm^2,

and the pressure was maintained at 30 mbar. Interestingly, the HHG yield in both configurations displayed a dependence on the relative phase between the two colors. The yield was noticeably higher at $\pi/2$ phase delay. This observation matches the results from our simulation, which show that the harmonic yield is highest near the relative phase of $\pi/2$.

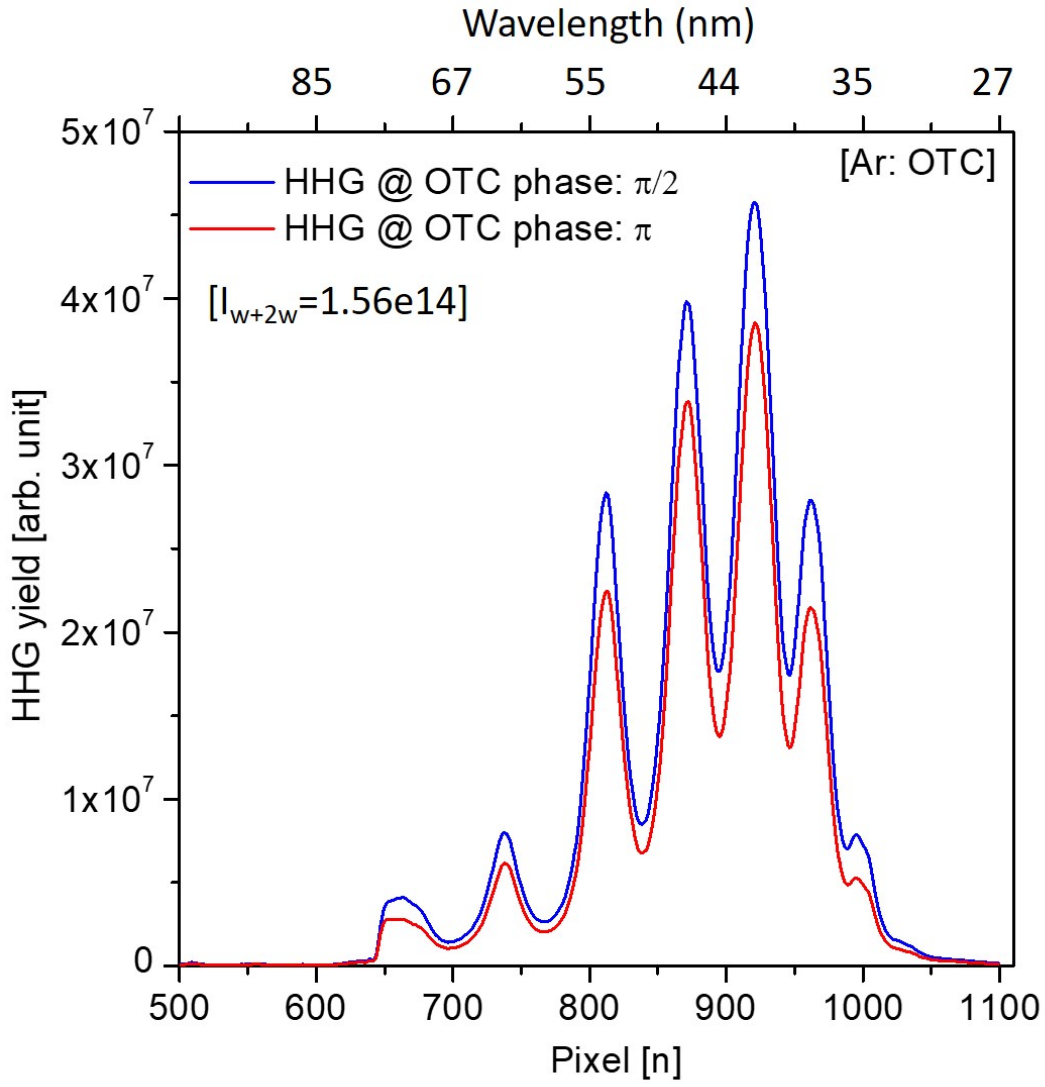

Figure 4.6: Two-color HHG spectra of Ar at phase π and $\pi/2$ using OTC fields.

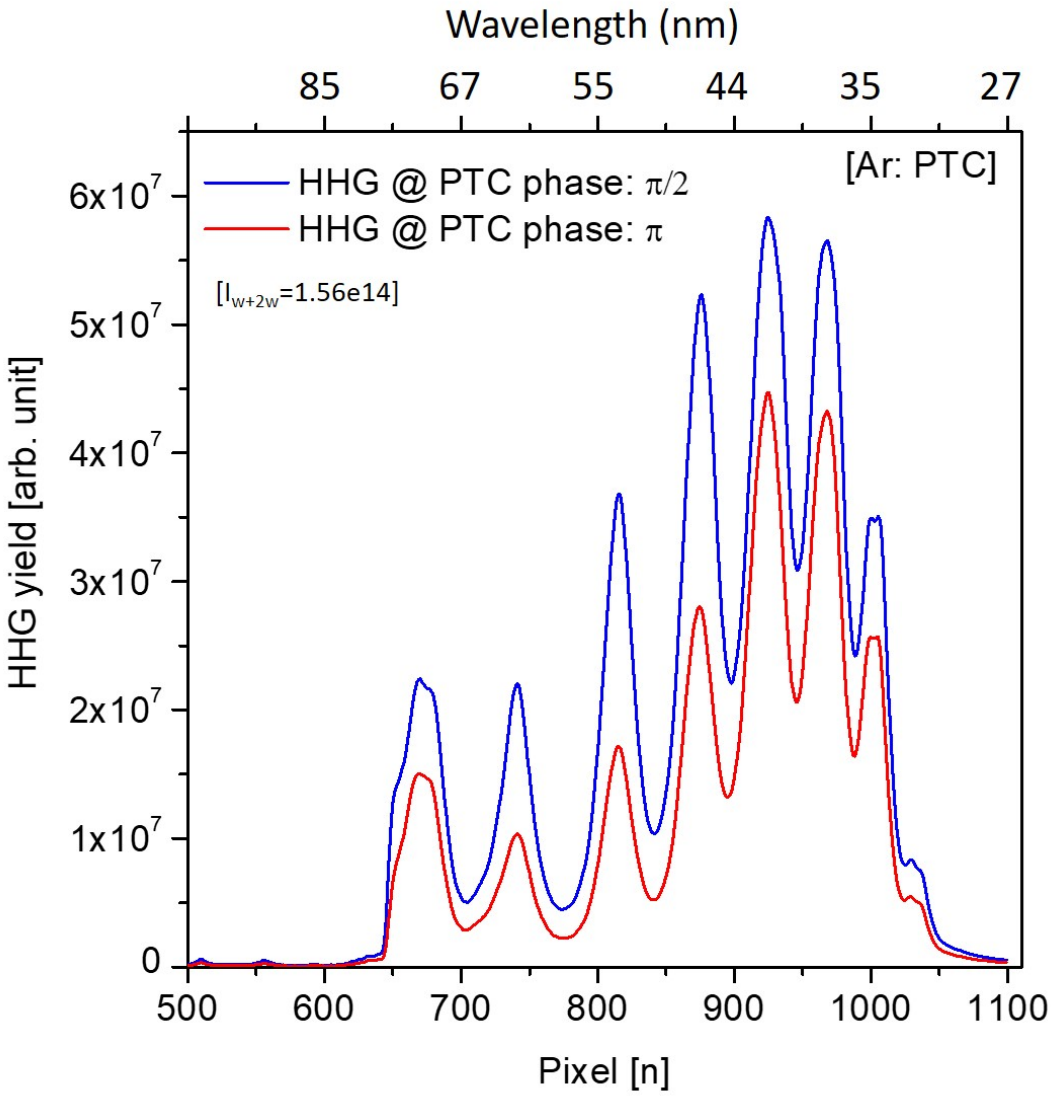

Figure 4.7: Two-color HHG spectra of Ar at phase π and $\pi/2$ using PTC fields.

4.3.5 Two-color HHG from atoms: Attosecond delay dependence

We shall now include the discussion of relative-phase dependent experiments in atoms (Ar and Kr). As discussed in the experimental section, we rotate the calcite plate and record the HHG spectra at multiple phase delay positions relative to a reference point defined as zero delay. Both OTC (Fig.4.8) and PTC (Fig.4.9) configurations are

explored in Argon to investigate the phase dependence on the HHG yield.

We see that the HHG yield exhibits a periodic modulation as the relative phase between the two colors is scanned. These results confirmed that the two-color relative phase modulates the tunnel electron trajectories, and thus, it affects the HHG yield. It is noteworthy that the yield variation is higher for higher harmonics. This is expected because higher harmonics on the onset of formation are more sensitive to intensity variations. In addition, we observe that the modulation depth in the PTC case is more than in the OTC case, in line with our previous results reported in [74].

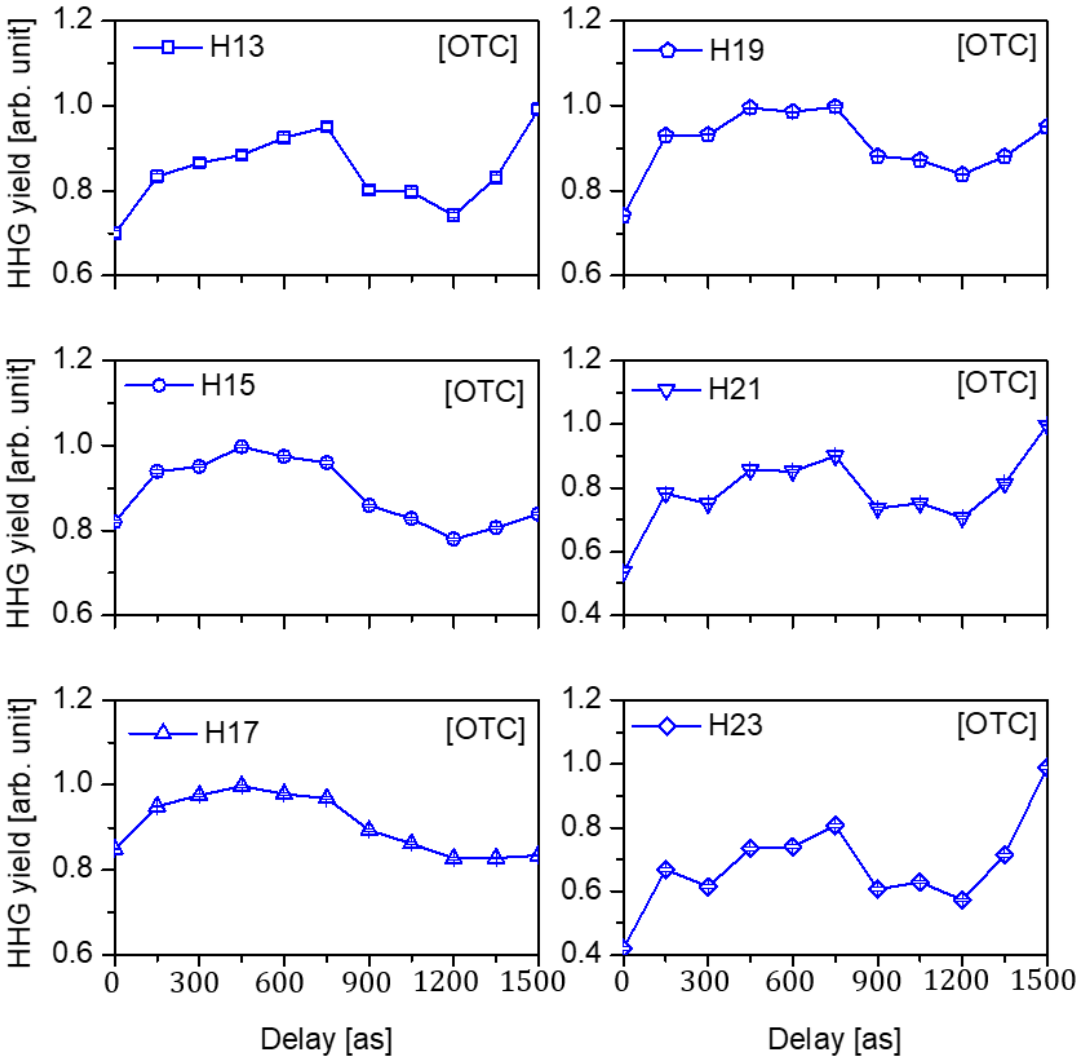

Figure 4.8: Orthogonal Two-color HHG in Ar as a function of relative phase delay.

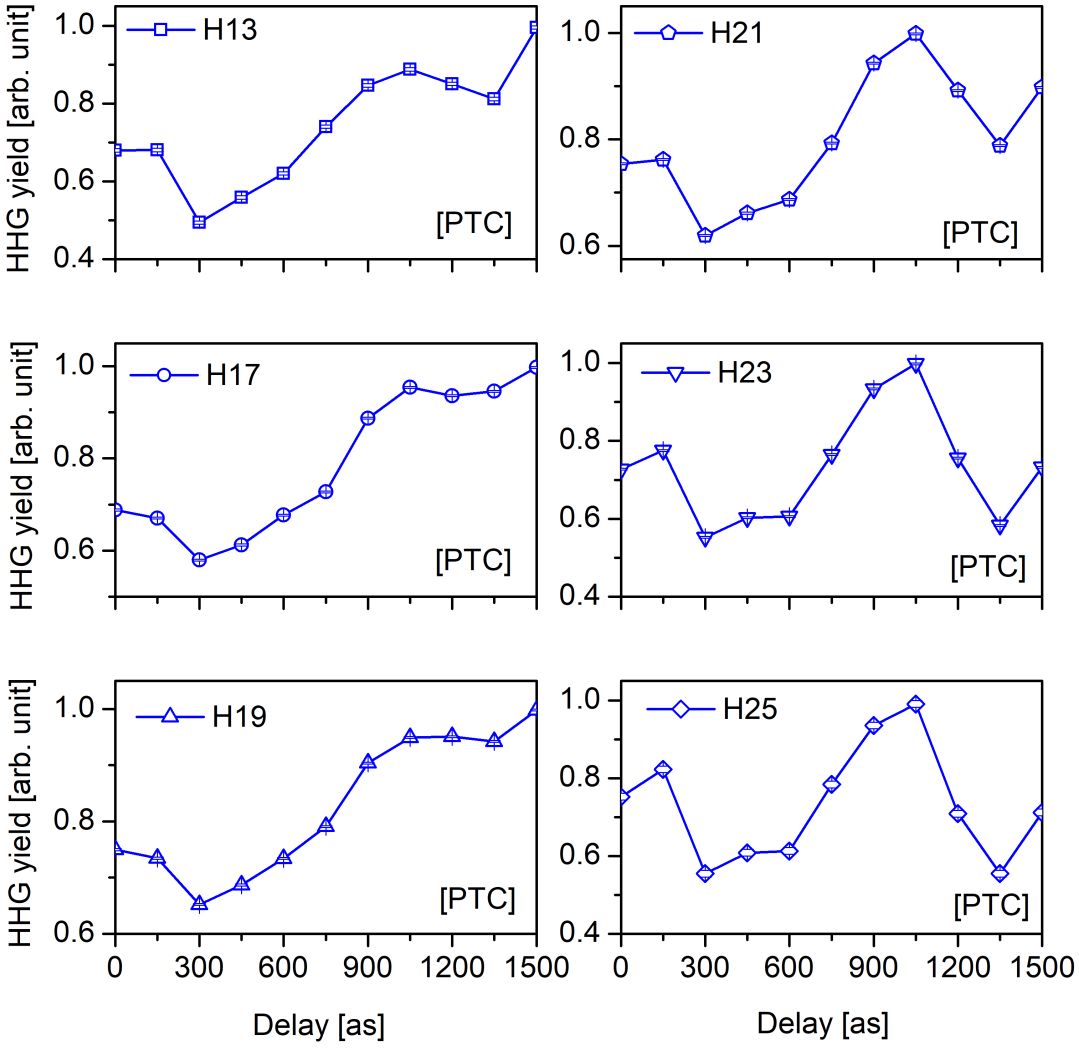

Figure 4.9: Parallel Two-color HHG in Ar as a function of relative phase delay.

Comparison with Simulation

We compare the results for the 15^{th} harmonic in the OTC configuration with the same result obtained using our simulation. For this, we estimated the electron trajectories as mentioned in the first section and calculated the position and kinetic energies of the returning electrons. Subsequently, the returning electrons falling within the range corresponding to the 15^{th} harmonic were sorted. The experimental and simulation re-

sults, as shown in Fig.4.10, align well, with the extent of modulation ranging from 0.8 to 1.0, further validating our experimental findings. It's noteworthy that one cycle of a 400nm pulse equates to 1330as. Consequently, owing to the overlap of the two pulses, one anticipates observing a complete phase variation across this temporal span. This phenomenon is evident in Fig.4.8 and Fig.4.9, where one complete cycle spans 1350as. Hence, in the case of Argon, our simulation successfully explains the variation in the HHG yield.

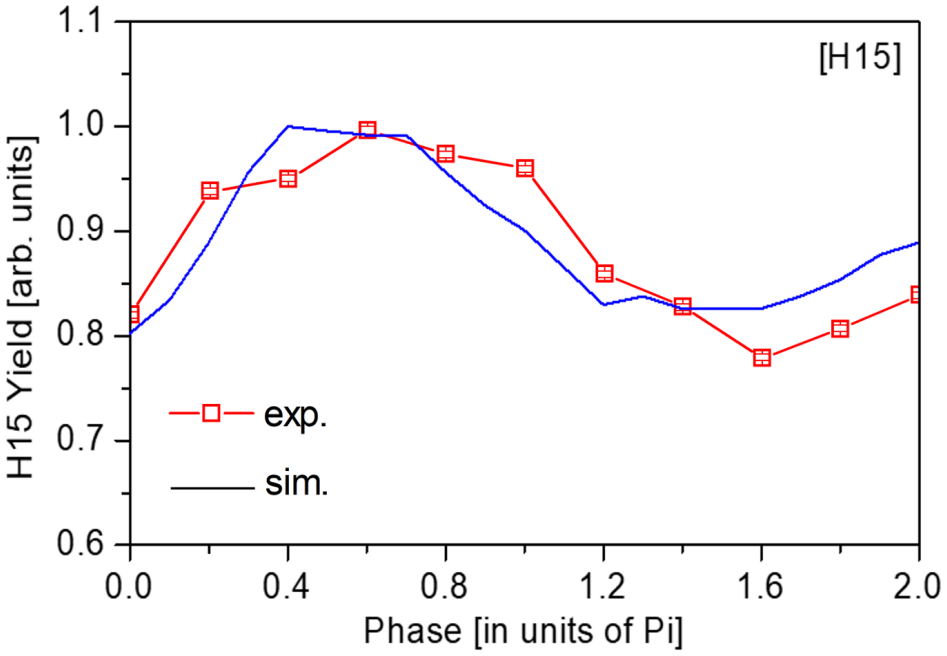

Figure 4.10: Experimental [Red] vs Simulated [Blue] Two-color HHG yield of Ar under the OTC configuration.

Delay dependence in Krypton

Delay dependence in Krypton at 0.69 W is shown in Fig.4.11 under the PTC configuration. Interestingly, similar to Ar, we observed the HHG yield variation as a function of relative phase. However, we noticed a double-peaked structure in higher harmonics. We will discuss this trend in more detail in the next chapter.

Overall, this study demonstrated that we can control the HHG yield using a two-color laser field.

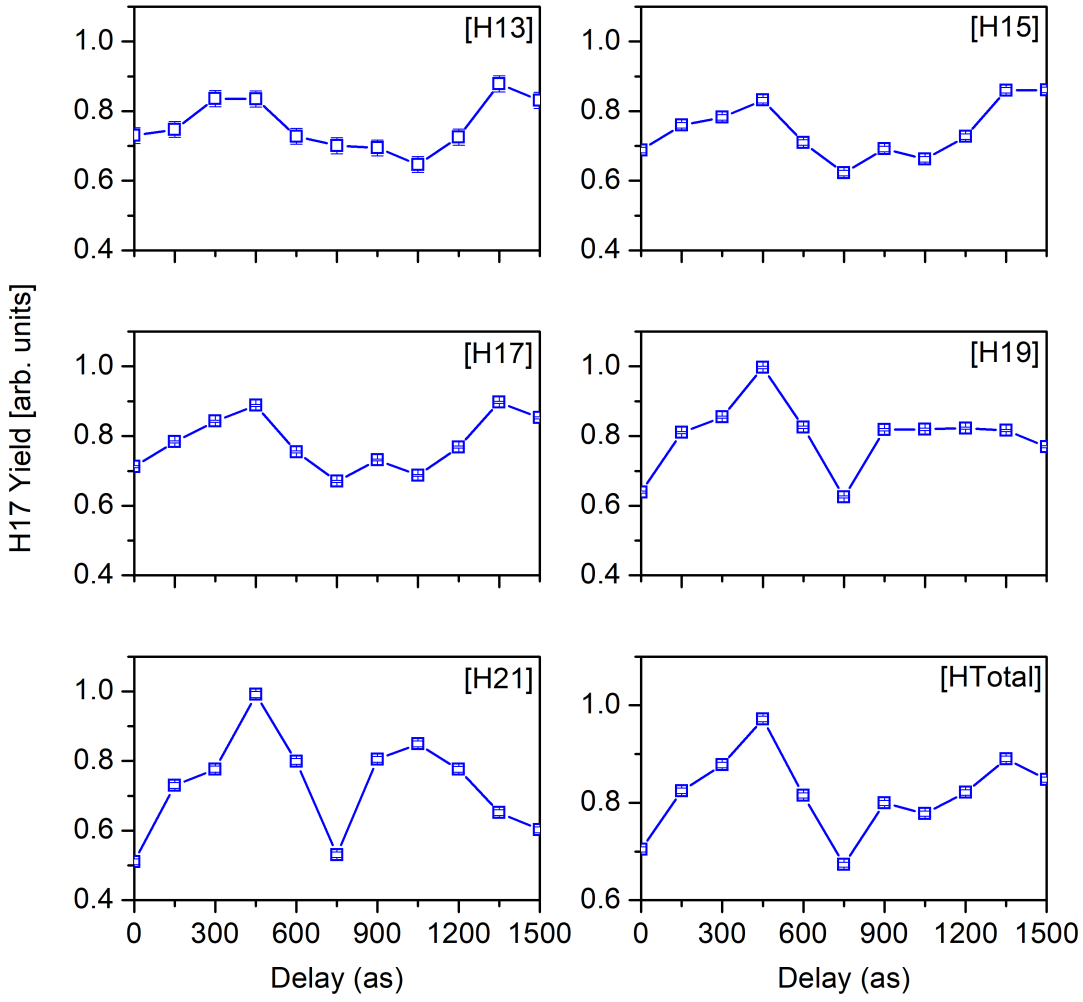

Figure 4.11: Two-color HHG of Kr as a function of relative phase in PTC case.

4.4 Summary and Conclusions

In this chapter we began by creating a theoretical framework for calculating the return kinetic energy and yield of the tunneled electrons across various birth times and delay positions of the two-color ultrashort pulses. This served as a future reference for our experimental investigations.

This was followed by a discussion of an experimental scheme for generating higher harmonics using two-color laser pulses. On the experimental front, we began by performing two-color intensity-dependent studies in Argon and Xenon. We showed that the effect of two-color intensity dependence on higher harmonics could be explained using the microscopic and macroscopic limits on the Intensity. A similar investigation in Xe showed that the use of Two-Color fields can reduce the cut-off intensities, especially for higher harmonic orders, making them easier to form than using just a single color.

In addition, we investigated the impact of relative phase and pulse configuration on high harmonic generation (HHG) in Argon (Ar) and Krypton (Kr) atoms using two-color laser fields. Comparing the Orthogonal Two Color (OTC) and Parallel Two Color (PTC) configurations in Argon, minimal change was observed in the 15th and 17th harmonics, while higher harmonics showed significant enhancement for the PTC case. This suggests that the relative polarization geometry of the two colors can influence the generation efficiency of higher-order harmonics.

In the Parallel Two Color (PTC) configuration, HHG spectra were obtained in Ar and Kr at different relative phases (π and $\pi/2$) of the two-color pulses to assess phase dependence. These measurements revealed variations in the yield of specific harmonic orders, indicating sensitivity to the relative timing between the two colors.

To delve deeper into the interplay between relative phase and electron dynamics, a two-color pump-probe attosecond delay experiment was conducted in Ar and Kr. This experiment focused on how the relative phase between the two-color fields affects the HHG spectra, revealing higher modulation in yield for higher harmonics, aligning with the previous results for intensity. The experimental modulations observed were explained using the classical trajectory simulations discussed earlier.

Chapter 5

Two-Color HHG in Molecules

Building upon our two-color studies in atoms, this chapter explores Higher Harmonic Generation (HHG) in N_2 and CH_3Cl molecules using two-color laser fields. While two-color HHG in atoms offers a fascinating interplay between laser parameters and harmonic yield, the scenario becomes even richer when considering molecules. We investigated the two-color phase dependence and observed an influence on the HHG yield in molecules, suggesting its impact extends beyond electron trajectories in atoms. To interpret these findings, we employed a theoretical simulation code that estimates the yield and kinetic energy of return electron trajectories under the experimental parameters. Detailed discussions of these studies, including the simulation results, are provided in the subsequent sections.

Unlike atoms with their spherically symmetric potentials, molecules possess intricate electronic structures governed by specific bond lengths and orientations. These factors significantly influence the HHG process in several ways:

Molecular Orbital Symmetry: The selection rules for HHG in molecules are gov-

erned by the symmetry of the molecular orbitals involved. Theoretical studies[75] have predicted different spectral characteristics for HHG arising from different orbitals within the molecule.

Nuclear Dynamics: In molecules, the nuclei are not stationary, and their vibrational and rotational motions can influence the electronic structure and, consequently, the HHG processes [76]. These nuclear motions can create transient changes in the molecular potential, potentially enhancing HHG at specific points in the vibrational cycle.

Alignment Dependence: Due to the non-spherical nature of molecules, the HHG yield often displays a strong dependence on the relative orientation between the polarization of the laser field and the molecular axis [77].

While many techniques, such as pulse shaping, and pump-probe techniques to achieve molecular alignment, can be employed for studying molecular dependencies in HHG, we restrict ourselves to the use of two-color fields.

5.0.1 Two-Color HHG from molecules: Phase dependence

We recorded HHG spectra for both molecules at specific phase delay positions corresponding to π and $\pi/2$ phases. As per our simulations, we expect the yield to be higher at the $\pi/2$ phase position.

Phase dependence in N_2

We compare the phase-dependent HHG spectra obtained with 0.73W total power at 32mbar pressure in N_2 at π and $\pi/2$ phases as shown in 5.1 similar to what we did for atoms; however, in this case, not much variation was observed except for harmonics

21 and 25 where the expected trend was still observed.

Phase dependence in CH_3Cl

We observed the HHG spectra using PTC fields at 0.47W and 1.1mbar pressure in CH_3Cl relative phase delays of π and $\pi/2$. We saw that the yield is greater at phase $\pi/2$, which is in line with our previous photoionization studies using two-color fields in the VMI spectrometer[74].

Looking at the results from both molecules, we went on to perform full delay-dependent studies to explore this phenomenon in greater detail.

5.0.2 Two-Color HHG from molecules: Attosecond delay dependence

The experimental scheme for this study remained the same as before.

Two-color attosecond delay dependence in N_2 As with the previous cases, we delayed the fundamental pulse with respect to the second harmonic field with delays ranging from 0 to 1350 as. We observed an interesting trend, as shown in Figure 5.3, in comparison to studies in Ar. The yield variation showed a double-peaked structure at delay positions of 300 as and 900 as, which correspond to π and $\pi/2$ phases, respectively. This explains why, in Fig. 5.1, we observed minimal change.

Two-color attosecond delay dependence in CH_3Cl

Having noted the double-peaked structure in N_2, albeit with a smaller variation in yield compared to atoms, we extended the range of relative phase between the two pulses up to 1950 as in order to understand the behavior in molecules. Fig.5.4 shows

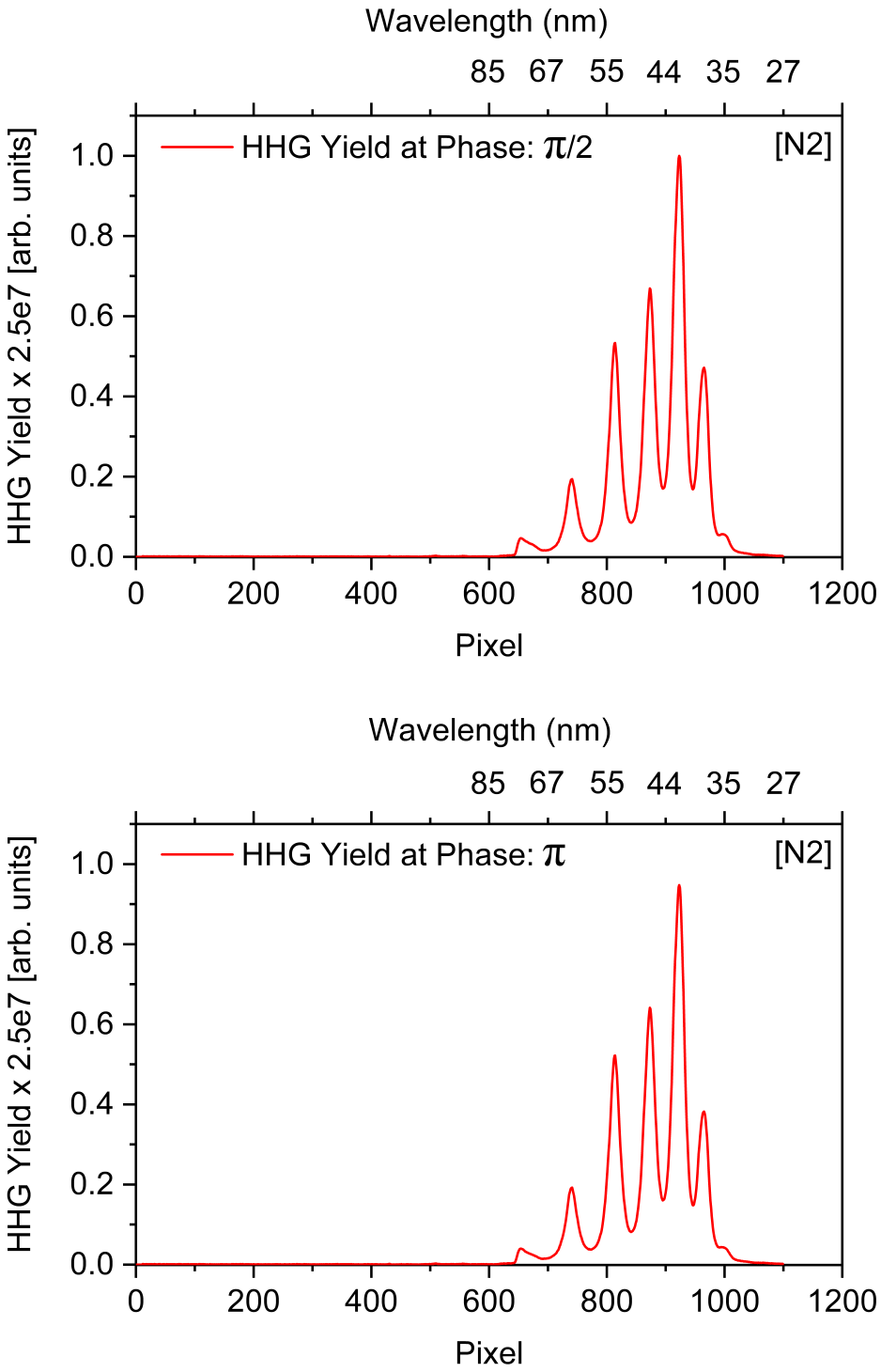

Figure 5.1: [top] Two-color (PTC) induced HHG spectrum of N_2 at $\pi/2$ phase, [Bottom] Two-color (PTC) induced HHG spectrum of N_2 at π phase.

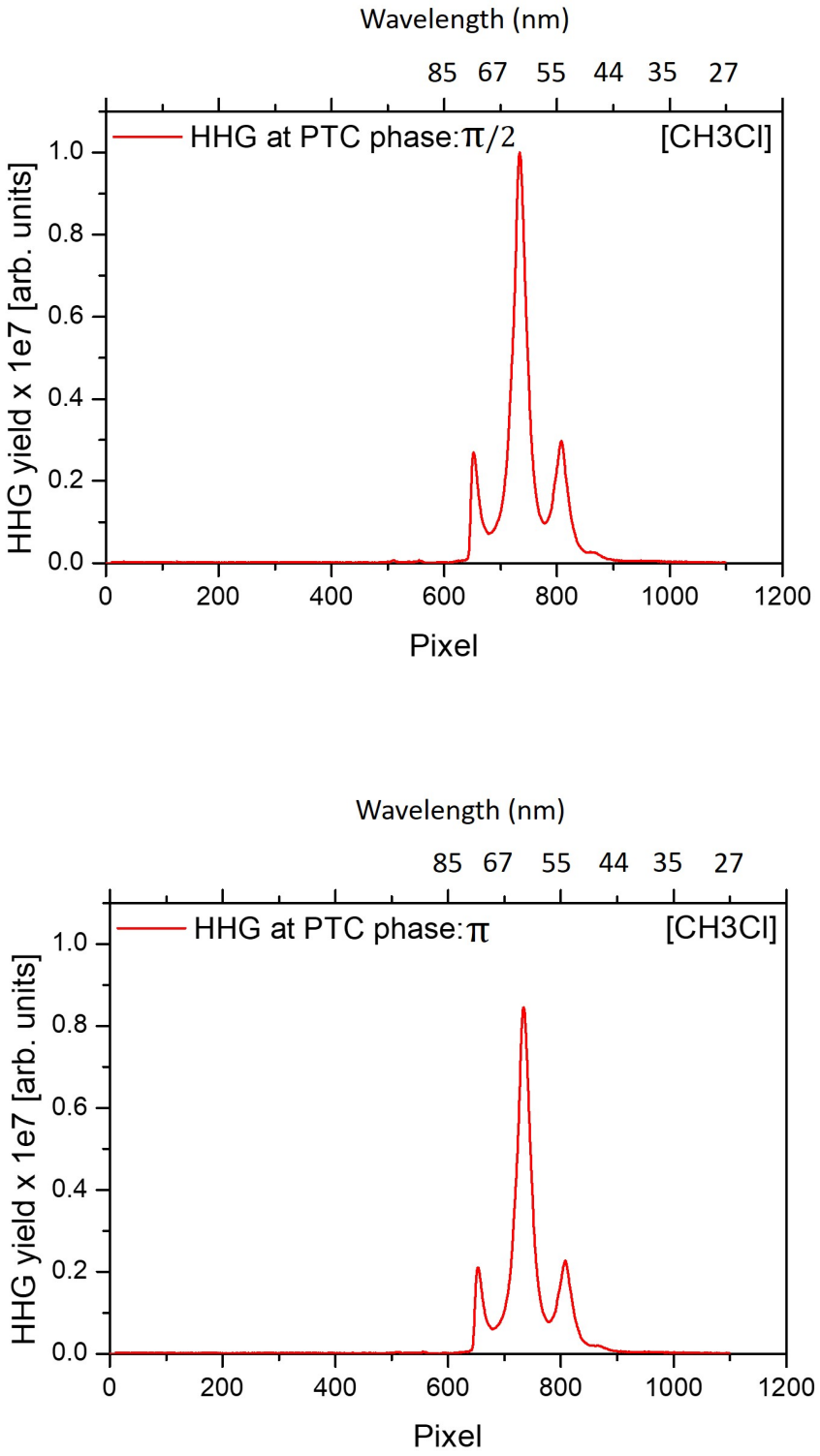

Figure 5.2: HHG spectrum of CH_3Cl at phase $\pi/2$[Top] and π[Bottom].

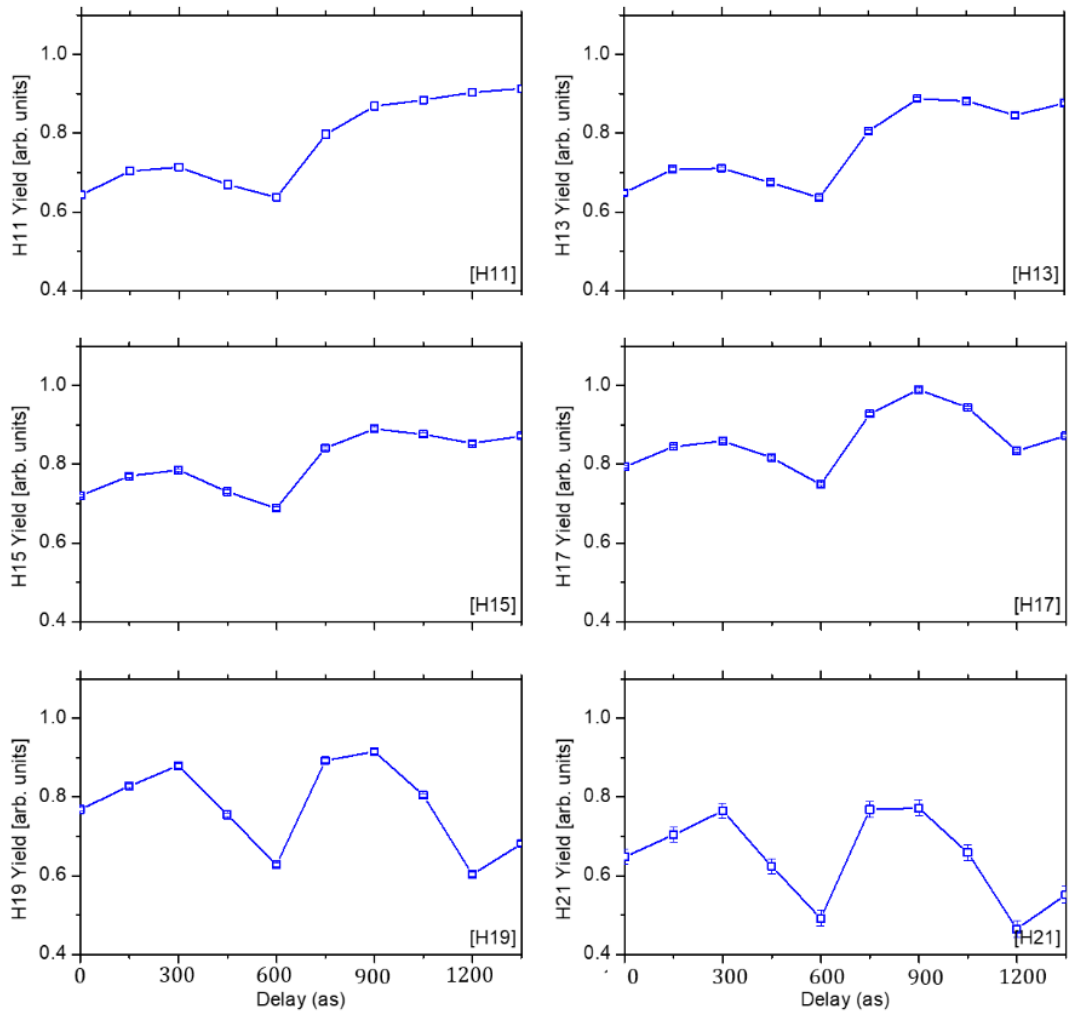

Figure 5.3: PTC delay dependence in N_2.

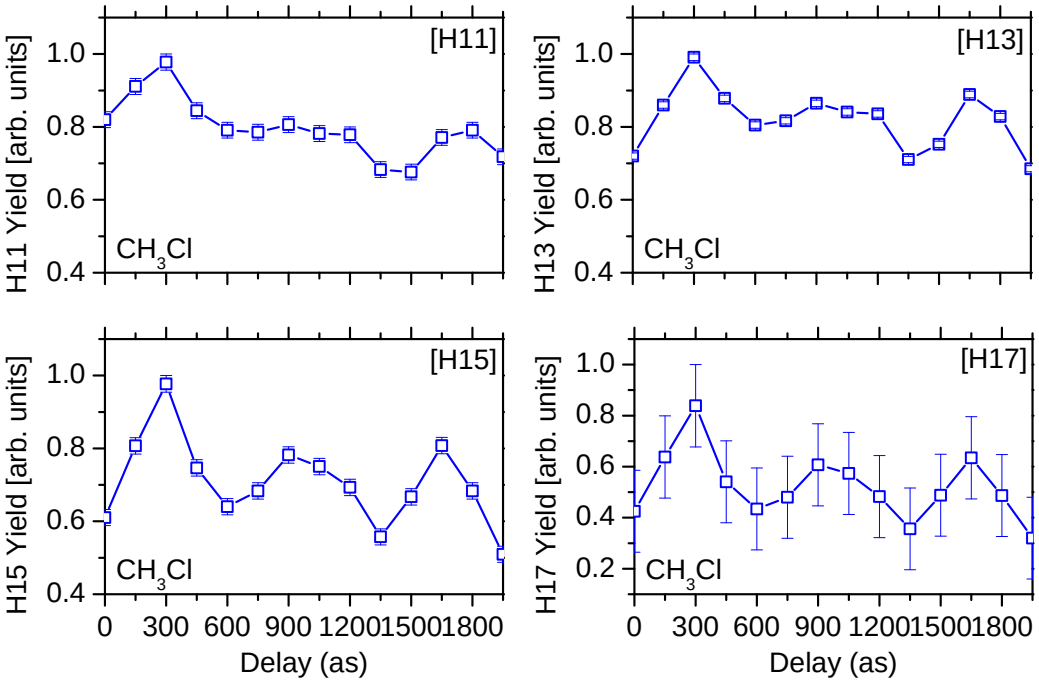

Figure 5.4: PTC delay dependence in CH_3Cl.

the two-color phase dependence for the PTC configuration. As with the previous cases, we observe a greater yield modulation at higher harmonics. Additionally, the double-peaked structure we observed in the previous cases is still present, and we see a similar peak at 1650 as, which corresponds to $3\pi/2$ phase. Therefore to summarize, we observe one full oscillation of the HHG yield in CH_3Cl with π phase duration however, now, instead of the yield falling at the π phase, it exhibits another peak. This trend continues at the subsequent $\pi/2$ phase delay.

Comparison with Simulations

In the preceding chapter, we successfully replicated the variation in yield observed in Argon through extensive 1D classical simulations for calculating y in 4.1. To explain the observed trend in N_2 and CH_3Cl both of which showed unique double-peaked

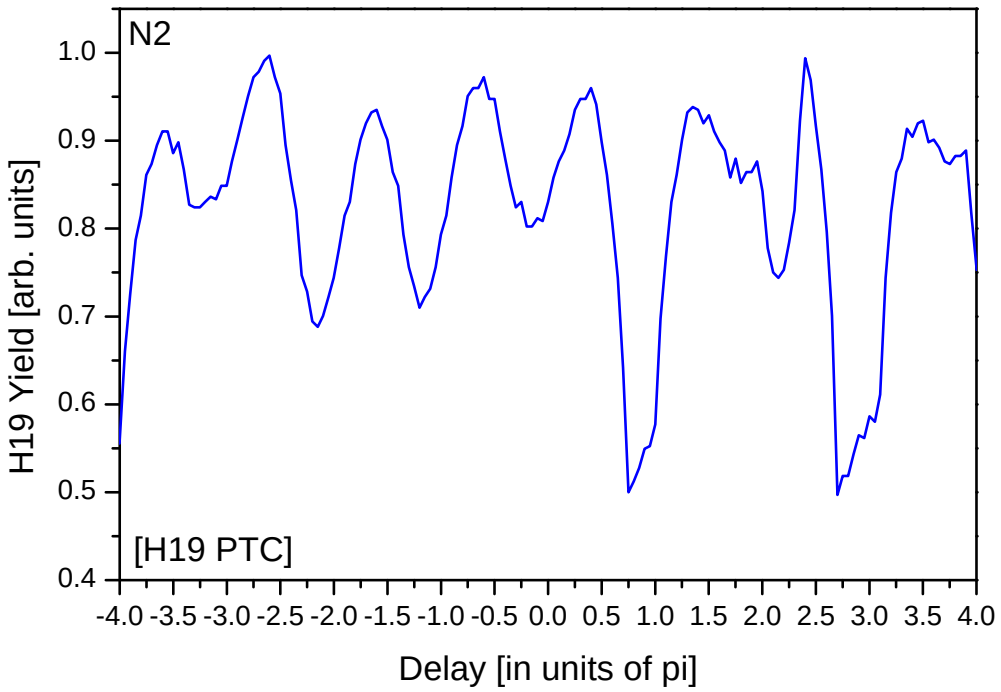

Figure 5.5: PTC delay dependence in N_2.

structures, we increased our phase delay range in our simulation to see if this trend could be observed at some specific delay positions of the two pulses. We began by performing the simulation for the 19^{th} harmonic of N_2 under the PTC configuration. The results are shown in 5.5. Contrary to our expectations, the theoretical projections failed to reveal the anticipated double-peaked pattern at any delay position. Although there were slight shifts in the positions of maxima, the separation between any two peaks consistently amounted to π; similar to the case in Argon. Subsequent investigations into other harmonic orders yielded similar variations.

We suspected that the phenomenon could be dependent on the Kinetic energy of the returning electrons and therefore choosing a lower ionization energy molecule such as CH_3Cl where the return K.E would be lower could show the doubled peak structures. The plots for the same for two harmonics H11 and H13 are shown in 5.6. The

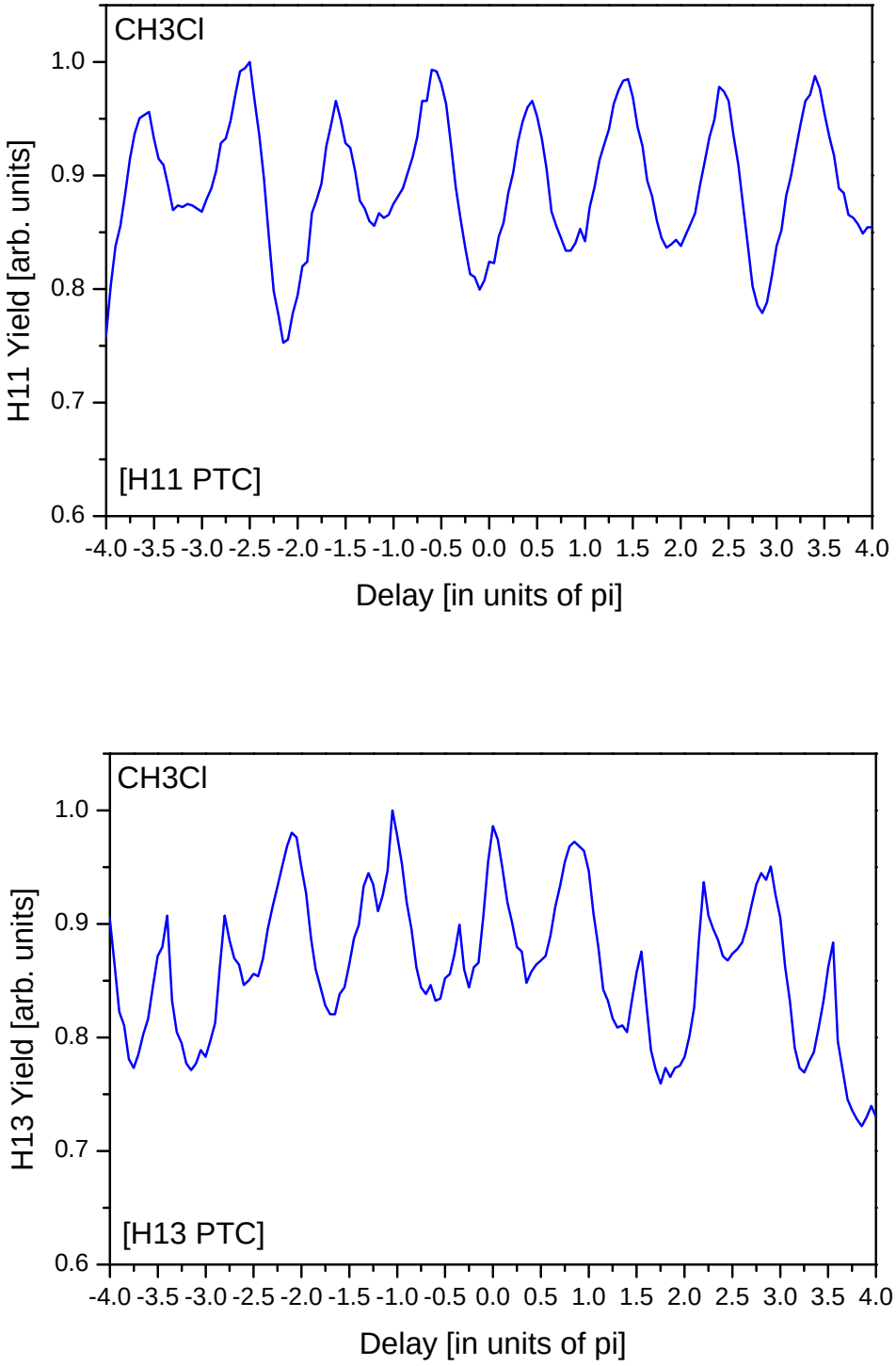

Figure 5.6: Simulated yield for PTC field induced HHG in CH_3Cl for [top] 11^{th} and [bottom] 13^{th} harmonic.

trend in H11 was comparable to the trend in N2. While H13 showed lower maxima's at some specific delay positions as observed in 5.6, the experimental observations suggested (almost) equal maxima's. Therefore, simple 1D - classical trajectory calculations based on the return kinetic energies of the tunneled electrons fail to explain the intricacies of the HHG yield variation observed in molecules. This limitation is not very surprising, as our semi-classical approach treats the molecule as a largely passive structure and does not account for orientation-dependent ionization or recombination dynamics. In this context, the models developed by Tong et al. [78] and At. Le et al.[67] would offer a more complete and structure-sensitive framework, when used alongside trajectory calculations.

The two papers together lay a theoretical foundation for quantitatively modeling high-order harmonic generation (HHG) in molecules by explicitly connecting the initial ionization process with the subsequent recollision dynamics. Tong et al. introduced the MO-ADK model, an extension of the atomic ADK theory, to account for the angular dependence of molecular orbitals during tunnel ionization. This model captures the impact of orbital symmetry and alignment angle on the ionization rate and successfully explains experimental observations such as ionization suppression in O_2 by introducing molecular structure through precomputed coefficients (Cl). It emphasizes that the spatial structure of the molecule plays a significant role in the first step of HHG and cannot be neglected in quantitative analyses.

Building on this, At. Le, CD Lin. and coworkers developed the Quantitative Rescattering Theory (QRS), which separates the HHG process into two components: the returning electron wave packet (governed by the laser field and ionization dynamics) and the photorecombination dipole (which encodes the molecular structure). QRS enables a clear distinction between what is laser-driven and what is target-specific, and

allows for more accurate modeling of HHG spectra from molecules by incorporating both dynamics and structure. These theoretical foundations have enabled significant advances in molecular orbital tomography[79, 80].

While implementing these models is beyond the scope of the present work, they form an essential theoretical backdrop that highlights the limitations of purely classical approaches. Incorporating them in future studies would likely help explain the more complex HHG behavior observed in molecular targets, especially under two-color driving conditions where (as we have experimentally realized) structure-dependent ionization timing plays a crucial role.

5.1 Summary and Conclusion

We expanded our investigation of two-color delay dependence to N2 and CH3Cl in order to understand the influence of the relative phase between the pulses and the dynamics of tunneled electrons on HHG from molecules. We observed minimal phase variation in N2 with some variation in CH3Cl at $\pi/2$ and π phase. While we observed higher modulation in yield for higher harmonics reminiscent of atoms, molecules exhibited a distinct double-peaked structure. Unlike atoms, where a peak at $\pi/2$ and a dip at π phase positions are observed, we observed peaks at both phase positions in molecules. Attempting to interpret our observations using classical 1D simulations, we realized their limitations in capturing molecular complexities, possibly due to geometric factors.

Chapter 6

Summary and Future Outlook

This thesis comprehensively investigated High Harmonic Generation (HHG) in atoms (Ar, Kr) and molecules (N_2 and CH_3Cl) utilizing both single-color and two-color laser fields. The primary objective was to explore the influence of revisiting tunneling electrons and their manipulation using two-color fields. A dedicated Two-Color High Harmonic Generation setup was developed for this purpose. By employing a two-color scheme, the study aimed to control the trajectories of revisiting electrons and analyze their impact on the resulting higher harmonics. The findings significantly contribute to our understanding of HHG induced by revisiting tunneling electrons and demonstrate the potential of utilizing this control mechanism to modulate HHG yield effectively. They also point to important areas where future research could yield valuable insights.

6.1 Summary and Outline

1. **Scientific Instruments developed for thesis work**

   For my thesis work, I developed the following instruments:

   (a) High Harmonic generation spectrometer

   I performed simulations in Zemax, designed and developed an HHG spectrometer based on a loose-focusing geometry, and optimized the setup using codes I developed in Python, based on a theoretical model by E.Constant.

   (b) Two-color pump-probe setup

   I extended the functionality of the HHG setup by developing a Two-Color pump-probe scheme in the collinear arrangement. The calibration for this scheme was done using the Third harmonic generation scheme and by observing the variation in photoelectron momentum distribution measured using the Velocity Map Imaging spectrometer.

2. **Scientific studies done for thesis work**

   Optimization of the High harmonic generation setup

   A Python code was developed based on the theoretical model proposed by E. Constant. This code was utilized to estimate the optimal phase-matching parameters required for the efficient generation of higher harmonics. The setup was then ready for further studies.

   [A] Study of macroscopic properties in Two-Color HHG

   A parametric optimization of Two-Color HHG was done, which showed a notable departure from the phase-matching parameters obtained using just the fundamental pulse. In Ar, while the phase-matching parameters related to Pressure

remained the same, huge deviations were seen in Z-dependence. Initially, there was anticipation that the theoretical model by E. Constant might fail to adequately explain the behavior observed using two-color fields. However, contrary to expectations, the model successfully accounted for both sets of observations. The deviations could be explained by studying the impact of a secondary field on the tunneled electron dynamics. The deviations in Z were linked to the contribution of long-trajectory electrons contributing to HHG, while the pressure-dependent phase-matching terms, devoid of tunneled electron effects, remained largely unaffected.

However, contrasting results were obtained for CO2, where deviations in pressure were also observed. These might be attributed to the geometric effects coming into play in the CO2 molecule.

[B] Two-Color HHG in Atoms

We explored the influence of relative phase and pulse configuration on high harmonic generation (HHG) in Argon (Ar) and Krypton (Kr) atoms using two-color laser fields.

Phase Dependence in PTC Configuration:

HHG spectra were obtained in Ar and Kr at different relative phases (π and $\pi/2$) of the two-color pulses in the Parallel Two Color (PTC) configuration to investigate phase dependence. These measurements revealed a noticeable variation in the yield of specific harmonic orders, indicating a sensitivity to the relative timing between the two colors.

Comparison of OTC and PTC Configurations in Argon:

HHG spectra were recorded in Argon for both OTC and PTC configurations. Interestingly, the 15th and 17th harmonics exhibited minimal change between

the configurations, while all higher harmonics showed a significant enhancement for the PTC case. This suggests that the relative polarization geometry of the two colors can influence the generation efficiency of higher-order harmonics.

Two-Color Pump-Probe attosecond delay Experiment:

To gain deeper insights into the interplay between relative phase and electron dynamics, a two-color pump-probe attosecond delay experiment was conducted in Ar and Kr. This experiment specifically focused on how the relative phase between the two color fields affects the HHG spectra. The modulation in yield was higher for higher harmonics. This was in line with the phase-matching conditions for intensity.

Simulations for Electron Dynamics:

To complement the experimental findings, theoretical simulations were performed to calculate the return kinetic energies of tunneling electrons for various birth times and across multiple delay positions of the two-color pulses. The simulations employed a high temporal resolution of 1 attosecond for birth times and a fine delay(/phase) step size of 0.05π amongst fundamental and second harmonic pulses. The theoretical data obtained from the simulations was then sorted based on the return kinetic energies of electrons responsible for generating specific harmonics of interest.

[C] Two-Color HHG in molecules

Phase Dependence in PTC Configuration:

HHG spectra were obtained in Nitrogen(N_2) and Chloromethane(CH_3Cl) at different relative phases (π and $\pi/2$) of the two-color pulses in the Parallel Two Color (PTC) configuration to investigate phase dependence. These measurements revealed a negligible variation in N_2 and some variation in CH_3Cl

Two-Color Pump-Probe attosecond delay Experiment:

We extended our two-color delay study to N_2 and CH_3Cl to understand the role of the relative phase between the pulses and the tunneled electron dynamics in HHG from molecules. Specifically, a double-peaked structure was observed in both the molecules. The obtained results compared with the simulation data compelled us to look beyond simple classical models and consider geometrical complexities.

6.2 Future Scope

In the near future, I would like to perform the following studies :

- **Two-Color HHG using other molecules**

  It will be interesting to compare HHG from N_2, a homo-nuclear molecule, with that of CO, a heteronuclear molecule possessing a permanent dipole moment. Similarly, it would be interesting to study the role of molecular geometry in HHG using CO_2(linear) and SO_2(bent) molecules.

- **XUV-IR experiments**

  An XUV-IR beamline has already been developed in our lab, a schematic of which is shown in Fig.6.1. The XUV beam will be produced using HHG while the IR beam will be combined using an off-axis parabolic hole mirror in the diagnostics chamber. This beamline will be combined with the VMI/ColTRIMS setup to perform XUV-IR pump-probe experiments in our lab.

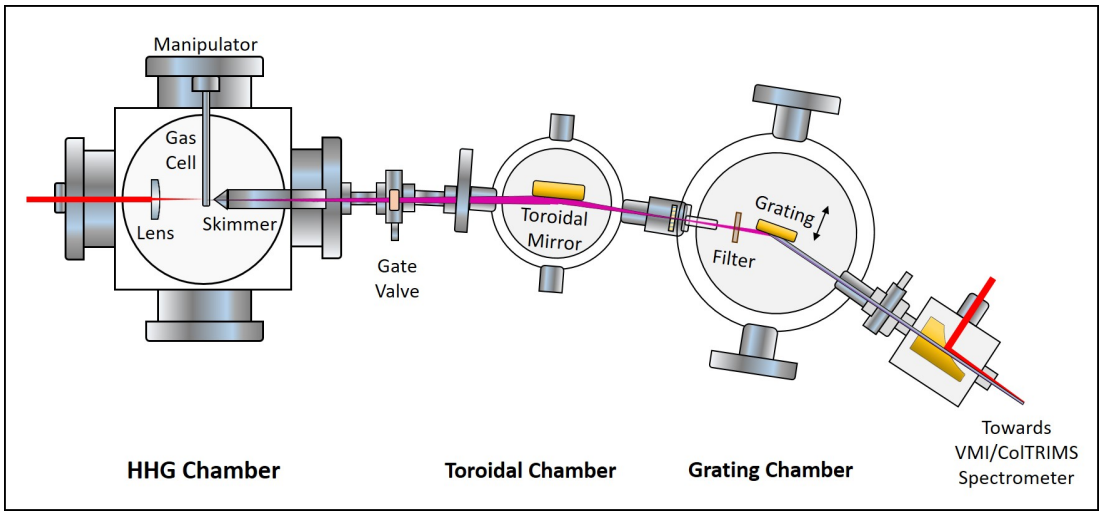

Figure 6.1: XUV-IR Beamline.

- **Orbital Angular Momentum transfer in HHG**

  By using a spiral phase plate to generate a Laguerre-Gaussian (LG) beam from the fundamental gaussian beam, I want to investigate the role of the tunneled electrons in facilitating the transfer of orbital angular momentum (OAM) from the incident beam to the resulting XUV beam. It will be interesting to study how the unique spatial phase structure of the LG beam interacts with the tunneled electrons during the harmonic generation process.

6.3 Addendum

6.3.1 Observance of even harmonics

HHG in krypton using two-color fields was generated to observe the appearance of even harmonics, using 0.8mJ pulse energy and a BBO crystal with approximately 30% second harmonic conversion efficiency.

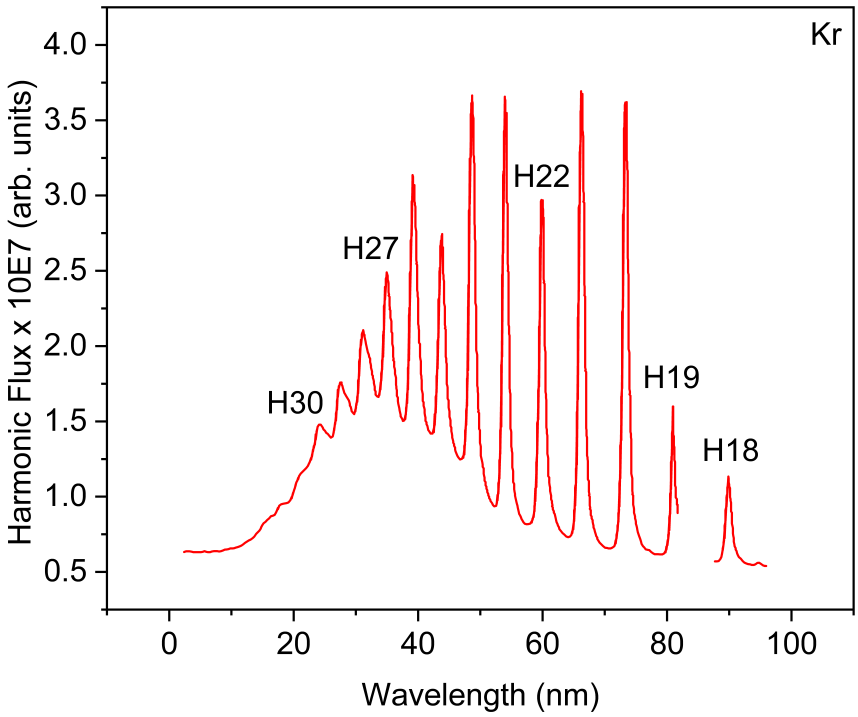

Figure 6.2: HHG using two-color fields in Kr. Both even and odd harmonics are observed.

6.3.2 Attosecond beamline in the making

The XUV-IR beamline described in Section 6.2 is shown below. High-order harmonic generation (HHG) in helium was performed using a 1030nm, 200fs laser pulse for the initial characterization of the setup. After harmonic selection via a grating, the XUV beam is focused onto the gas target in the VMI chamber using a toroidal mirror. For further details, readers are referred to the upcoming thesis work of Indrajit Kabiraj.

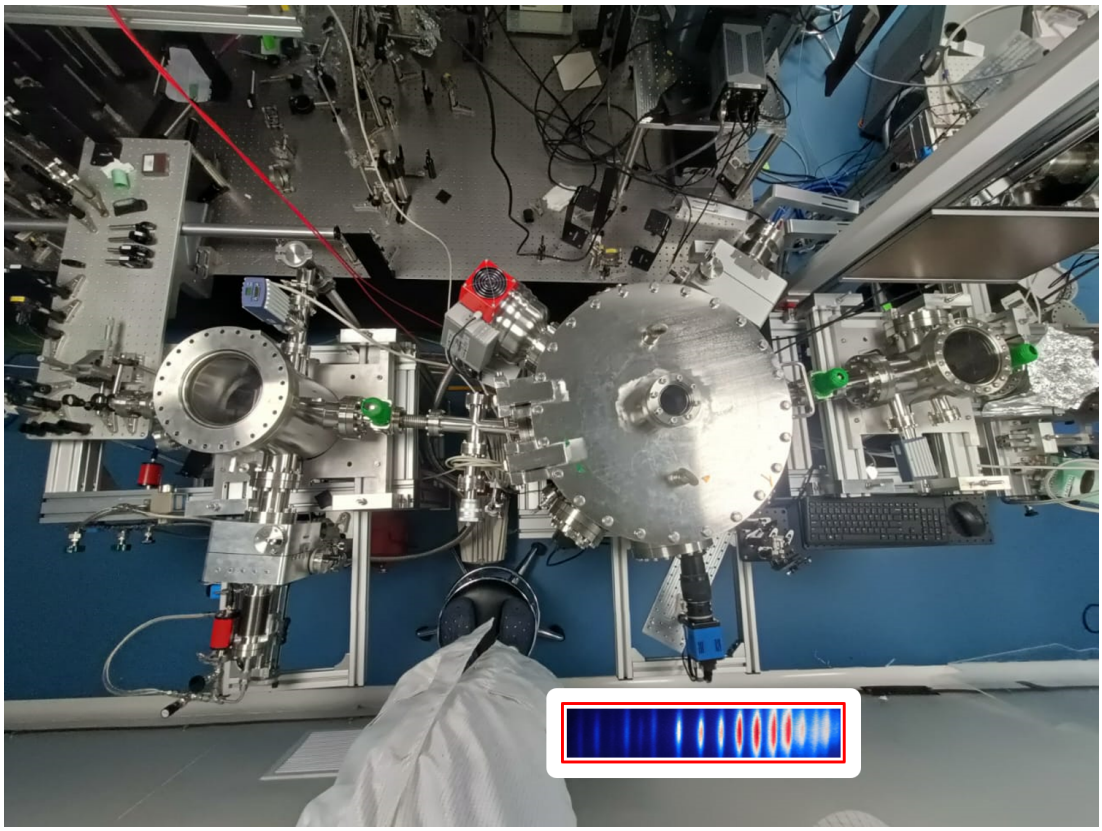

Figure 6.3: The XUV-IR beamline at PRL. HHG from Helium is shown at the bottom.

Bibliography

[1] P. B. Corkum, *Plasma perspective on strong field multiphoton ionization,* Phys. Rev. Lett. **71**, 1994–1997 (1993).

[2] E. Constant, D. Garzella, P. Breger, E. Mével, C. Dorrer, C. Le Blanc, F. Salin, and P. Agostini, *Optimizing high harmonic generation in absorbing gases: Model and experiment,* Physical Review Letters **82**, 1668 (1999).

[3] R. Gutzler, M. Garg, C. R. Ast, K. Kuhnke, and K. Kern, *Light–matter interaction at atomic scales,* Nature Reviews Physics **3**, 441–453 (2021).

[4] J. Weiner and F. Nunes, *1Historical Synopsis of Light–Matter Interaction,* in "Light-Matter Interaction: Physics and Engineering at the Nanoscale, Second Edition," (Oxford University Press, 2017).

[5] P. B. Corkum and F. Krausz, *Attosecond science,* Nature physics **3**, 381–387 (2007).

[6] F. Calegari, G. Sansone, S. Stagira, C. Vozzi, and M. Nisoli, *Advances in attosecond science,* Journal of Physics B: Atomic, Molecular and Optical Physics **49**, 062001 (2016).

[7] H. Kapteyn, O. Cohen, I. Christov, and M. Murnane, *Harnessing attosecond science in the quest for coherent x-rays,* Science **317**, 775–778 (2007).

[8] H. Kim, M. Garg, S. Mandal, L. Seiffert, T. Fennel, and E. Goulielmakis, *Attosecond field emission,* Nature **613**, 662–666 (2023).

[9] J. Biegert, F. Calegari, N. Dudovich, F. Quéré, and M. Vrakking, *Attosecond technology (ies) and science,* Journal of Physics B: Atomic, Molecular and Optical Physics **54**, 070201 (2021).

[10] S. R. Leone and D. M. Neumark, *Attosecond science in atomic, molecular, and condensed matter physics,* Faraday Discussions **194**, 15–39 (2016).

[11] S. R. Leone, *Profile of pierre agostini, anne l'huillier, and ferenc krausz: 2023 nobel laureates in physics,* Proceedings of the National Academy of Sciences **121**, e2321587121 (2024).

[12] L. Poisson and F. Lépine, *Ultrafast phenomena from attosecond to picosecond timescales: theory and experiments,* The European Physical Journal Special Topics **232**, 1995–2000 (2023).

[13] M. Kretschmar, E. Svirplys, M. Volkov, T. Witting, T. Nagy, M. J. Vrakking, and B. Schütte, *Compact realization of all-attosecond pump-probe spectroscopy,* Science Advances **10**, eadk9605 (2024).

[14] G. A. Stewart, P. Hoerner, D. A. Debrah, S. K. Lee, H. B. Schlegel, and W. Li, *Attosecond imaging of electronic wave packets,* Physical Review Letters **130**, 083202 (2023).

[15] A. Zong, B. R. Nebgen, S.-C. Lin, J. A. Spies, and M. Zuerch, *Emerging ultrafast techniques for studying quantum materials,* Nature Reviews Materials **8**, 224–240 (2023).

[16] M. Lewenstein, P. Balcou, M. Y. Ivanov, A. L'Huillier, and P. B. Corkum, *Theory of high-harmonic generation by low-frequency laser fields,* Phys. Rev. A **49**, 2117–2132 (1994).

[17] P. Madhusudhan, R. Das, P. Bhardwaj, M. S. KM, V. Nimma, S. Soumyashree, and R. K. Kushawaha, *Strong-field ionization of n2 and co molecules using two-color laser field,* Journal of Physics B: Atomic, Molecular and Optical Physics **55**, 234001 (2022).

[18] I. J. Kim, C. M. Kim, H. T. Kim, G. H. Lee, Y. S. Lee, J. Y. Park, D. J. Cho, and C. H. Nam, *Highly efficient high-harmonic generation in an orthogonally polarized two-color laser field,* Physical Review Letters **94**, 243901 (2005).

[19] G.-T. Zhang, J. Wu, C.-L. Xia, and X.-S. Liu, *Enhanced high-order harmonics and an isolated short attosecond pulse generated by using a two-color laser and an extreme-ultraviolet attosecond pulse,* Physical Review A **80**, 055404 (2009).

[20] D. Boll, L. Martini, A. Palacios, and O. Fojón, *Two-color polarization control of angularly resolved attosecond time delays,* Physical Review A **107**, 043113 (2023).

[21] A. Mandal, P. C. Deshmukh, and K. P. Singh, *Controlling high harmonic generation using inhomogeneous two-color driving laser pulse,* Laser Physics **31**, 075302 (2021).

[22] M. Frolov, N. Manakov, A. Minina, N. Vvedenskii, A. Silaev, M. Y. Ivanov, and A. F. Starace, *Control of harmonic generation by the time delay between two-color, bicircular few-cycle mid-ir laser pulses,* Physical review letters **120**, 263203 (2018).

[23] X. Song, S. Yang, R. Zuo, T. Meier, and W. Yang, *Enhanced high-order harmonic generation in semiconductors by excitation with multicolor pulses,* Physical Review A **101**, 033410 (2020).

[24] A. McPherson, G. Gibson, H. Jara, U. Johann, T. S. Luk, I. McIntyre, K. Boyer, and C. K. Rhodes, *Studies of multiphoton production of vacuum-ultraviolet radiation in the rare gases,* JOSA B **4**, 595–601 (1987).

[25] M. Ferray, A. L'Huillier, X. Li, L. Lompre, G. Mainfray, and C. Manus, *Multiple-harmonic conversion of 1064 nm radiation in rare gases,* Journal of Physics B: Atomic, Molecular and Optical Physics **21**, L31 (1988).

[26] X. Li, A. l'Huillier, M. Ferray, L. Lompré, and G. Mainfray, *Multiple-harmonic generation in rare gases at high laser intensity,* Physical Review A **39**, 5751 (1989).

[27] A. L'Huillier, K. Schafer, and K. Kulander, *Higher-order harmonic generation in xenon at 1064 nm: The role of phase matching,* Physical review letters **66**, 2200 (1991).

[28] C. Lyngå, A. L'Huillier, and C.-G. Wahlström, *High-order harmonic generation in molecular gases,* Journal of Physics B: Atomic, Molecular and Optical Physics **29**, 3293 (1996).

[29] A. Flettner, T. Pfeifer, D. Walter, C. Winterfeldt, C. Spielmann, and G. Gerber, *High-harmonic generation and plasma radiation from water microdroplets,* Applied Physics B **77**, 747–751 (2003).

[30] A. D. DiChiara, E. Sistrunk, T. A. Miller, P. Agostini, and L. F. DiMauro, *An investigation of harmonic generation in liquid media with a mid-infrared laser,* Optics express **17**, 20959–20965 (2009).

[31] T. T. Luu, Z. Yin, A. Jain, T. Gaumnitz, Y. Pertot, J. Ma, and H. J. Wörner, *Extreme–ultraviolet high–harmonic generation in liquids,* Nature communications **9**, 3723 (2018).

[32] T. T. Luu, M. Garg, S. Y. Kruchinin, A. Moulet, M. T. Hassan, and E. Goulielmakis, *Extreme ultraviolet high-harmonic spectroscopy of solids,* Nature **521**, 498–502 (2015).

[33] Y. S. You, Y. Yin, Y. Wu, A. Chew, X. Ren, F. Zhuang, S. Gholam-Mirzaei, M. Chini, Z. Chang, and S. Ghimire, *High-harmonic generation in amorphous solids,* Nature communications **8**, 724 (2017).

[34] S. Ghimire and D. A. Reis, *High-harmonic generation from solids,* Nature physics **15**, 10–16 (2019).

[35] J. Li, J. Lu, A. Chew, S. Han, J. Li, Y. Wu, H. Wang, S. Ghimire, and Z. Chang, *Attosecond science based on high harmonic generation from gases and solids,* Nature Communications **11**, 2748 (2020).

[36] E. Mével, E. Constant, D. Garzella, P. Breger, C. Dorrer, C. Le Blanc, F. Salin, and P. Agostini, *Optimizing high order harmonic generation in absorbing gases,* in "AIP Conference Proceedings," , vol. 525 (American Institute of Physics, 2000), vol. 525, pp. 373–384.

[37] M. Sayrac, A. Kolomenskii, S. Anumula, Y. Boran, N. Hart, N. Kaya, J. Strohaber, and H. Schuessler, *Pressure optimization of high harmonic generation in a differentially pumped ar or h2 gas jet,* Review of Scientific Instruments **86** (2015).

[38] M. Sayrac, A. Kolomenskii, and H. Schuessler, *Pressure dependence of high*

order harmonic generation in nitrogen molecular gas and atmospheric air, Optik **179**, 994–1000 (2019).

[39] B. Major, D. Rivas, B. Bergues, M. Weidman, A. Muschet, H. Schröder, C. P. Kőrös, E. Balogh, K. Kovács, V. Tosa *et al.*, *Investigation of high harmonic generation using a high-power, 5-fs laser in a loose-focusing geometry,* in "The European Conference on Lasers and Electro-Optics," (Optica Publishing Group, 2017), p. CG_P_11.

[40] K. Kovács, B. Major, E. Balogh, C. P. Kőrös, P. Rudawski, C. Heyl, P. Johnsson, C. Arnold, A. L'Huillier, V. Tosa *et al.*, *Multi-parameter optimization of a loose focusing high flux high-harmonic beamline,* Journal of Physics B: Atomic, Molecular and Optical Physics **52**, 055402 (2019).

[41] Q. Lin, S. Li, and W. Becker, *High-order harmonic generation in a tightly focused laser beam,* Optics letters **31**, 2163–2165 (2006).

[42] J. Rothhardt, M. Krebs, S. Hädrich, S. Demmler, J. Limpert, and A. Tünnermann, *Absorption-limited and phase-matched high harmonic generation in the tight focusing regime,* New Journal of Physics **16**, 033022 (2014).

[43] Y. Niu, F. Liu, Y. Liu, H. Liang, Y. Yang, R. Ma, and D. Ding, *Pressure-dependent phase matching for high harmonic generation of ar and n2 in the tight focusing regime,* Optics Communications **397**, 118–121 (2017).

[44] U. Keller, *Recent developments in compact ultrafast lasers,* nature **424**, 831–838 (2003).

[45] U. Keller and R. Paschotta, *Ultrafast lasers* (Springer, 2021).

[46] S. Backus, C. G. Durfee III, M. M. Murnane, and H. C. Kapteyn, *High power ultrafast lasers,* Review of scientific instruments **69**, 1207–1223 (1998).

[47] M. V. Shugaev, C. Wu, O. Armbruster, A. Naghilou, N. Brouwer, D. S. Ivanov, T. J.-Y. Derrien, N. M. Bulgakova, W. Kautek, B. Rethfeld *et al.*, *Fundamentals of ultrafast laser–material interaction,* Mrs Bulletin **41**, 960–968 (2016).

[48] H. A. Haus, *Mode-locking of lasers,* IEEE Journal of Selected Topics in Quantum Electronics **6**, 1173–1185 (2000).

[49] T. Brabec, C. Spielmann, P. Curley, and F. Krausz, *Kerr lens mode locking,* Optics letters **17**, 1292–1294 (1992).

[50] S. Kimura, S. Tani, and Y. Kobayashi, *Q-switching stability limits of kerr-lens mode locking,* Physical Review A **102**, 043505 (2020).

[51] R. Weissenbilder, S. Carlström, L. Rego, C. Guo, C. M. Heyl, P. Smorenburg, E. Constant, C. L. Arnold, and A. L'Huillier, *How to optimize high-order harmonic generation in gases,* Nature Reviews Physics **4**, 713–722 (2022).

[52] J. R. Sutherland, E. Christensen, N. Powers, S. Rhynard, J. Painter, and J. Peatross, *High harmonic generation in a semi-infinite gas cell,* Optics Express **12**, 4430–4436 (2004).

[53] A. Ansari, M. Kumar, H. Singhal, and J. Chakera, *The effect of gas-density gradient on high-harmonic generation from neon-filled cells using annular and gaussian laser beams,* Journal of Physics B: Atomic, Molecular and Optical Physics **55**, 165602 (2022).

[54] Y. S. Kim, B. Moon, C. Kim, B.-k. Ju, J. H. Lee, and Y. M. Jhon, *Optimizing high harmonic generation in hollow-core gas cell considering variation of gas density,* Optics & Laser Technology **149**, 107803 (2022).

[55] H. Ren, A. Nazarkin, J. Nold, and P. S. Russell, *Quasi-phase-matched high harmonic generation in hollow core photonic crystal fibers,* Opt. Express **16**, 17052–17059 (2008).

[56] A. Rundquist, C. G. Durfee, Z. Chang, C. Herne, S. Backus, M. M. Murnane, and H. C. Kapteyn, *Phase-matched generation of coherent soft x-rays,* Science **280**, 1412–1415 (1998).

[57] X. Zhang, A. Lytle, T. Popmintchev, A. Paul, N. Wagner, M. Murnane, H. Kapteyn, and I. P. Christov, *Phase matching, quasi-phase matching, and pulse compression in a single waveguide for enhanced high-harmonic generation,* Opt. Lett. **30**, 1971–1973 (2005).

[58] E. A. Gibson, A. Paul, N. Wagner, S. Backus, I. P. Christov, M. M. Murnane, H. C. Kapteyn *et al.*, *High-order harmonic generation up to 250 ev from highly ionized argon,* Physical Review Letters **92**, 033001 (2004).

[59] A. Rundquist, C. G. Durfee III, Z. Chang, C. Herne, S. Backus, M. M. Murnane, and H. C. Kapteyn, *Phase-matched generation of coherent soft x-rays,* Science **280**, 1412–1415 (1998).

[60] L. Wang, H. Li, and Y. Zhang, *Spatio-temporal dependence of high harmonic generation in noble gas,* Optics Express **27**, 33898–33906 (2019).

[61] G. Wang, C. Jin, A.-T. Le, and C. Lin, *Influence of gas pressure on high-order-harmonic generation of ar and ne,* Physical Review A **84**, 053404 (2011).

[62] Y. Wu, J. Zhang, H. Ye, and Z. Xu, *Intensity-dependent interference effect in high-order harmonic generation from aligned h 2+ molecules,* Physical Review A **83**, 023417 (2011).

[63] P. M. Abanador, F. Mauger, K. Lopata, M. B. Gaarde, and K. J. Schafer, *Wavelength and intensity dependence of recollision-enhanced multielectron effects in high-order harmonic generation,* Physical Review A **97**, 043414 (2018).

[64] M. Ammosov, *Mv ammosov, nb delone, and vp krainov,* Sov. Phys. JETP **64**, 1191 (1986).

[65] C. Jin, G. Wang, H. Wei, A.-T. Le, and C. D. Lin, *Waveforms for optimal sub-kev high-order harmonics with synthesized two- or three-colour laser fields,* Nature Communications **5**, 4003 (2014).

[66] T. Severt, J. Troß, G. Kolliopoulos, I. Ben-Itzhak, and C. A. Trallero-Herrero, *Enhancing high-order harmonic generation by controlling the diffusion of the electron wave packet,* Optica **8**, 1113–1121 (2021).

[67] A.-T. Le, R. R. Lucchese, S. Tonzani, T. Morishita, and C. D. Lin, *Quantitative rescattering theory for high-order harmonic generation from molecules,* Phys. Rev. A **80**, 013401 (2009).

[68] I. J. Kim, C. M. Kim, H. T. Kim, G. H. Lee, Y. S. Lee, J. Y. Park, D. J. Cho, and C. H. Nam, *Highly efficient high-harmonic generation in an orthogonally polarized two-color laser field,* Phys. Rev. Lett. **94**, 243901 (2005).

[69] I. Kim, H. Kim, C. Kim, J. Park, Y. Lee, K.-H. Hong, and C. H. Nam, *Efficient high-order harmonic generation in a two-color laser field,* Applied Physics B **78**, 859–861 (2004).

[70] D. Milošević and W. Becker, *High-order harmonic generation by bi-elliptical orthogonally polarized two-color fields,* Physical Review A **102**, 023107 (2020).

[71] H. K. Avetissian, G. F. Mkrtchian, and A. Knorr, *Efficient high-harmonic generation in graphene with two-color laser field at orthogonal polarization,* Physical Review B **105**, 195405 (2022).

[72] M. Sayrac, A. A. Kolomenskii, J. Dong, and H. A. Schuessler, *Generation of enhanced even harmonics of fundamental radiation in temporally separated two-color laser fields,* Journal of Electron Spectroscopy and Related Phenomena **233**, 22–27 (2019).

[73] Y. Fang and Y. Liu, *Optimal control over high-order-harmonic ellipticity in two-color cross-linearly-polarized laser fields,* Physical Review A **103**, 033116 (2021).

[74] M. .P, R. Das, P. Bhardwaj, M. S. K M, V. Nimma, S. Soumyashree, and R. Kushawaha, *Strong-field ionization of n_2 and co molecules using two-color laser field,* Journal of Physics B: Atomic, Molecular and Optical Physics **55** (2022).

[75] P. M. Kraus and H. J. Wörner, *Perspectives of attosecond spectroscopy for the understanding of fundamental electron correlations,* Angewandte Chemie International Edition **57**, 5228–5247 (2018).

[76] X. Yuan, P. Wei, C. Liu, X. Ge, Y. Zheng, Z. Zeng, and R. Li, *Effect of nuclear motion on spectral broadening of high-order harmonic generation,* Opt. Express **24**, 8194–8201 (2016).

[77] N. Hay, R. Velotta, M. Lein, R. de Nalda, E. Heesel, M. Castillejo, and J. P. Marangos, *High-order harmonic generation in laser-aligned molecules,* Phys. Rev. A **65**, 053805 (2002).

[78] X. M. Tong, Z. X. Zhao, and C. D. Lin, *Theory of molecular tunneling ionization,* Phys. Rev. A **66**, 033402 (2002).

[79] S. Haessler, J. Caillat, W. Boutu, C. Giovanetti-Teixeira, T. Ruchon, T. Auguste, Z. Divéki, P. Breger, A. Maquet, B. Carré, R. Taïeb, and P. Salières, *Attosecond imaging of molecular electronic wavepackets,* Nature Physics **6**, 200–206 (2010).

[80] C. Vozzi, M. Negro, F. Calegari, G. Sansone, M. Nisoli, S. de Silvestri, and S. Stagira, *Generalized molecular orbital tomography,* Nature Physics **7**, 822–826 (2011).

List of Publications

Thesis related Publications

1. **Pranav Bhardwaj**, Madhusudhan, P, Vinitha Nimma, Rituparna Das, Pooja Chandravanshi and Rajesh K. Kushawaha,"Two-Color High Harmonic Generation Apparatus: Pressure, Power, and Delay effect on the harmonics yield" [Under preparation]

2. Madhusudhan, P., Rituparna Das, **Pranav Bhardwaj**, Muhammed Shameem KM, Vinitha Nimma, Swetapuspa Soumyashree, and Rajesh K. Kushawaha, "Strong-field ionization of N2 and CO molecules using two-color laser field", 10.1088/1361-6455/ac9873" [J. Phys. B: At. Mol. Opt. Phys. 55 234001]

Publications not included in Thesis

3. Rituparna Das, Deepak K Pandey, Vinitha Nimma, Madhusudhan P, **Pranav Bhardwaj**, Pooja Chandravanshi, Muhammed Shameem KM, Dheeraj Singh, and Rajesh K Kushawaha, "Strongfield ionization of polyatomic molecules: Ultrafast H atom migration and bond formation in photodissociation of CH3OH", 10.1039/D0FD00129E Faraday Discuss., 2021,228, 432-450

4. Rituparna Das, Deepak K Pandey, Swetapuspa Soumyashree, Madhusudhan P, Vinitha Nimma, Muhammed Shameem KM,**Pranav Bhardwaj**, Dheeraj Singh, and Rajesh K Kushawaha, "Strong-field ionization of CH3Cl: proton migration and association", 10.1039/D2CP02494B, Phys. Chem. Chem. Phys., 2022,24, 18306-18320

5. Muhammed Shameem K M, Madhusudhan P, Rituparna Das,**Pranav Bhardwaj**, Nimma Vinitha, Swetapuspa Soumyashree and Rajesh Kumar Kushawaha "Molecular emission dynamics from a femtosecond filament induced plasma plume",2022 J. Opt. 24 044015

6. Anju Rani, Pooja Chandravanshi, Jayanth Ramakrishnan, Pravin Vaity, P. Madhusudhan, Tanya Sharma,**Pranav Bhardwaj**, Ayan Biswas, R.P. Singh, "Free space continuous variable Quantum Key Distribution with discrete phases", Physics Open, Volume, 2023,100162

Other Publications

1. Madhusudhan P, Rituparna Das,**Pranav Bhardwaj**, Pooja Chandravanshi, Swetapuspa Soumyashree, Vinitha Nimma, and Rajesh K Kushawaha, "Modern Experimental Techniques in Ultrafast Atomic and Molecular Physics", 10.1007/978-981-33-6084-610, 978-98133-6084-6

2. Muhammed Shameem K M, Swetapuspa Soumyashree, Madhusudhan P, Vinitha Nimma, Rituparna Das,**Pranav Bhardwaj**, Prashant Kumar, and Rajesh K Kushawaha, "Nanosecond and Femtosecond Laser-Induced Breakdown Spectroscopy (LIBS): Fundamentals and Applications", 978-1-119-75840-2

3. Muhammed Shameem K M, Swetapuspa Soumyashree, Madhusudhan P, Vinitha

Nimma, Rituparna Das,**Pranav Bhardwaj**, Prashant Kumar, and Rajesh K Kushawaha, ”Molecular species formation in laser produced plasma”, 978-1-119-75840-2